Experimental Investigation of Turbulent Flow through Trashracks

By

Jonathan Mawuli Tsikata

A Thesis submitted to the Faculty of Graduate Studies of

The University of Manitoba

in partial fulfilment of the requirements of the degree of

Master of Science

Department of Mechanical/Manufacturing Engineering

University of Manitoba

Winnipeg, Manitoba

August, 2008

Experimental Investigation of Turbulent Flow through Trashracks

BY

Jonathan Mawuli Tsikata

A Thesis/Practicum submitted to the Faculty of Graduate Studies of The University of Manitoba in partial fulfillment of the requirement of the degree

Of

MASTER OF SCIENCE

ABSTRACT

This thesis reports on an experimental study of turbulent open channel flow near small-scale and large-scale trashrack models that are comprised of an array of bars. The experiments were conducted for a wide range of bar depth, bar thickness, bar shape, bar spacing and bar inclination to approach flow. For the small-scale models, the measurements were conducted at a range of Reynolds number and Froude number based on approach velocity and water depth. A particle image velocimetry (PIV) technique was used to conduct velocity measurements around the small-scale models, from which iso-contours and profiles of the mean velocities and turbulent statistics were obtained to study the effects of bar depth, bar thickness, bar shape, bar spacing and bar inclination to approach flow on the flow field and head losses in the bars. The iso-contours of the mean velocity for small-scale models revealed that bar inclination produced asymmetric flow, a potential threat for vibration failure. The mean velocities and turbulent statistics within the bars were high, and increase with increasing blockage ratio and bar inclination.

For the large-scale models, the Reynolds and Froude numbers based on approach velocity and water depth were kept constant. Acoustic Doppler velocimeter and point gauge were used for the large-scale model measurements. The results demonstrate that head loss coefficient generally increased non-linearly with bar inclination and linearly with blockage ratio. Significant reduction in head losses was observed when the square leading edges of rectangular bars are replaced by rounded leading edges. For the bar depths considered in this study, it was found that the head loss coefficient is somewhat lower for the shorter bar depths.

ACKNOWLEDGEMENT

I first expressed my profound gratitude to the almighty God, for giving me life and seeing me through this program. I am also indebted to my advisor, Dr. Mark F. Tachie, for his support, advice, idea, and patience. My sincere thanks go to my advisory committee members; Chris Katopodis, Efrem Teklemariam, Haitham Ghamry, Kevin Sydor, Bernie Shumilak, and Dennis Lemke. Thanks should also go to Dr. Shawn Clark for his technical assistance. I gratefully acknowledge the financial support of Manitoba Hydro in the form of postgraduate grant and that of Natural Sciences and Engineering Research Council (NSERC CRD) of Canada (awarded to Dr. Mark F. Tachie).

I extend my profound thanks to Dr. L. E. Ansong for instilling in me good principles and introducing me to Dr. Mark F. Tachie. My brothers and sisters, you are never left out, without your prayers and words of encouragement, I would not have made it, thanks. To you my great friends and students of Dr. Tachie, I am very grateful for your helps.

DEDICATION

This manuscript is dedicated to my parents and my wife.

TABLE OF CONTENTS

LIST OF TABLES

LIST OF FIGURES

Page

Page

Page

Page

NOMENCLATURE

$2B$	inserted channel width
b	clear spacing between the adjacent bars
b_a	centre-to-centre spacing
B	coefficient for the horizontal angle of inflow, $B = 0.65$
C	coefficient applicable to the blockage ratio, p, $C = 1.33$
D	coefficient applicable to the ratio of b/L. $D = - 0.43$
F	Froude number ($F = U_e/[gh_1]^{0.5}$)
g	acceleration due to gravity
H	bar height
h_1	upstream potential head,
h_2	downstream potential head
k	coefficient of bar shape, according to Fellenius & Lindquist [9]
k_F	coefficient of bar shape, according to Meusburger *et al.* [7]
L	bar depth
n	number of bars
N	total instantaneous image pairs
p	blockage ratio
R	ratio of the net flow area to the gross trashrack area ($R = A_{net}/A_{gross}$)
RD	round leading edge bar
Re_s	Reynolds number ($Re_s = U_e s/\nu$)
s	bar thickness
SQ	square leading edge bar
ST	streamlined shape bar

u, w streamwise and spanwise turbulence intensities

U, W streamwise and spanwise mean velocity components

U average velocity through the net flow area of trashrack

U_1 average velocity at the upstream of the trashrack

U_2 average velocity at the downstream of the trashrack

U_e approach velocity

Greek symbols

α the vertical angle in between the main direction of the local current and the trashrack (in the present study $\alpha = 90°$)

β coefficient of bar shape, according to Spangler [6]

δ the horizontal angle of inflow

ε flow ratio

Δh head loss

Δh^* head loss coefficient

μ the coefficient of contraction

ϕ coefficient of bar shape, according to Kirschmer [8]

θ bar inclination to approach flow

ν fluid kinematic viscosity

CHAPTER 1: INTRODUCTION

1.1. Introduction

Trashracks are comprised of an array of vertical rectangular bars that are held together by supporting beams. They are typically fitted to the inlet of hydraulic generating units to prevent large debris or obstacles from entering the units and damaging turbine components and/or reducing hydraulic performance. Figure 1.1 shows a photo of a trashrack section consisting of an array of bars held together by supporting beams at one of the power generating units of Manitoba Hydro. Figure 1.2 shows a sectional view of a turbine with trashrack fitted at the inlet. Trashracks at intakes may also prevent mortality of relatively large fish by turbine blades. The fish protection efficiency of trashracks is mainly determined by spacing between trashrack bars and flow conditions at the intake and near bypass entrances.

The existence of trashracks at intakes produces unwanted energy losses that directly reduce power production. These losses can be partly attributed to the large scale flow structures or vortices generated by the bars. The vortices give rise to significant pressure fluctuations which in turn produces unsteady hydrodynamic forces acting on the bars. Research has shown that the formation of vortices by array of bars, their evolution and interaction depend strongly on bar spacing, and may also depend on the shape of the bars. Consequently, the choice of bar shape and spacing has a significant impact on energy losses and performance of hydro generating units. For example, streamlined shape would reduce head loss but it has been suggested that streamlined bars would increase the potential for vibrations and subsequent trashrack failure (McPhail [1]). Reduced bar

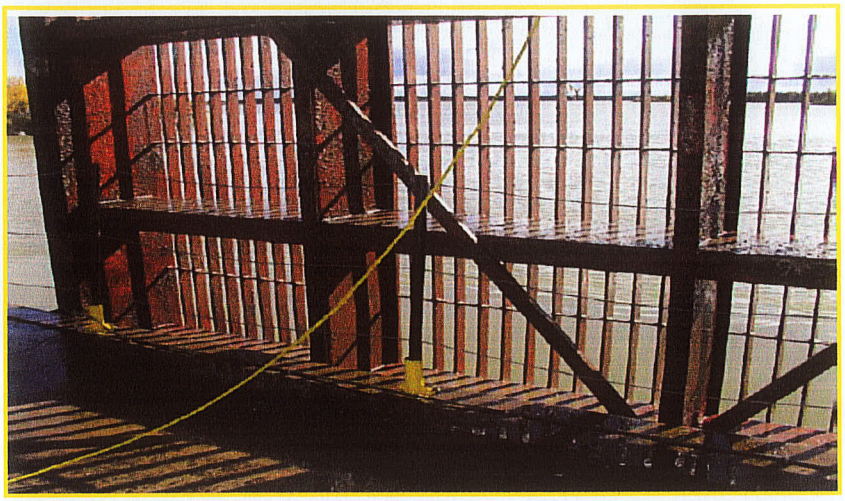

Figure 1.1: A photo of a trashrack section from Kelsey G.S. (*Courtesy of Manitoba Hydro*)

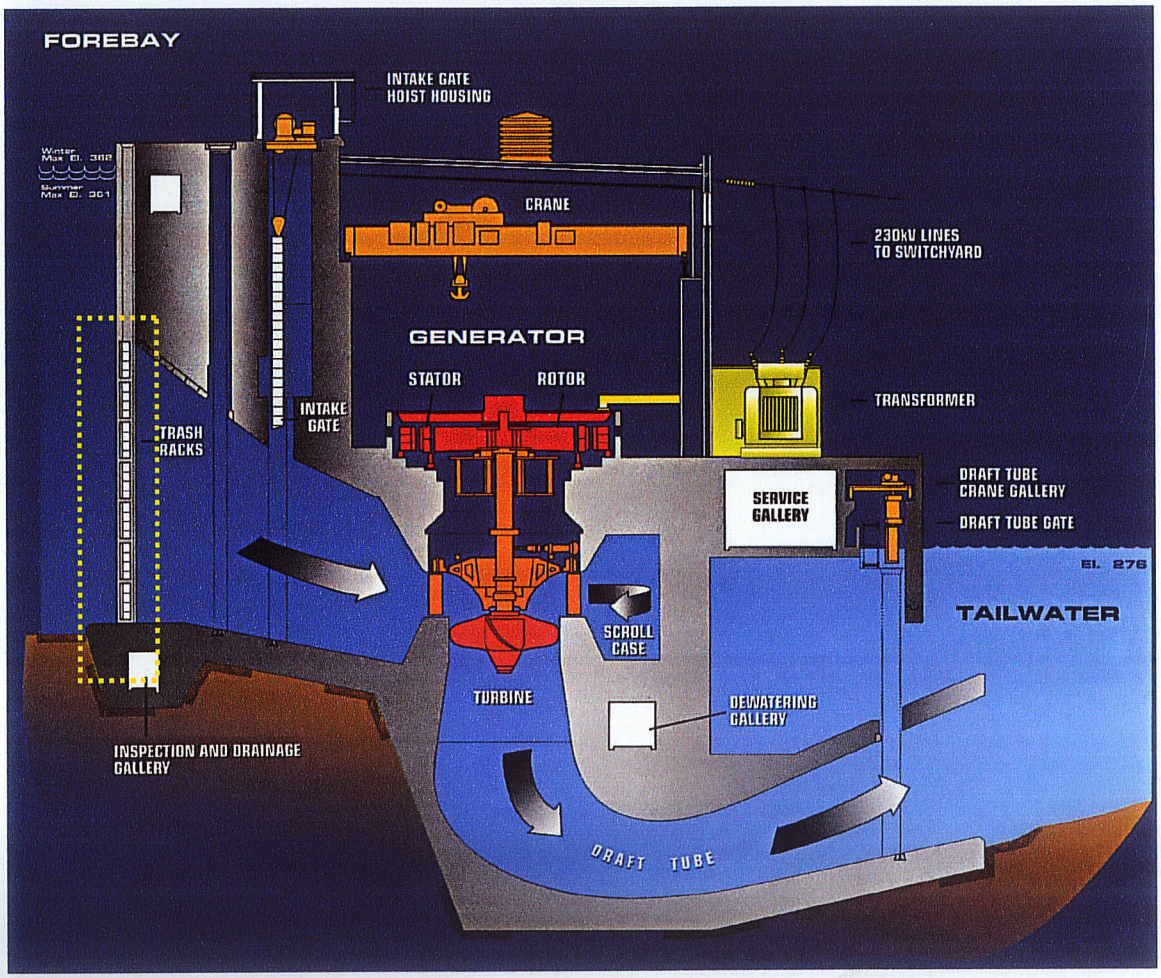

Figure 1.2: Sectional view of turbine plants showing relative position of trashrack with respect to turbine (*Courtesy of Manitoba Hydro*)

spacing would produce higher sectional blockage and consequently undesirable increase in head losses. On the other hand, reduced bar spacing would physically prevent smaller fish from entering the turbines and draft tubes, a desirable outcome. There is a need to better understand the flow characteristics near trashracks and also to provide benchmark data for validating turbulence models for hydraulic applications.

1.2. Research Motivation

Trashracks are important parts of hydro-power plants. Numerous experiments have been conducted in the past to study head losses produced by trashracks. In those experiments, only global flow quantities such as bulk velocity, water depth and pressure were measured. Furthermore, trashrack parameters such as bar shape have not been investigated in detail to assess their effects on head losses. There is a need to conduct detailed measurements and to study the characteristics of the mean flow pattern and turbulent statistics near trashracks of diverse bar shape, bar spacing, bar thickness and bar orientation.

To this end, Manitoba Hydro, Department of Fisheries and Oceans Canada (DFO) and the University of Manitoba have developed a collaborative research program to study the nature of turbulent flow through trashracks. The overall objective of the collaboration is to study the hydraulics near trashracks to assess the potential biological benefits and power generation cost. In this collaboration, the University of Manitoba is conducting physical modeling of small-scale and large-scale trashracks of diverse bar shape, bar thickness, bar depth, bar spacing and bar orientation. In order to understand the dynamics

of flow near the trashracks, it is necessary to obtain whole-field velocity measurements of the flow velocity around the trashracks using a particle image velocimetry (PIV). The Department of Fisheries and Oceans Canada is applying commercial Computational Fluid Dynamics software (CFX-11) and turbulence models of varying sophistication to conduct more extensive numerical analyses than in the physical modeling. The physical insight and benchmark datasets from the physical modeling would guide researchers at DFO to select the appropriate turbulence models and to validate the numerical results.

1.3 Objectives

This thesis reports on small-scale and large-scale physical modeling of trashracks of diverse bar shape, bar thickness, bar depth, bar spacing and bar orientation.

The specific objective of the small-scale experiments is to study the effects of approach flow velocity, bar spacing, bar shape, bar depth and bar inclination to approach flow on head losses as well as the mean flow patterns, mean velocity profiles and turbulent statistics. A particle image velocimetry technique is used to obtain detailed whole-field measurements of mean velocities and turbulence quantities near small-scale model trashracks.

The objective of large-scale physical modeling is to study the effects of bar leading edge, bar thickness, bar spacing, bar depth and bar inclination to approach flow on head losses. In these experiments, an acoustic Doppler velocimeter (ADV) is used to conduct the velocity measurement.

1.4. Layout of Thesis

The general layout of this thesis is as follow. Chapter 2 presents literature review on previous studies of flow through trashracks. Detailed descriptions of principles of operation of particle image velocimetry and acoustic Doppler velocimeter are presented in Chapter 3. Chapter 4 describes the experimental techniques that were employed for both small-scale and large-scale trashrack models. The experimental results are presented and discussed in Chapter 5. Chapter 6 presents the concluding remarks and recommendations for future work.

CHAPTER 2: LITERATURE REVIEW

2.1. Introduction

As shown in Figure 1.1, trashracks typically comprise of vertical and horizontal structural members that support closely spaced vertical bars (hereafter referred to as trashrack bars). Most often, the horizontal members are spaced more closely than the vertical members, or the vertical members are omitted altogether (Lemon *et al.* [2]). This chapter begins by outlining the various ways of classifying trashracks. Section 2.3 provides a summary of various equations that have been proposed to quantify head loss produced by trashracks. The section also examines the effects of bar spacing, bar shape and bar depth, concurrently with the effects of approach flow on trashrack head losses. Section 2.4 provides a review of numerical studies of flow through trashrack. In section 2.5, the usage of fine trashrack and its implications are outlined.

2.2. Classification of Trashracks

Trashracks have been classified in various ways. According to Wahl [3], trashracks are classified into three types depending on the basis of construction and installation methods. The types of trashracks are identified as end-bearing, side-bearing and integral trashracks. For the end-bearing trashracks, the trashrack bars run from the top to the bottom and they individually carry the loads into the trashrack structure. The side-bearing trashracks are made up of excessively long trashrack bars. The side-bearing trashrack uses one or more lateral support beams to make the load spans of the trashrack bars shorter. The lateral beams carry the load into guides or grooves in the trashrack structure. The integral trashracks are a combination of several panels made up of trashrack bars

with lateral support beams or members. The panels are constructed by either welding or bolting the support members together. The support members make up a multisided, rigid frame that carries the loading into the trashrack supporting structure. Integral trashracks are usually used for deeply submerged intakes and are not intended to be replaced.

On the basis of bar spacing, trashracks may be classified as coarse trashracks and fine trashracks. According to Mosonyi [4], the interspacing of the bars of coarse trashracks varies between 100 mm and 500 mm. Their existence at the turbine intakes is to prevent debris from entering the hydraulic units to cause damage to the turbine. Tight-spaced trashracks are called fine trashracks. The interspacing of the bars of fine trashracks varies from 15 mm to 100 mm. The primary function of the fine trashracks is to retain fish, and for this reason they are also called fish screens. Fine trashracks are mounted almost generally in a slanting position at an angle of about 50° to 80° to the horizontal. The advantage of this orientation is to facilitate cleaning and to lessen the head loss. With regards to bar depth, trashrack bars are generally classified as short bars if $L/s < 3$ and as long bars if $L/s > 3$ (Escande [5]).

2.3. Head Losses in Trashrack

Trashracks at the intakes of hydraulic generating unit produce head loss which reduces power production. Studies have indicated that head loss increases significantly as the spacing of the bars decreases, direction of approach flow is oblique to the trashrack and approach flow increases. Flow through unsubmerged trashrack is marked with a considerable change in water level before and after trashrack. Figure 2.1 is an illustration

of the differential water level before and after the trashrack. The difference in water levels does not correspond to the energy loss (Spangler [6] and Meusburger *et al.* [7]). This is because the average velocity before the trashrack is essentially different from the average velocity after the trashrack. Thus, there is a consequential velocity head difference corresponding to the decrease in height of the water surface. The energy loss through trashracks can be estimated by application of the energy equation. Thus, the head loss, Δh (Figure 2.1a) is given as:

$$\Delta h = h_1 - h_2 + \frac{1}{2g}\left(U_1^{\,2} - U_2^{\,2}\right) \qquad 2.1$$

where h_1 is the upstream potential head, h_2 is the downstream potential head, U_1 is the average velocity at the upstream of the trashrack and U_2 is the average velocity at the downstream of the trashrack. In Eq. (2.1), Δh corresponds to the difference in the energy grade line upstream (EGL_u) and downstream (EGL_d) of the trashrack (Figure 2.1a).

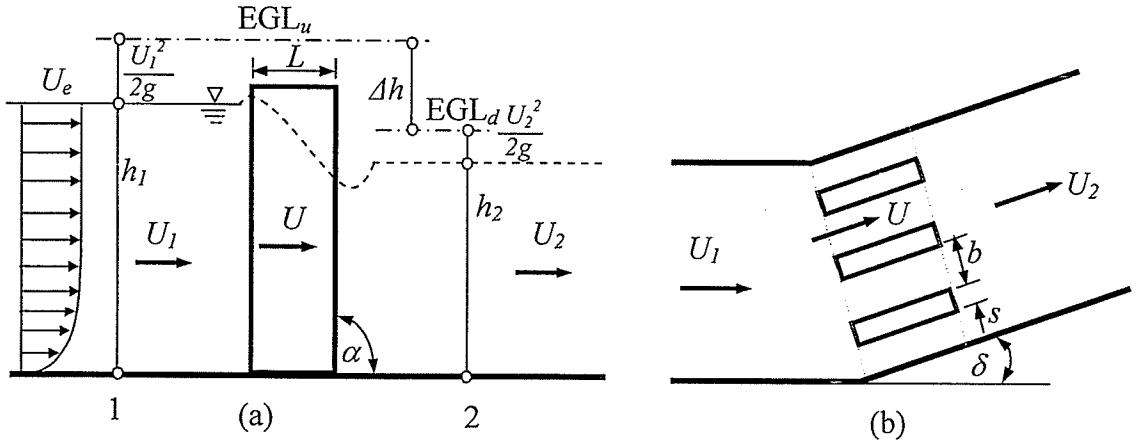

Figure 2.1: Side (a) and plan (b) views of a typical trashrack model.

Apart from the energy equation, various correlations have been formulated by various researchers for quantifying the head loss produced by trashrack. These correlations are

Table 2.1: Summary of studies on trashrack and head loss equations

Author	Flow Condition	Bar Geometry Study	Equation
-	-	Independent of bar shape & angle of trashrack	$\Delta h = (1.45 - 0.45R - R^2)U^2/2g$ ..... 2.2 $R = A_{net}/A_{gross}$, U = velocity through net flow area
Kirschmer [8]	up to 0.82 m/s	Rectangular, streamlined, circular, round edge, tapered and circular section bars	$\Delta h = \phi(s/b)^{4/3}(U_1^2/2g)\sin\alpha$ ..... 2.3 ϕ = 2.42, for rectangular bar ϕ =1.83, for rectangular bar with round edge ϕ = 0.76, for streamlined bar ϕ = coefficient based on bar shape
Spangler [6]	up to 0.72 m/s h_l = 1 m δ = 0°, 30°, 45°, 60°	Rectangular, streamlined, circular, round edge, tapered and circular section bars	$\Delta h = \beta[(1-\varepsilon)/\varepsilon]^{4/3}(U_1^2/2g)$ ..... 2.4 β = 2.34, for rectangular bar β = 1.77, for rectangular bar with round edge β = 0.71, for streamlined bar β = coefficient based on bar shape flow ratio, $\varepsilon = b/(b+s)$
Meusburger *et al.* [7]	0.5 m/s – 1.5 m/s	Rectangular bar	$\Delta h = k_F(1 + B\tan\delta)p^C(b/L)^D(U_1^2/2g)\sin\alpha$ ..... 2.5 k_F = 2.42, form factor for rectangular bar
Fellenius & Lindquist [9]	0.68 m/s, 0.98 m/s 1.00 m/s, 1.12 m/s	Rectangular, round edge, trapezoidal sections	$\Delta h = kp^2(U_1^2/2g)\sin\alpha$ ..... 2.6 k = form factor blockage ratio, $p = (A_h + A_v)/A_t$
Fellenius & Lindquist [9]		Tapered sections	$\Delta h = kp^2(U_1^2/2g)\sin^{3/2}\alpha$ ..... 2.7 k = form factor
Mosonyi [4]	-	Streamlined bar	$\Delta h = (1/\varepsilon^2 - 1)^2 U_1^2/2g$ 2.8
Escande [5]	-	$L/s < 3$	$\Delta h = (1/[\mu\varepsilon] - 1)^2 U_1^2/2g$ 2.9
Escande [5]	-	$L/s > 3$	$\Delta h = [[(1-\mu)/\mu]^2 + (1-\varepsilon)^2]/\varepsilon^2(U_1^2/2g)$ 2.10
Orsborn [10]	0.6 m/s – 3 m/s, ε = 0.25, 0.5, 0.75	Rectangular bar, $L/s < 3$	$\Delta h = (1.35/\varepsilon^{7/6} - 1)^2 U_1^2/2g$ 2.11
Orsborn [10]		Rectangular bar, $L/s > 3$	$\Delta h = (1-\varepsilon)/\varepsilon^{7/3}(U_1^2/2g)$ 2.12

summarized in Table 2.1. In this table, b is the clear spacing between bars, L is the bar depth in the flow direction, s is the bar thickness, B is a coefficient for the horizontal angle of inflow (B = 0.65), C is a coefficient applicable to the blockage ratio (C = 1.33), D is a coefficient applicable to the ratio of b/L (D = - 0.43), A_h is the area blocked by horizontal spacing elements, A_v is the area blocked by the bars, A_t is the total area of the trashrack field, U_1 is upstream average velocity, α is the angle of inclination of the trashrack with the horizontal, δ is the horizontal angle of inflow and μ is the coefficient of contraction. Equation (2.2) is the correlation that is commonly used by the Bureau of Reclamation (Wahl [3]) to estimate head loss through trashrack.

2.3.1. The Effects of Bar Spacing on Head Loss

The permissible spacing for bars of trashracks is determined by the type of turbine, dimensions of the turbines (defined by the discharge capacity), peripheral speed of vanes depending upon the specific speed and the head, and the debris present at the site. According to Doland [11], propeller-type turbines have relatively large spaces between the blades. For this reason, they can pass, without damage, larger sized pieces of debris than the smaller-spaced and more intricate-shaped blades of the Francis-type turbine. Ecological demands have also put constraint on the spacing between trashrack bars. For instance, the power plant situated at river Fulda in the north-east of the city of Kassel in Germany was originally protected with a trashrack having a clear spacing of 60 mm. However, because of ecological demands, the original trashrack was replaced by a new trashrack having reduced clear spacing of 20 mm (Meusburger *et al.* [7]).

Spangler [6] investigated trashracks with their clear spacing between adjacent bars varied from 8.7 mm to 64.5 mm. It was found that trashrack with 8.7 mm clear bar spacing produced the highest coefficients of resistance. The coefficient of resistance also increased with increasing angle of approach. The author reasoned that the rise of the coefficient of resistance was associated with an enlargement of dead-water area which formed on one side of the trashrack. Contrarily, the trashrack with highest clear spacing of 64.7 mm produced the lowest coefficients of resistance.

2.3.2. The Effects of Bar Shape on Head Loss

Most component bars in trashracks at hydraulic intakes frequently have sharp-edged rectangular cross-sectional shapes. However, sharp-edged rectangular shapes are susceptible to flow-induced vibration (Knisely [12]). Because of economics, ease of construction or structural requirements, often these non-aerodynamics geometries are employed. Nevertheless, rectangular steel bars are preferred over round bars, since round bars are highly susceptible to clogging and even more vibration than rectangular bars. According to Wahl [3], objects pass partially through trashracks that are made of round bars and become firmly lodged in between the bars.

Spangler's [6] investigations revealed that rectangular cross-section bars produced the highest coefficient of resistance to the flow at various angles of approach velocity. He also noted that all the rectangular bars used for the experiment had the same coefficient of resistance to the flow at zero angle of approach, irrespective of the thickness and depth of the bars. However, as the angle of approach flow was increased, the coefficient of

resistance increased with bar thickness. Spangler [6] also observed that the losses at trashrack decreased as the corners of the leading and/or trailing edges of the bars were rounded. The author concluded that the increase in head loss for round leading edge bars was associated with freeing of the flowing water at the upstream side of the bars (at larger angle of approach flow). Spangler [6] observed the least coefficient of resistances for the streamlined shape bars, irrespective of the angles of approach flow. The author, however, remarked that streamlined shape bars cannot easily be kept free from debris by the use of a cleaning machine.

2.3.3. The Effects of Bar Depth on Head Loss

Kirschmer's [8] study indicated that there is slight variation in head loss coefficient for rectangular bars of greater depth. The results of Spangler [6] also showed that bar depth has strong effect on head loss coefficient as the angle of approach flow is larger than 0°. Spangler [6] obtained the same coefficient for all rectangular bars at 0° to approach flow, irrespective of their depth. However, as the angle of approach flow increased, the coefficient of resistance to flow also increased, signifying a corresponding increase in head loss. This increase in head loss was high for bars with shorter depth. Escande [5] and Orsborn [10] investigated head losses associated with trashrack bars of different depths. Their study led to the formulation of two separate equations for determining head loss caused by relatively short ($L/s < 3$) and long ($L/s > 3$) bars respectively (Table 2.1). Orsborn [10] argued that for short bars, the flow after separation from the leading edge does not reattach to the sides of the bar within the trashrack (Figure 2.2), resulting in higher head losses. On the other hand, increasing the bar depth from square reduces the

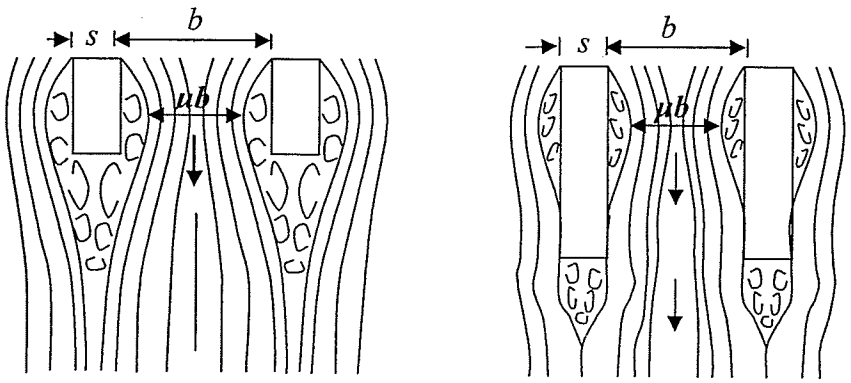

(a) Short bars (b) Long bars

Figure 2.2: Flow around short and long trashracks bars

head loss since a greater portion of the wake cavity is filled by the bar, and energy dissipation is thereby reduced. The author argued that when the flow expands to the sides of the bars, the trashrack head loss increases and consists of a sudden contraction loss plus a sudden expansion loss. When this condition is reached, any additional increase in bar depth does not greatly increase the total head loss for blockage ratios up to 0.50.

2.4. Numerical Studies on Trashracks

Only a few numerical analyses of flow through trashracks have been performed to date. Hermann *et al.* [13] and Meusburger *et al.* [14] applied direct numerical simulation (DNS) and k-ε turbulence models to conduct detailed analysis of flow through arrays of rectangular bars for a range of blockage ratios, $0.18 \leq p \leq 0.54$. The velocity was varied from 0.29 m/s to 0.87 m/s and 0.50 m/s to 1.5 m/s, respectively, in the studies by Hermann *et al.* [13] and Meusburger *et al.* [14]. The DNS was performed on bars aligned to the flow, and only small part of the trashrack domain (typically 3 or 4 bars) was

simulated. The DNS produced head losses that compared well with measured values at low blockage ratios but produced higher losses than experimental data at higher blockage ratios. The authors attributed the discrepancies to insufficient grid resolution in the turbulent boundary layer zone close to the bars. The results from k-ε turbulence models were in good agreement with the measured data, especially at higher blockage ratios.

2.5. Fine Trashracks

Fine trashracks are typically used where fish protection against turbine mortality or injury is a prime concern. Fish such as salmon and eel suffer severe mortality from turbine blades, especially when they are migrating into the sea during summer. This has compelled the authorities to enact laws for the usage of fine trashracks or screens at the intakes of hydro-power terminals to abate turbine mortality of fish (Mosonyi [4]). Fine trashracks, on the other hand, are very expensive and they pose higher resistance to flow which cause excessive head losses. However, according to Mosonyi [4], the protection of fish by fine screens is inadequate since fish are pressed by the flow against the screen and are not able to get freed. Yeh and Shrestha [15] have also reported the pressing of small fish against the screen surface, when they examined flow through screen. Eels and salmon are very often caught by screen-bars and are killed during cleaning operations (Mosonyi [4]). For example, many salmon were reported dead at the screen of the Rheinfelden power plant in Germany. Consequently, the original spacing of 15 mm was increased to 38 mm. Similar experience was gained regarding eels at the power plants of the Main River (Germany), where the original 20 mm spacing of the bars was increased.

According to Mosonyi [4], with regards to protection of fish, it is important to consider the injury and extent of damage to fish caused by the runner vanes. Another important factor to consider is the ability of fish to withstand the sudden drop in pressure that occurs as the flow passes through the turbine. It has been a practice at some power plants in the northern states to employ only coarse trashracks in the winter, whereas fine trashracks are used only in the summer season when fish are migrating towards the sea. The use of coarse trashrack is advantageous to fish protection, if fish passage through the turbine is permitted. Practically, the omission of the screen is guaranteed provided the loss in fish caused by the operation of the screen is undoubtedly greater than that due to the turbines.

CHAPTER 3: PRINCIPLES OF PARTICLE IMAGE VELOCIMETRY AND ACOUSTIC DOPPLER VELOCIMETER

3.1. Introduction

Particle Image Velocimetry (PIV) is a non-intrusive optical measurement technique that provides simultaneous whole field velocity measurements at several positions in a plane. Compared to other measurement techniques such as Pitot tubes, hot wires and laser Doppler anemometry (LDA), PIV can capture the velocity and direction information in many points over a plane of fluid flow almost instantaneously with high accuracy. Because it is a multi-point technique, it is very well suited for investigation of coherent flow patterns. The PIV is also well suited for estimating velocity gradients and derived quantities such as vorticity and the various terms in the transport equations for turbulent kinetic energy and Reynolds stresses. Due to these attractive features, PIV has been applied in many areas of fluid mechanics and aerodynamics research in the recent past.

Acoustic Doppler Velocimeter (ADV) is a single-point, high-resolution, current meter that measures flow velocity. Some inherent advantages of ADV are 3D velocity measurements in a remote sampling volume, invariant factory calibration, simple operation, direct calculation of turbulent quantities such as Reynolds stress, and excellent low-flow performance. These attractive features of ADV dictate its application to measure velocity in a wide range of environments including laboratories, rivers, estuaries, and ocean. Section 3.2 of this chapter outlined the basic principle of the PIV and the various components of a typical PIV system. In section 3.3, the basic principle of ADV is outlined in addition to that of point gauge.

3.2. Particle Image Velocimetry

3.2.1. Planar PIV

A typical experimental setup using a two dimensional or planar PIV is shown in Figure 3.1. The setup consists of an optically transparent test-section containing fluid seeded with light reflecting particles, a laser to illuminate the region of interest, a CCD camera to record the illuminated particles, a synchronizer to control the camera and laser, and a computer with suitable software to record, store and post-process the recorded images.

In PIV measurements, the flow field is seeded with small light scattering particles (called seeding particles) that are presumed to faithfully follow the fluid motion. These seeding particles are then illuminated by two pulses of laser sheet separated by a time delay, Δt. The light scattered by the seeding particles is recorded and two successive images are captured. The images are divided into a grid of small regions called interrogation areas. For each interrogation area, a numerical correlation algorithm (auto-correlation or cross-correlation) is applied to statistically determine the local displacement vector (Δs) of particles between the first and the second illuminations. It is assumed that all particles within an interrogation area have moved homogeneously between the two illuminations. The velocity, V, for a particular interrogation area is obtained from the expression $V = \Delta s/\Delta t$. A velocity vector map over the region of interest is obtained by repeating the correlation for each interrogation area over the two image frames captured. In this process, the time delay between laser pulses and the image capturing is synchronized. A detail description of the basic components of a PIV is presented in the following sections.

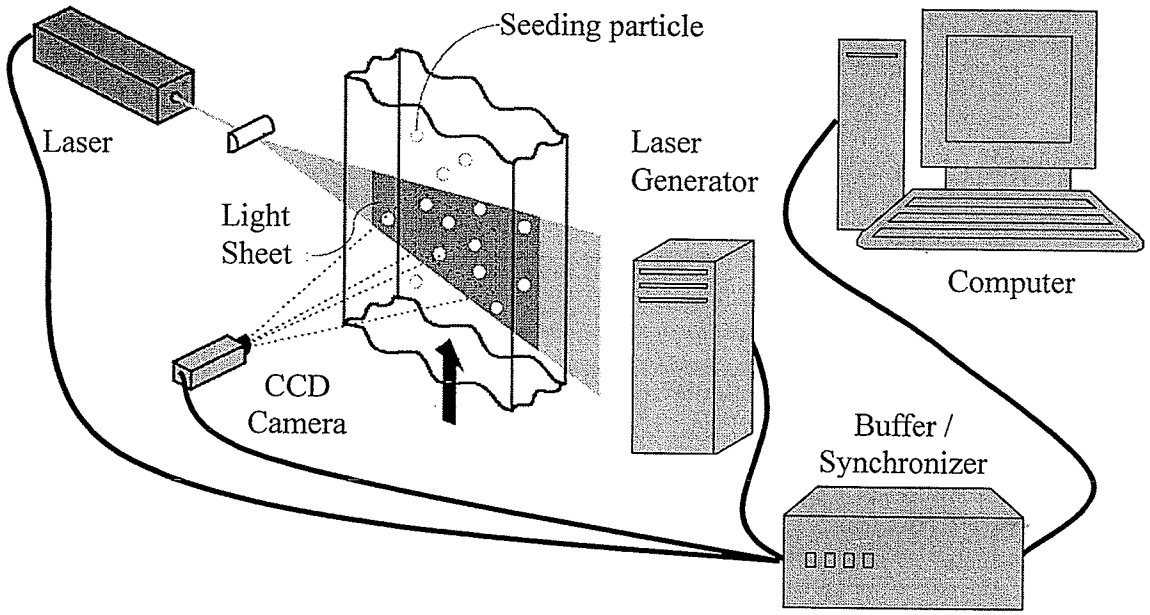

Figure 3.1: A typical experimental set-up of a planar PIV system.

3.2.2. Light Source

For PIV measurements, a high intensity laser is required to freeze the motion of the particles during image capturing. The fact that the whole field is illuminated and the camera captures the side-wards scattered light by the particles makes a high power laser necessary. Frequency doubled neodymium-yttrium-aluminum-garnet (Nd:YAG) lasers are commonly used for PIV measurements because these lasers provide monochromatic light with high intensity, which can easily be bundled into thin light sheets for illuminating and recording the seeding particles without chromatic aberrations (Raffel *et al.* [16]). Laser-emitted light is passed through a lens system to create a plane sheet of light to illuminate the region of interest. The length and width of the light sheet can be adjusted to the field of view required.

3.2.3. Seeding Particles

Seeding particles should have the ability to follow the fluid faithfully without disturbing the flow of the fluid but large enough to scatter sufficient light for them to be detected by the camera. Also, the seeding particles should be distributed homogeneously (Westerweel *et al.* [17]). Because PIV measures the velocity of the particle but not the fluid velocity, it is essential that the particles have certain hydrodynamic properties to ensure that they faithfully follow the flow. It is therefore imperative to consider the working fluid in selecting the seeding particle. Particles that have negligible settling velocity are desirable. According to Mei *et al.* [18], the settling velocity can be estimated from Stokes drag law for flow around a sphere under gravity and is given by,

$$v_s = \frac{(\rho_p - \rho_f) g d_p^2}{18 \mu_f} \qquad 3.1$$

where, ρ_p is the particle density, ρ_f is the fluid density, g is the acceleration due to gravity, d_p is the diameter of the particle and μ_f is the viscosity of the fluid. Settling is undesirable and can be minimized by using small particles and/or particles whose density is similar to that of the working fluid.

The ability of a particle to follow the flow is characterized by its response time. The response time is a measure of the tendency of the particles to attain velocity equilibrium with the fluid. The response time, τ_r, for the particle (for Stokes flow) is according to Raffel *et al.* [16] given by:

$$\tau_r = \rho_p \frac{d_p^2}{18 \mu_f} \qquad 3.2$$

The particles must also be good at scattering light to ensure that they are visible to the CCD sensor (Willert and Gharib [19]). The particle size and shape, the refractive index and the wavelength of radiation are the factors that affect the light scatter by a particle. A variety of seeding particles are commercially available ranging from a few microns to hundreds of microns. It should be noted that the ultimate goal in particle selection is to obtain the most efficient scattering and maximize the light intensity of the sensor. The widely used tracer particles in liquids are polyamide seeding particles (PSP), silver-coated hollow glass spheres, hollow glass spheres, polystyrene latex and fluorescent polymer particles, to mention a few.

3.2.4. Recording Medium

Two types of recording media are available: the CCD camera and photographic film camera. The CCD camera is the most widely employed recording device for PIV because of its several advantages over the photographic film cameras. These advantages include higher frame rates, superior sensitivity to light and possibility of on-line image analysis. However, the photographic film cameras do offer higher resolution. The major component of a CCD camera is the CCD sensor which consists of an array of detectors called pixels. The CCD camera employed in the PIV studies generally uses high-performance progressive scan interline CCD chips. The chip consists of an array of photosensitive cells and an equal number of storage cells. After the first laser pulse is triggered, the first image is acquired and immediately transferred from the photosensitive cells to the storage cells. Later, when the second laser pulse is triggered, the photosensitive cells are available to store the second image. In this case, the storage cells

contain the first image and the photosensitive cells contain the second image. Then both images are transferred sequentially from the camera to the computer for storage. With this technique, the exposure interval, Δt can be reduced to less than 1 microsecond.

3.2.5. Methods of Correlation in PIV

As mentioned earlier, the images recorded by the CCD camera are sub-divided into smaller regions called interrogation areas. For each of the interrogation areas, the images at the first and second frames are correlated to obtain an average displacement vector. This results in a vector map of average displacements for all the interrogation areas. The most commonly used correlation methods are auto-correlation and the cross-correlation/adaptive-correlation.

Auto-correlation allows the particles in an interrogation area to be correlated with themselves. This results in a large central peak (the self-correlation peak) in the correlation plane along with two displacement peaks, one on each side of the central peak. The distance from the central peak to either of the displacement peaks corresponds to the average particle displacement in the interrogation area. Because of the presence of the self-correlation peak, particle displacements less than two to three pixels cannot be detected. This reduces the dynamic range of the auto-correlation technique. Another drawback of the auto-correlation is its 180-degree directional ambiguity.

In cross-correlation, particles in two different interrogation areas belonging to two different images at the first and second frames are correlated. Because the order of image

recording is known, directional ambiguity of the flow is no longer a concern. With the cross-correlation method, two sequential images of the flow field with a specific time between them are considered as two spatial signals. The first image of the particles at $t = t_1$ is considered the input signal and the second image at $t = t + t_1$ is the output signal. The detail of this method and the computational implementation are given in Willert and Gharib [19] and Raffel *et al.* [16].

The adaptive-correlation algorithm is an advanced type of cross-correlation. It is an iterative method which relies on the knowledge of the actual velocity spatial distribution, which is not known a *priori* and is the objective of the measurement procedure itself. Therefore, an initial guessed offset value is used to introduce an offset from the first window (the interrogation area in the image frame from laser pulse one) to the second window. The result of each single interrogation is validated and used as an input to evaluate the interrogation parameters for the subsequent iteration. The process terminates when a convergence criterion is fulfilled or after a prescribed number of iterations. The use of adaptive correlation helps in two major ways. First, the signal strength is raised due to the capture of the in-plane dropout. In-plane dropout occurs because during the time between the two light pulses some of the particle images leave the interrogation area and are lost. This loss of particles reduces signal strength and the number of successful vectors that can be obtained. Secondly, a refinement of the interrogation area is possible because an adaptive window offset may be applied, again producing a successful signal. The adaptive correlation technique finds applications in large area of PIV; flows with high velocity gradients, and flows with inhomogeneous or sparse seeding density.

3.2.6. Optimizing PIV Measurements

The combination of laser energy, camera magnification and light sheet dimension needs to be optimized in order to obtain results from a PIV system with high accuracy. Even under ideal experimental conditions, a PIV vector map may contain spurious vectors. These spurious vectors emanate from interrogation spots where signal-to-noise ratio is less than unity. That is, a noise peak is higher than the signal peak. Keane and Adrian [20] focus their study on the detection probability (i.e., the percentage of valid vectors). To improve the signal-to-noise ratio, they recommended the interrogation areas be large enough to accommodate a sufficient number of particles, but small enough so that one vector describes the flow. It was also recommended that the time separation should be set so that the variation in particle displacements within the interrogation cell is less than the particle image diameter. The particle size should be selected such that the particle image size is approximately two pixels when imaged by the digital camera (Raffel *et al.* [16]). The particle image diameter, d_{image}, is given by:

$$d_{image} \approx [d_p^2 M^2 + (2.44 f_{\#}(1+M)\lambda)^2]^{0.5} \qquad 3.3$$

where d_p is particle diameter, $f_{\#}$ is the *f*-number of the lens, λ is the wavelength of the laser light, and M is the magnification factor of the camera. Raffel *et al.* [16] suggested that when the image diameter becomes too small there is insufficient information to make effective use of sub pixel interpolation because there is likelihood of biasing data towards integer pixel values. Sub-pixel interpolation is used to increase the resolution or accuracy when detecting the position of the correlation peak which makes it possible to determine displacements with an accuracy of fractions of a pixel.

The seeding density is dependent on the type of PIV method used. For the two-frame cross-correlation method, Willert and Gharib [19] showed that to obtain a high valid detection probability the particle image density should be larger than 6. Using very high particle image densities, large particle image diameters, and small interrogation cell sizes will reduce the error due to gradients. The movement of the particles can only be tracked as long as they remain within the same interrogation area during both exposures. Also, the particles should not traverse more than one fourth of the side length of the interrogation areas between exposures to keep the number of particles that leave the interrogation area down.

3.3. Acoustic Doppler Velocimeter

3.3.1. The 3D ADV

A typical experimental setup using a three-dimensional ADV probe is shown in Figure 3.2. The setup consists of a transparent test-section containing fluid, an ADV probe, a processor, and a computer with suitable software to record, store and post-process the recorded data. The operation of the ADV requires that the fluid naturally contains particulate matter or scatterers, which are assumed to be moving at velocities similar to the fluid. The 3D ADV uses an acoustic pulse to remotely measure the three components of water velocity at a single point using a principle called the Doppler effect. The ADV is implemented as a bistatic acoustic Doppler system and consists of a transmitter and three receivers. The three receivers are positioned in 120° increments on a circle around the transmitter. The probe of the ADV is submerged in the flow to be measured and the receivers are slanted at 30° from the axis of the transmit transducer. The transducers are

positioned and oriented such that their acoustic beams all intercept at a common sample volume located at about 5 cm or 10 cm in front of the transmitter transducer, which ensures non-intrusive flow measurements.

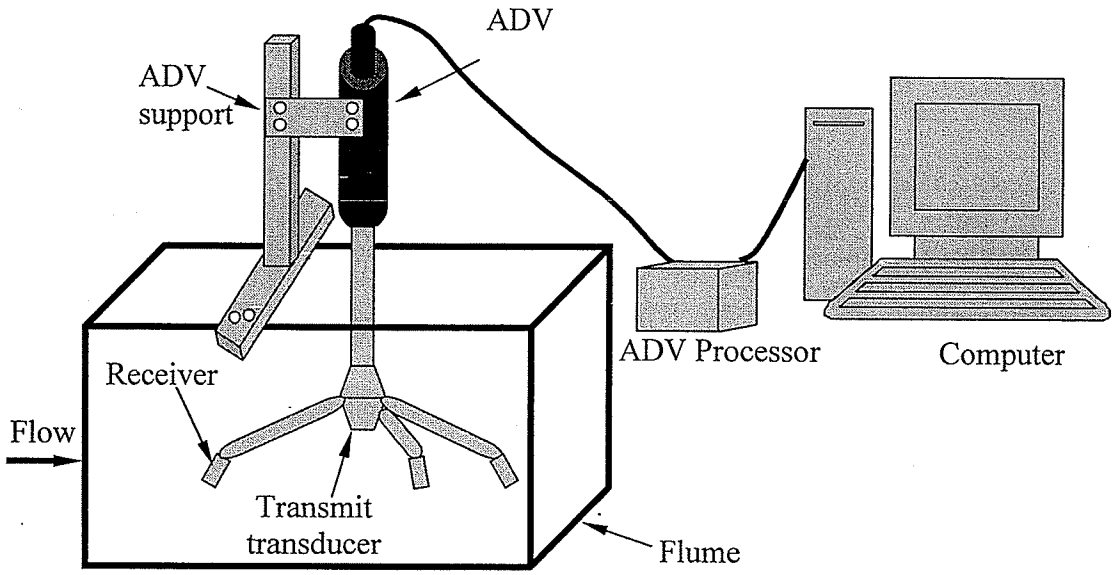

Figure 3.2: A typical experimental set-up of a 3D ADV system.

The transmitter generates a short pulse of sound at a known frequency, which propagates through the liquid along the axis of its beam. As the pulse passes through the sampling volume, the acoustic energy is reflected in all directions by particulate matter. In general, for excellent operation, the ADV requires a minimal amount of scattering material, typically 10 mg/L (Sontek ADV Manual). Some portion of the reflected energy travels back along the receiver axis, where it is sampled by the ADV and processed by the electronics to measure the change in frequency. The Doppler shift measured by one receiver is proportional to the velocity of the particles along the bistatic axis of the receiver and transmitter. The bistatic axis is located halfway between the center axes of

transmitted and received beams. It should be noted that in ADV, each transmitter/receiver pair measures the projection of the liquid velocity onto its bistatic axis. The velocity measured by each receiver is referred to as the bistatic velocity. Bistatic velocities are converted by the ADV to *x-y-z* (Cartesian) velocities using the probe geometry. The *x-y-z* velocities give the 3D velocity field relative to the orientation of the ADV probe.

3.3.2. Components of ADV

The ADV consists of three basic components: the probe, the signal conditioning module, and the processor.

ADV Probe Configuration: The ADV probe configuration is determined by a combination of four factors: sampling volume location, coordinate resolution (3D or 2D), sensor mounting, and sensor orientation. The probes can be constructed with almost any combination of these options. The ADV sampling volume is located at a distance from the tip of the probe to ensure non-intrusive flow measurements. The acoustic sensor can be mounted on a 25-cm rigid stem or on a 100-cm flexible cable. The down-looking sensor orientation is ideal for measurements close to the bottom. Side-looking probes are typically used in wave flumes to avoid flow interference. If the primary interest is to measure velocity in the surface layer (under a layer of ice) or under structures (near the bottom of a vessel or structure.), an up-looking probe may be preferred.

ADV Signal Conditioning Module: The standard ADV signal conditioning module is a cylindrical acetyl (Delrin) housing, which contains low-noise receiver electronics. The probe is attached at one end of the conditioning module while the other end is connected

to the processing module/processor via a high-frequency cable up to 20-m long, using a 16-pin wet-mateable connector.

ADV Processor: The ADV processor is a set of three printed circuit cards that perform the signal generation and processing required for the ADV to make velocity measurements. This includes generating electrical signals that are converted to acoustic energy at the transducers, digitizing the return signal, performing Doppler processing to calculate velocity, and averaging samples together before data output. The ADV processor operates from DC power and is typically connected to a computer running data acquisition software. It can also be integrated with a variety of data acquisition systems using either serial communication or the analog output voltages.

3.3.3. Method of Pulse-Coherent Processing in ADV

The pulse-coherent or pure-coherent processing technique requires that the ADV sends two pulses of sound separated by a time lag so that the phase of the return signal from each pulse is measured. The change in the phase divided by the time between pulses is directly proportional to the velocity of the particles in the water. The pulse-coherent processing is used because it provides the best possible spatial and temporal resolution. Pulse-coherent processing, however, has inherent limitation on the maximum velocity that can be measured. This is because pulse coherent processing measures the phase of return signals. The phase measurements are limited to a range of $(-\pi, \pi)$. If the phase exceeds these limits, it will 'wrap around' (that is, if the phase increases to just above π, the ADV measures a phase of $-\pi$). This is very often referred to as an ambiguity jump,

where, for example, the ADV will measure a negative velocity rather than the true, larger positive velocity. The maximum ambiguous velocity is a function of the time lag between the two pulses. The ADV offers a choice of a number of pre-set velocity ranges (standard settings are ±3, ±10, ±30, ±100, and ±250 cm/s), each of which corresponds to a particular pulse lag. The instrument noise level scales directly with the velocity range setting (higher velocity ranges have a higher noise for each sample). It is therefore necessary to select the lowest range that meets the requirements of the particular experiment. Pulse-coherent processing affects the ADV operation in two other situations. When making near boundary measurements, there is a potential that the reflection of one pulse from the boundary could interfere with the other pulse. Secondly, the ability to adjust the time lag between pulses gives the ADV excellent performance for applications with low flow velocities.

3.3.4. Point Gauge

A point gauge consists of a downward sharply pointed, movable metal rod connected to a graduated scale. The pointed rod is slowly raised or lowered using a rack and pinion gearing system until the point just makes contact with the water surface. The graduated scale is then read off to obtain the distance between the water surface and the point gauge zero reference elevation. In order to get absolute water level elevations relative to the model datum, the elevation of the point gauge zero reference must be determined. A potentiometer can be attached to the point gauge to partially automate the recording of data.

CHAPTER 4: EXPERIMENTAL TECHNIQUE

4.1. Introduction

In this chapter, the experimental facility, the test models, the PIV system and the ADV system employed, respectively, for small-scale and large-scale measurements and the measurement procedure are described. The chapter also provides summary of test conditions for the small-scale and large-scale trashrack models. Section 4.2 describes the experimental technique that was used for small-scale measurements. In section 4.3, the experimental technique that was used for large-scale measurements is described.

4.2. Small-Scale Trashrack Models

4.2.1. The Water Tunnel

The water tunnel used in the present study was designed and constructed by Engineering Laboratory Design, Inc., Minnesota, U.S.A. A schematic view of the water tunnel is shown in Figure 4.1. It consists of a flow conditioning section, test section, circulating pump, variable speed drive, piping, supporting framework and filtering station. The overall dimensions of the unit are: 5370 mm in length, 1822 mm in height and 1435 mm in width. The settling chamber upstream of the contraction is fitted with perforated steel plates to ensure minimal disturbance. A six-to-one contraction, with a symmetrical cross section, is used prior to the working section to further reduce the turbulence intensity by accelerating the mean flow. The test section was fabricated using Super Abrasion Resistant® (SAR) clear acrylic to facilitate optical access and flow visualization. The interior dimensions of the test section are 200 mm wide by 200 mm high by 2500 mm long. The pump is belt driven by a 25 hp, 1750 rpm, and 600 V AC 3-phase 60 Hz motor.

A 25 hp transistor inverter type variable speed controller regulates the speed of the motor that drives the pump. A filter system is furnished as a means of removing dye concentrations and other contaminants from the system's water. The filtration can be activated at any time, but it is not operated during experiments.

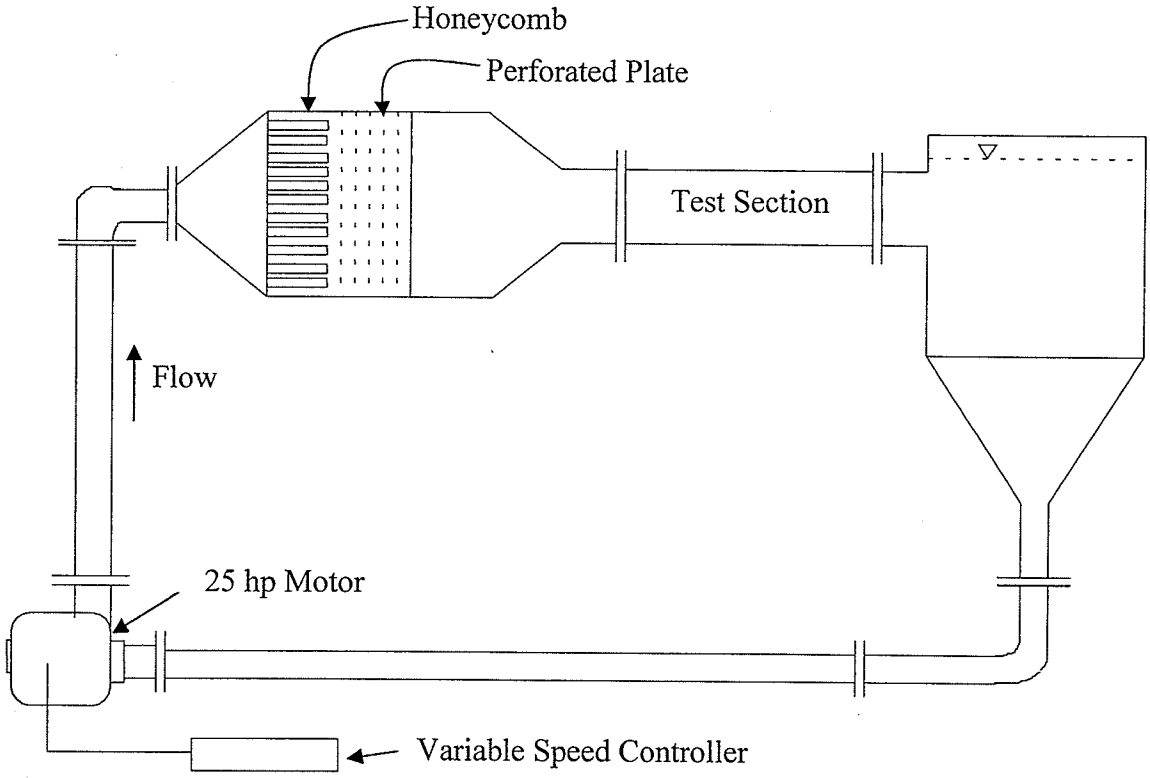

Figure 4.1: Schematic of the water tunnel (not drawn to scale).

4.2.2. Inserted Test Section

A provisional test section made from 6 mm thick acrylic plate was inserted into the main water channel to hold the array of bars in place. The insert was 2500 mm long, 184 mm wide and 190 mm deep. The base of the inserted test section was screwed onto the floor of the main water channel. Figure 4.2 shows schematic diagrams of the side and plan views of the inserted test section, and also defines some of the flow nomenclature and the

Cartesian coordinate system used. As shown, x, y, and z are, respectively, in the streamwise, transverse, and spanwise directions; $x = 0$ is at the leading edge of the trashrack bars, $y = 0$ is on the channel floor and $x' = 0$ is at the trailing edge of the trashrack bars. The axes z' and z'' are, respectively, located on the edge and the centre of each bar, whereas z is located at the centre of the channel. The bars were mounted by screwing them onto the floor and to a provisional supporting bar provided on top of the walls of the inserted channel at $x = L/2$ (see Figure 4.2).

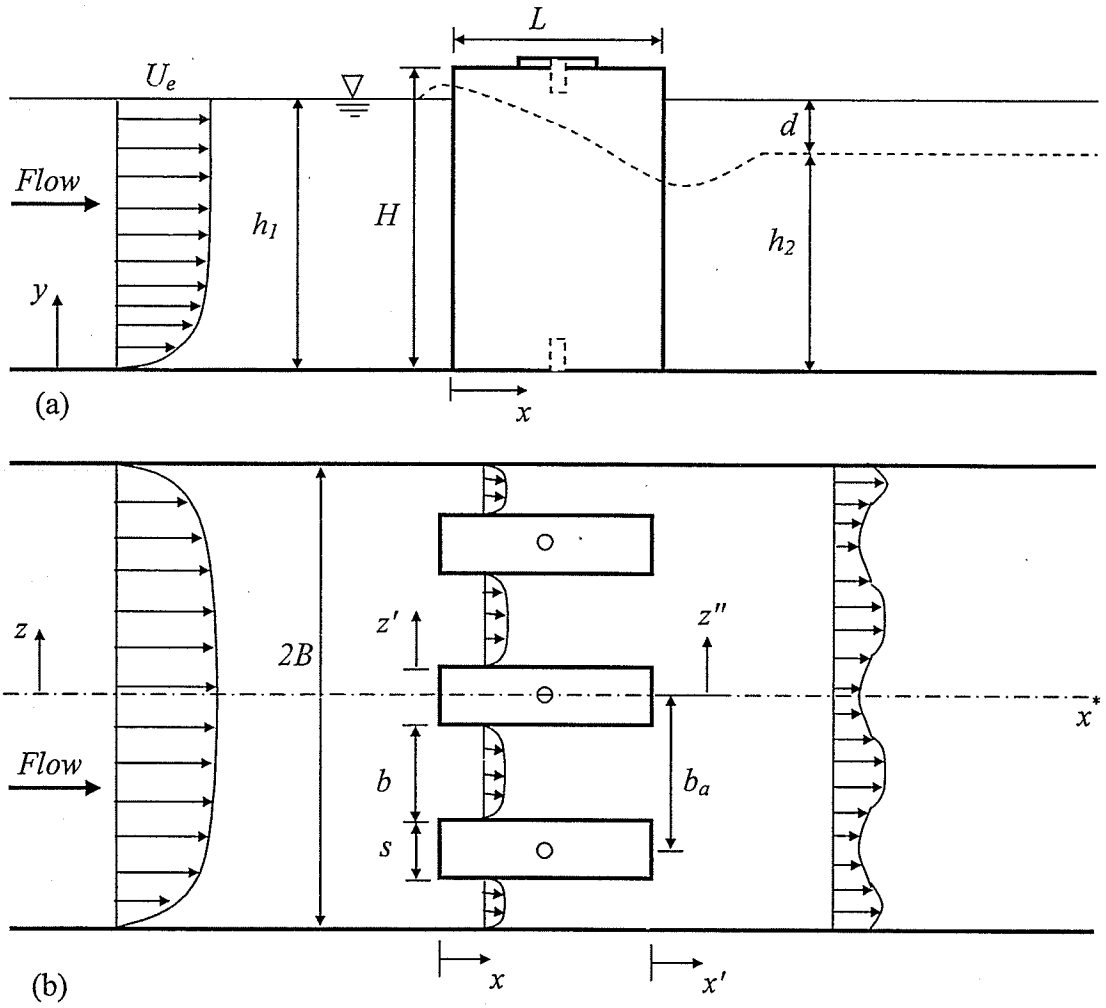

Figure 4.2: Schematic views of test sections: (a) side, (b) plan.

4.2.3. Test Models

In North American hydroelectric stations, arrays of rectangular bars that are typically 10 to 12 mm thick and 50 to 150 mm deep are widely used for construction of trashracks (Wahl [3]). For example, Manitoba Hydro, which is the main electrical utility in the Province of Manitoba, Canada, has more than 10 generating stations. At these stations, the depth of trashrack bars varies from 34.3 mm to 156.0 mm, the bar thickness varies from 7.6 mm to 12.7 mm, and the center-to-center-spacing between bars varies from 43.2 mm to 190.5 mm. In this study, the dimensions of the bars and centre-to-centre spacing of the bars were selected to meet some of the prevailing dimensions in use at Manitoba Hydro.

The bars for the present trashrack models were fabricated from clear acrylic plates. The bar height and thicknesses of each bar studied were, respectively, H = 190 mm, and s = 6 mm, 9 mm and 12 mm. The bar depth studied were L = 50 mm, 76 mm, 100 mm and 110 mm. Two different bar shapes were studied; rectangular and streamlined cross-section bars. The rectangular bars have sharp leading and trailing edges. The streamlined bars have the leading and trailing edge faired into a gradual smooth contour (NACA 0012). It should be noted that the bar depth and maximum thickness of the streamlined bars were 100 mm and 12 mm respectively, with L/s = 8.3.

Various centre-to-centre spacing (b_a = 40 mm, 51 mm, 63 mm and 70 mm) were tested. Depending on the test condition, 3, 4 or 5 bars were used (Figure 4.3). The corresponding blockage ratio, p, defined as the flow area occupied by the bars to the gross flow area

without the bars in place (that is, $p = ns/2B$, where n is the number of bars and $2B$ is the width of the inserted channel) were 0.10 and 0.15, 0.20, 0.26 and 0.33. In order to investigate the effects of bar inclination to the approach flow, $L = 76$ mm and $b_a = 70$ mm model was chosen. The bar inclination, θ was then varied from 0°, 6°, 9° to 12° as indicated in Figure 4.3b.

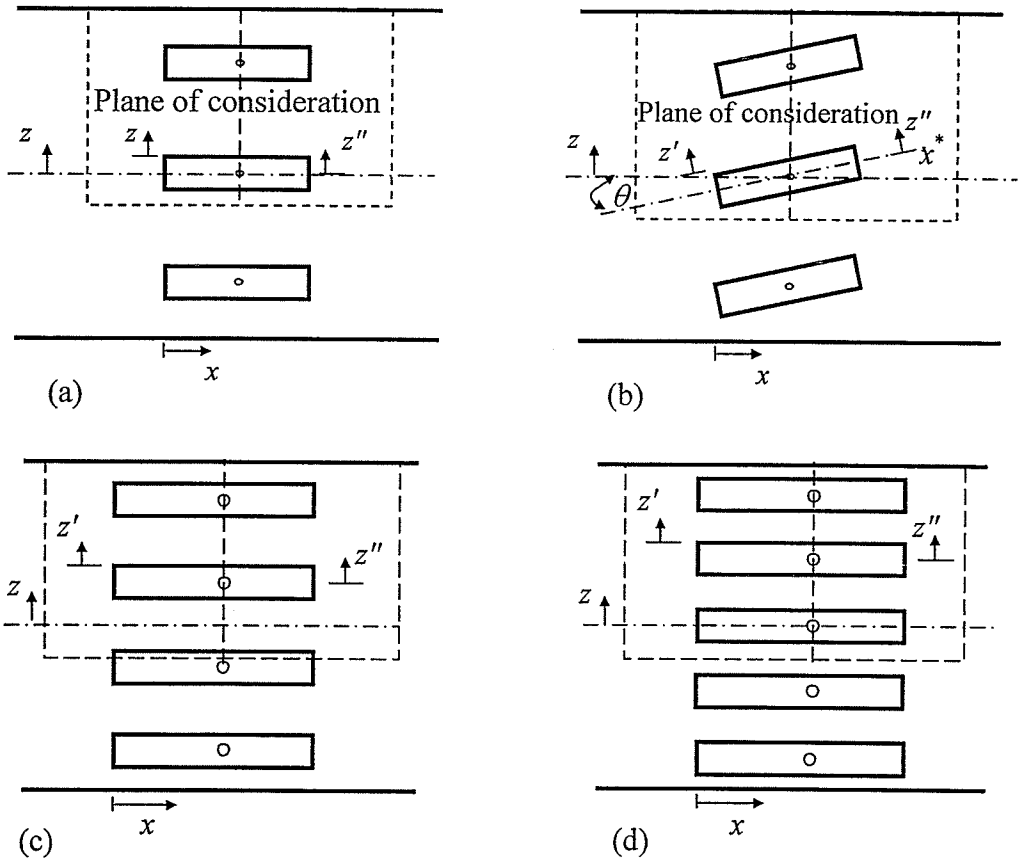

Figure 4.3: Schematic of the sectional view of the various trashrack models

4.2.4. PIV System

The flow was seeded with 5 μm polyamide seeding particles having a specific gravity of 1.03. The settling velocity and response time of the particles estimated from Eqs. (3.1) and (3.2) were 0.43 μm/s and 1.43 μs, respectively. The settling velocity is insignificant

compared to the streamwise mean velocity measured and the response time is very small compared to the sampling time employed in this study. This implies that the particles follow the fluid flow faithfully. An Nd-YAG laser of 120 mJ/pulse maximum energy and 532 nm wavelength was employed to illuminate the flow field. The laser sheet was located at mid-depth of flow, i.e., a distance $y = 90$ mm above the channel floor. A 12 bits HiSense 4M camera with 2048 pixels × 2048 pixels CCD array size and a 7.4 μm pixel pitch was coupled to a 60 mm AF Micro Nikkor lens. The images were acquired continuously through a buffer system onto 3.0 GHz Pentium 4 computer with 1 GB RAM and two 250 GD hard drives running on windows XP 2000 using Dantec Dynamics' FlowManager.

4.2.5. Measurement Procedure

The CCD digital camera was positioned perpendicular to the plane of the light sheet and focused to provide a 116 mm × 116 mm field of view. The laser pulse separation time, Δt was found based on the estimation that the particle displacement should be less than one quarter of the interrogation, using the following expression,

$$\Delta t = \frac{N \times d_{pitch}}{4MV_{\max}}, \qquad 4.1$$

where, N is the interrogation window size, d_{pitch} is the pixel pitch, M is the magnification factor and V_{max} is the maximum velocity of the flow. In addition to the condition stated above, particle displacement of at least 2 pixels was satisfied in order to ensure high signal-to-noise ratio and high quality data. The particle image diameter was estimated to be d_{image} = 14.7 μm (1.99 pixels) which is in good agreement with a value of 2.0 pixels recommended by Raffel *et al.* [16] to minimize peak locking.

For a given test condition, the volume flow rate was kept constant during all the measurements to maintain the upstream conditions as similar as possible. Measurements were made at Reynolds number based on the bar thickness and approach velocity which ranges from $3060 \leq Re_s \leq 9060$. The Froude number based on upstream water level and approach velocity varies from $0.19 \leq F \leq 0.57$. For each test condition, measurements were obtained for three or four x-z planes: far upstream of the bars (denoted as *P1*), two planes (*P2* and *P3*) around the bars and a plane (*P4*) far downstream of the bars. Note that the two separate measurement planes (*P2* and *P3*) were used for the longer trashrack bars in order to maintain the same spatial resolution. For a similar reason, only 2 or 3 of the trashrack bars domain was covered.

For each test condition in a given plane, 1190 pairs of instantaneous images were recorded at a sampling rate of 5.8 Hz. During the image acquisition, the PIV parameters were optimized to satisfy the condition that, for an interrogation window (IW) of 32 × 32 pixels with 50% overlap, the maximum particle displacement is less than one quarter of IW. The instantaneous images for each measurement plane were processed using

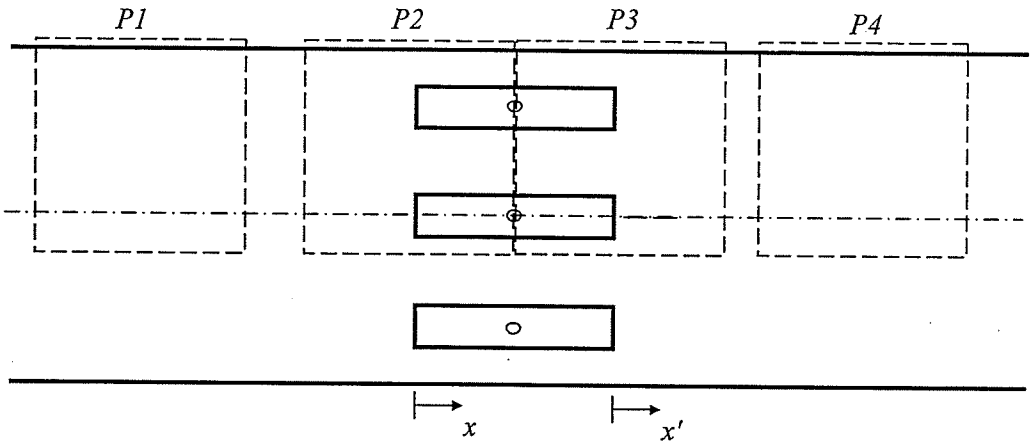

Figure 4.4: Planes of PIV Measurements

adaptive correlation option of FlowManager (version 4.50.17), commercial software developed by Dantec Dynamics. The PIV images were processed using 32 pixels × 32 pixels with 50% overlap interrogation area. This gave a spatial resolution of about 0.90 mm by 0.90 mm. It was found that the average number of particles in an interrogation window was 12 while the total number of vectors per image was 16129. Moving average validation was used during processing. Moving average validation validates or rejects vectors based on a comparison between neighboring vectors. The rejected vectors are then replaced by vectors estimated from surrounding values.

Because of losses through the bars, the water level dropped below the undisturbed upstream level. This is indicated by the dashed line close to the free surface in Figure 4.2a. For each test condition, the water depth was measured at mid-span along the channel at x intervals of 5 mm. From these data, the dip (d), relative to the undisturbed free surface upstream of the bars was calculated. It should be noted that h_2 was measured sufficiently far downstream of the bars where the free surface became horizontal, i.e., the water level became independent of x.

4.2.6. Summary of Test Conditions

The small-scale experiments were conducted in series. Tables 4.1, 4.2, and 4.3 provide a summary of the various test conditions denoted as *Series I*, *Series II* and *Series III*, respectively. In these tables, $Re_s = U_e s/\nu$ and $F = U_e/[gh_1]^{0.5}$ are, respectively, the Reynolds number and Froude number.

Series I: These experiments were conducted to specifically study the effects of bar inclination (θ), Reynolds number (Re_s) based on approach flow velocity and bar thickness, and Froude number (F) on head losses and the velocity field. In these experiments, the bar thickness (s = 12 mm), bar depth (L = 76 mm), bar spacing (b_a = 70 mm), and water depth (h_1 = 180 mm) were kept constant. The bars were inclined at an angle of θ = 0°, 6°, 9° and 12° while the approach flow velocities were U_e = 0.26 m/s, 0.52 m/s and 0.76 m/s. The test conditions are summarized in Table 4.1. In the first column of the table, the subscript after θ denotes the inclination of the bar in degrees while the subscript after U denotes the approach velocity in m/s. For example, in test $\theta_0 U_{0.52}$, the bar inclination, θ is 0° and the approach velocity, U is 0.52 m/s.

Table 4.1: Summary of Test Conditions for *Series I*

Test	θ	L (mm)	b_a (mm)	s (mm)	n	p	U_e (m/s)	U_1 (m/s)	Re_s	F
$\theta_0 U_{0.26}$	0°	76	70	12	3	0.20	0.26	0.25	3060	0.19
$\theta_0 U_{0.52}$	0°	76	70	12	3	0.20	0.52	0.50	6260	0.39
$\theta_0 U_{0.76}$	0°	76	70	12	3	0.20	0.76	0.73	9060	0.57
$\theta_6 U_{0.52}$	6°	76	70	12	3	0.20	0.52	0.50	6260	0.39
$\theta_9 U_{0.52}$	9°	76	70	12	3	0.20	0.52	0.50	6260	0.39
$\theta_{12} U_{0.52}$	12°	76	70	12	3	0.20	0.52	0.50	6260	0.39

Series II: In these experiments, the bar thickness (s = 12 mm), Reynolds number (Re_s) and Froude number (F) were held constant while bar depth, L, bar spacing, b_a, and number of bars were varied. The goal was to study the effects of blockage ratio and bar depth on head loss coefficient and the velocity field. The test conditions are shown in Table 4.2. In the first column of the table, SQ denotes rectangular bar with square leading and trailing edges, the subscript after L denotes the depth of the bar in mm while the

subscript after p denotes the blockage ratio. For example, in test SQ-L_{110}-$p_{0.20}$, the model is comprised of rectangular bars with bar depth, L is 110 mm and blockage ratio, p is 0.20.

Table 4.2: Summary of Test Conditions for *Series II*

Test	L (mm)	b_a (mm)	s (mm)	n	p	U_e (m/s)	U_1 (m/s)	Re_s	F
SQ-L_{50}-$p_{0.20}$	50	70	12	3	0.20	0.511	0.487	6130	0.38
SQ-L_{76}-$p_{0.20}$	76	70	12	3	0.20	0.522	0.500	6260	0.39
SQ-L_{110}-$p_{0.20}$	110	70	12	3	0.20	0.567	0.547	6800	0.43
SQ-L_{110}-$p_{0.26}$	110	51	12	4	0.26	0.536	0.519	6430	0.40
SQ-L_{110}-$p_{0.33}$	110	40	12	5	0.33	0.524	0.504	6290	0.39

Series III: In these experiments, rectangular and streamlined bars were used. The number of bars (n = 3), the bar spacing (b_a = 63 mm), the water level (h_1), the freestream velocity and the Froude number (F), were kept constant. The goal was to study the effects of bar thickness, bar depth and bar shape on head loss coefficient and the velocity field. The test conditions are summarized in Table 4.3. In the first column of the table, the subscript after s denotes the bar thickness in mm, while subscript after L denoted the bar depth in mm. For example, in test SQ-s_6-L_{50}, the trashrack model is comprised of rectangular bars with thickness, s = 6 mm and bar depth, L = 50 mm. The ST-s_{12}-L_{100} denotes streamlined bar.

Table 4.3: Summary of Test Conditions for *Series III*

Test	L (mm)	b_a (mm)	s (mm)	n	p	U_e (m/s)	U_1 (m/s)	Re_s	F
SQ-s_6-L_{50}	50	63	6	3	0.10	0.511	0.487	3070	0.38
SQ-s_9-L_{50}	50	63	9	3	0.15	0.511	0.487	4600	0.38
SQ-s_{12}-L_{50}	50	63	12	3	0.20	0.511	0.487	6130	0.38
SQ-$s_{12}L_{76}$	76	63	12	3	0.20	0.510	0.483	6120	0.38
SQ-s_{12}-L_{100}	100	63	12	3	0.20	0.528	0.493	6330	0.40
ST-s_{12}-L_{100}	100	63	12	3	0.20	0.500	0.471	6000	0.38

4.3. Large-Scale Trashrack Models

4.3.1. The Hydraulics Flume

A schematic view of the hydraulics flume used for the large-scale experiments is shown in Figure 4.5. It consists of a flow conditioning section, test section, supporting framework, carriage, circulating pump and pipes. The settling chamber upstream of the flume is fitted with flow straighteners to ensure minimal disturbance. At the outlet of the settling chamber is an adjustable plate, which can be lowered or raised to provide contraction effects on the flow. The test section was fabricated using transparent glass to facilitate visual observations. The interior dimensions of the test section are 930 mm wide by 715 mm high by 13200 mm long. The pump is coupled via a shaft to a 75 hp, 1770 rpm and 575 V AC 3-phase 60 Hz motor.

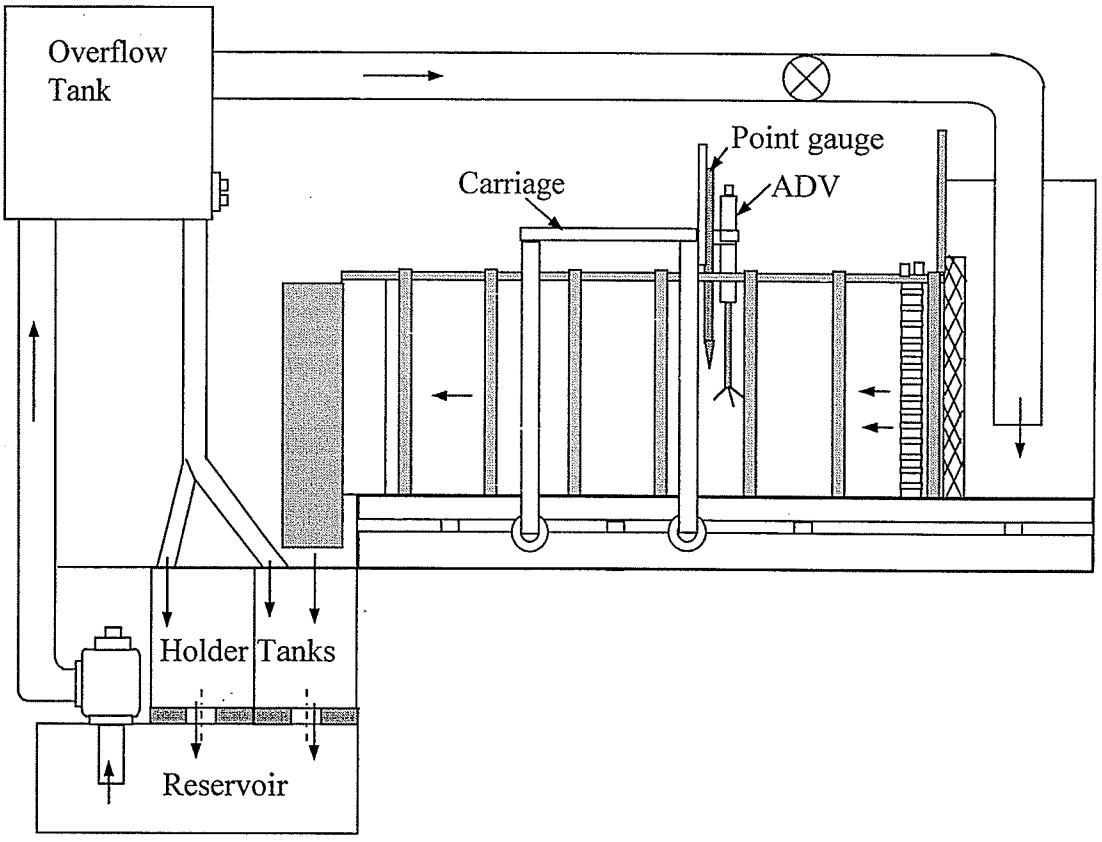

Figure 4.5: Schematic of the hydraulic flume (not to scale).

4.3.2. Inserted Test Section

A provisional test section made from 9 mm thick acrylic plate was inserted into the main channel to hold the array of bars in place. The insert was 1050 mm long, 910 mm wide and 700 mm deep. The base of the inserted test section was screwed onto the floor of the main flume.

4.3.3. Test Models

For the large-scale models, the height and thicknesses of each bar were, respectively, H = 700 mm, and s = 9 mm and 12 mm. The bar depths studied were L = 50 mm and 100 mm. For L = 100 mm, two bar shapes were studied; (i) rectangular cross-section with flat leading and trailing edges and (ii) rectangular cross-section with round leading edge (with a rounding radius of 6 mm) and flat trailing edge. For these cross-sections, the angle of inclination to the approach flow was varied from θ = 0°, 10°, 20°, to 30°. The interspaces studied for the large-scale models were 50 mm, 63 mm, 75 mm, 100 mm, 126 mm and 150 mm. The blockage ratio ranged from p = 0.06 to 0.24.

4.3.4. The ADV System

The flow contained natural particulate matters, which were presumed to follow the fluid flow faithfully. A high resolution, 3D-ADV that has an acoustic frequency of 10 MHz and a standard sampling frequency up to 25 Hz was employed for the flow measurements. The standard settings for the velocity ranges are ±3, ±10, ±30, ±100, and ±250 cm/s. The ADV probe is mounted on a carriage that can be moved along the hydraulic flume when necessary. The ADV can also be moved vertically by a rack and

pinion gear. The ADV measures the flow in a small sampling volume, which is 9 mm long and approximately 6 mm in diameter, and is 50 mm away from the sensing elements. The data were acquired continuously onto 1.80 GHz Pentium 4 computer with 512 MB RAM and two hard drives (203 GB and 29 GB) running on windows XP 2002 using SonTek HorizonADV 1.04 (core 1.04.0.6) software .

4.3.5. Measurement Procedure

The ADV was positioned perpendicular into the flow. The mean velocity measured at $y = 0.6h_1$ was found to be within 6% of the corresponding discharge velocity. The upstream water level was maintained constant at h_1 = 500 mm. Measurements were made at Reynolds number based on the bar thickness and approach velocity that ranges from 5000 $\leq Re_s \leq$ 6780. The Froude number based on upstream water level and approach velocity was $F \approx 0.25$. For each test condition, measurements were obtained for two locations: far upstream of the bars, and far downstream of the bars. For each test condition at a given point, 5000 samples were taken and recorded on the PC. The ADV was operated at a sampling rate of 5 Hz and velocity range of ±100 cm/s. The samples for each measurement point were processed using WinADV32 (version 2.0250), a software developed by SonTek. This permits the extraction of the processed data onto Excel spreadsheet for averaging. Preliminary convergence test indicated that 5000 samples were sufficient to calculate the mean velocity.

The water level measurements were made with a point gauge, which was also attached to the carriage, and is moved vertically by a separate rack and pinion gear. For each test

condition, the water levels (h_1 and h_2) and velocities (U_1 and U_2) were measured at mid-span of the flume.

4.3.6. Summary of Test Conditions

The summary of test conditions for the large scale experiments is provided in Tables 4.4 and 4.5. The large-scale experiments were also conducted in series: *Series 1, Series 2, Series 3, Series 4, Series 5* and *Series 6*.

Series 1: In these experiments, the bar thickness (s = 12 mm), bar depth (L = 100 mm), Reynolds number (Re_s) and Froude number (F) were held constant while bar spacing (b_a) and number of bars (n) were varied from 50 mm to 150 mm and 6 to 18, respectively. The goal was to study the effects of blockage ratio on head loss coefficient. The test conditions are shown in Table 4.4. In the first column of the table, SQ denotes rectangular bar with square leading and trailing edges, the subscript after s denotes the bar thickness in mm while the subscript after L denotes the bar depth in mm. For example, in test SQ-s_{12}-L_{100}, the model is comprised of rectangular bars with bar thickness, s = 12 mm and bar depth, L is 100 mm.

Series 2: These experiments were conducted to specifically study the effects of rounding the bar leading edge and blockage ratio on head loss coefficients. In these experiments, the bar thickness (s = 12 mm), bar depth (L = 100 mm), Reynolds number (Re_s) and Froude number (F) were held constant while bar spacing (b_a) and number of bars (n) were varied from 50 mm to 150 mm and 6 to 18, respectively. The test conditions are

shown in Table 4.4. In the first column of the table, RD denotes rectangular bar with round leading edge but square trailing edge, the subscript after s denotes the bar thickness in mm while the subscript after L denotes the depth of the bar in mm. For example, in test RD-s_{12}-L_{100}, the model is comprised of rectangular bars with round leading edge, bar thickness, s = 12 mm and bar depth, L is 100 mm.

Table 4.4: Summary of test conditions; effects of bar spacing, bar depth, thickness and shape

Bar type	L (mm)	s (mm)	θ^o	b_a (mm)	n	p	U_1 (m/s)	Re	F
Square leading edge (SQ) SQ-s_{12}-L_{100} (*Series 1*)	100	12	0	50	18	0.24	0.543	6516	0.25
	100	12	0	63	14	0.18	0.555	6660	0.25
	100	12	0	75	12	0.16	0.547	6564	0.25
	100	12	0	100	9	0.12	0.546	6552	0.25
	100	12	0	126	7	0.09	0.557	6684	0.25
	100	12	0	150	6	0.08	0.557	6684	0.25
Round leading edge (RD) RD-s_{12}-L_{100} (*Series 2*)	100	12	0	50	18	0.24	0.560	6720	0.25
	100	12	0	63	14	0.18	0.558	6696	0.25
	100	12	0	75	12	0.16	0.560	6720	0.25
	100	12	0	100	9	0.12	0.557	6684	0.25
	100	12	0	126	7	0.09	0.563	6756	0.25
	100	12	0	150	6	0.08	0.565	6780	0.26
Square leading edge (SQ) SQ-s_{12}-L_{50} (*Series 3*)	50	12	0	50	18	0.24	0.545	6540	0.25
	50	12	0	63	14	0.18	0.548	6576	0.25
	50	12	0	75	12	0.16	0.553	6636	0.25
	50	12	0	100	9	0.12	0.551	6612	0.25
	50	12	0	126	7	0.09	0.561	6732	0.25
	50	12	0	150	6	0.08	0.561	6732	0.25
Square leading edge (SQ) SQ-s_9-L_{50} (*Series 4*)	50	9	0	50	18	0.18	0.548	4932	0.25
	50	9	0	63	14	0.14	0.558	5022	0.25
	50	9	0	75	12	0.12	0.558	5022	0.25
	50	9	0	100	9	0.09	0.563	5067	0.25
	50	9	0	126	7	0.07	0.567	5103	0.26
	50	9	0	150	6	0.06	0.567	5103	0.26

Series 3: In these experiments, the bar thickness (s = 12 mm), bar depth (L = 50 mm), Reynolds number (Re_s) and Froude number (F) were held constant while bar spacing (b_a) and number of bars (n) were varied from 50 mm to 150 mm and 6 to 18, respectively. The goal was to study the effects of bar depth by comparing it to *Series 1* (SQ-s_{12}-L_{100}), along with blockage ratio on head loss coefficient. The test conditions are shown in Table 4.4. In the first column of the table, SQ denotes rectangular bar with square leading and trailing edges, the subscript after s denotes the bar thickness in mm while the subscript after L denotes the depth of the bar in mm. For example, in test SQ-s_{12}-L_{50}, the model is comprised of rectangular bars with bar thickness, s = 12 mm and bar depth, L is 50 mm.

Series 4: In these experiments, the bar thickness (s = 9 mm), bar depth (L = 50 mm), Reynolds number (Re_s) and Froude number (F) were held constant while bar spacing (b_a) and number of bars (n) were varied from 50 mm to 150 mm and 6 to 18, respectively. The goal was to study the effects of bar thickness by comparing it to *Series 3* (SQ-s_{12}-L_{50}), along with blockage ratio on head loss coefficient. The test conditions are shown in Table 4.4. In the first column of the table, SQ denotes rectangular bar with square leading and trailing edges, the subscript after s denotes the bar thickness in mm while the subscript after L denotes the depth of the bar in mm. For example, in test SQ-s_9-L_{50}, the model is comprised of rectangular bars with bar thickness, s = 9 mm and bar depth, L is 50 mm.

Series 5: In these experiments, the bar thickness (s = 12 mm), bar depth (L = 100 mm), Reynolds number (Re_s) and Froude number (F) were held constant while bar spacing (b_a = 50 mm, 75 mm and 100 mm), bar inclination (θ = 0°, 10°, 20° and 30°) and number of

bars (n = 9, 12 and 18) were varied. The goal was to study the effects of bar inclination and blockage ratio on head loss coefficient. The test conditions are shown in Table 4.5. In the first column of the table, SQ denotes rectangular bar with square leading and trailing edges, the subscript after s denotes the bar thickness in mm while the subscript after L denotes the depth of the bar in mm. For example, in test SQ-s_{12}-L_{100}, the model is comprised of rectangular bars with bar thickness, s = 12 mm and bar depth, L is 100 mm.

Series 6: These experiments were conducted to specifically study the effects of bar inclination, rounding the bar leading edge and blockage ratio on head loss coefficients. In these experiments, the bar thickness (s = 12 mm), bar depth (L = 100 mm), Reynolds number (Re_s) and Froude number (F) were held constant while bar spacing (b_a = 50 mm, 75 mm and 100 mm), bar inclination (θ = 0°, 10°, 20° and 30°) and number of bars (n = 9, 12 and 18) were varied. The test conditions are shown in Table 4.5. In the first column of the table, RD denotes rectangular bar with round leading edge but square trailing edge, the subscript after s denotes the bar thickness in mm while the subscript after L denotes the depth of the bar in mm. For example, in test RD-s_{12}-L_{100}, the model is comprised of rectangular bars with round leading edge, bar thickness, s = 12 mm and bar depth, L is 100 mm.

Table 4.5: Summary of test conditions; effects of bar inclination and bar spacing

Bar	L (mm)	s (mm)	b_a (mm)	$\theta°$	n	p	U_1 (m/s)	Re	F
Square leading edge (SQ)	100	12	50	0	18	0.24	0.543	6516	0.25
	100	12	50	10	18	0.24	0.495	5940	0.22
	100	12	50	20	18	0.24	0.491	5892	0.22
SQ-s_{12}-L_{100}	100	12	50	30	18	0.24	0.477	5724	0.22
(*Series 5*)	100	12	75	0	12	0.16	0.547	6564	0.25
	100	12	75	10	12	0.16	0.499	5988	0.23
	100	12	75	20	12	0.16	0.501	6012	0.23
	100	12	75	30	12	0.16	0.488	5856	0.22
	100	12	100	0	9	0.12	0.546	6552	0.25
	100	12	100	10	9	0.12	0.501	6012	0.23
	100	12	100	20	9	0.12	0.500	6000	0.23
	100	12	100	30	9	0.12	0.495	5940	0.22
Round leading edge (RD)	100	12	50	0	18	0.24	0.560	6720	0.25
	100	12	50	10	18	0.24	0.493	5916	0.22
	100	12	50	20	18	0.24	0.488	5856	0.22
RD-s_{12}-L_{100}	100	12	50	30	18	0.24	0.485	5820	0.22
	100	12	75	0	12	0.16	0.560	6720	0.25
(*Series 6*)	100	12	75	10	12	0.16	0.502	6024	0.23
	100	12	75	20	12	0.16	0.499	5988	0.23
	100	12	75	30	12	0.16	0.491	5892	0.22
	100	12	100	0	9	0.12	0.557	6684	0.25
	100	12	100	10	9	0.12	0.501	6012	0.23
	100	12	100	20	9	0.12	0.498	5976	0.23
	100	12	100	30	9	0.12	0.496	5952	0.22

CHAPTER 5: RESULTS AND DISCUSSION

5.1. Introduction

This chapter presents and discusses the results obtained from the small-scale and large-scale experiments. The chapter begins with the results for small-scale trashrack models in section 5.2. In this section, the characteristics of approach flow and the flow far downstream of the trashrack bars are quantified using profiles in the x-y plane. The variation of dip with the various trashrack models is also reported. The section also reports iso-contours obtained near the various trashrack models as well as profiles of mean velocities and turbulent quantities. Section 5.3 presents head loss coefficients for the small-scale and large-scale models, using correlations reported in Chapter 2. Section 5.4 discusses the implications of the flow field near a trashrack on the trashrack bars, head loss and fish response.

5.2. Small-Scale

5.2.1 Flow Qualification

Boundary Layer Characterization: Prior to conducting measurements across the bars (in x-z plane), data were taken in x-y plane located at channel mid-plane (z = 0) to characterize the velocity distribution across flow depth at upstream (x/s = -15) and downstream (x/s = 20) of the bars. Figure 5.1 shows that, for $\theta_0 U_{0.52}$, values of U at the upstream location are uniform across the outer 88% of the flow depth but the downstream values decrease below the maximum value close to the free surface. The background turbulence level close to the free surface (not shown) was $u/U_e = 0.06$.

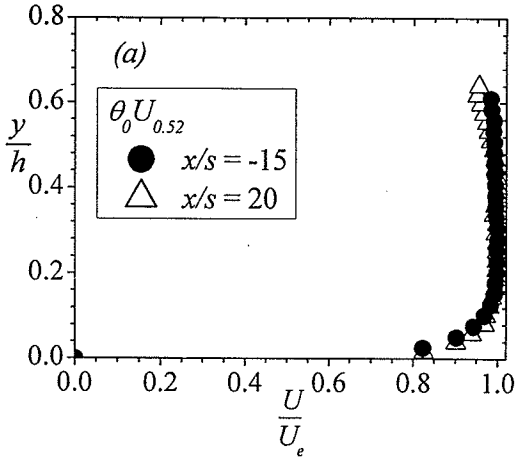

Figure 5.1: Mean streamwise velocity profiles upstream (x/s = -15) and downstream (x/s = 20) of bars

Variation of Dip with Approach Flow, Bar Inclination, Bar Spacing and Bar Geometry: The dip of the free surface (d), relative to the undisturbed free surface upstream of the bars, are plotted in Figures 5.2a, 5.2b and 5.2c, respectively, for *Series I*, *Series II* and *Series III*. The figures show that the water level rose above the upstream reference value in the vicinity of the bar leading edge. Figure 5.2a shows the variation of the dip with bar inclination and approach velocity. For $\theta_0 U_{0.26}$, there is only a minimal depression within and downstream of the bars. As the Reynolds number increased ($\theta_0 U_{0.52}$, $\theta_0 U_{0.76}$), the free surface downstream of the aligned bars became severely distorted and the dip increased. Figure 5.2a shows that the maximum depression (d_{max}), the corresponding x-location of d_{max} (x_{max}) and the x-location where d tends to level off also increased with Reynolds number. At a similar U_e value (or Reynolds number), d increased substantially with θ. It is also evident from Figures 5.2b and 5.2c that the dip of the free surface within and downstream of the bars increases with blockage ratio, bar depth and bar thickness. The increase with bar depth is however, marginal. The dip is smallest for SQ-s_6-L_{50} and ST-s_{12}-L_{100} (Figure 5.2c).

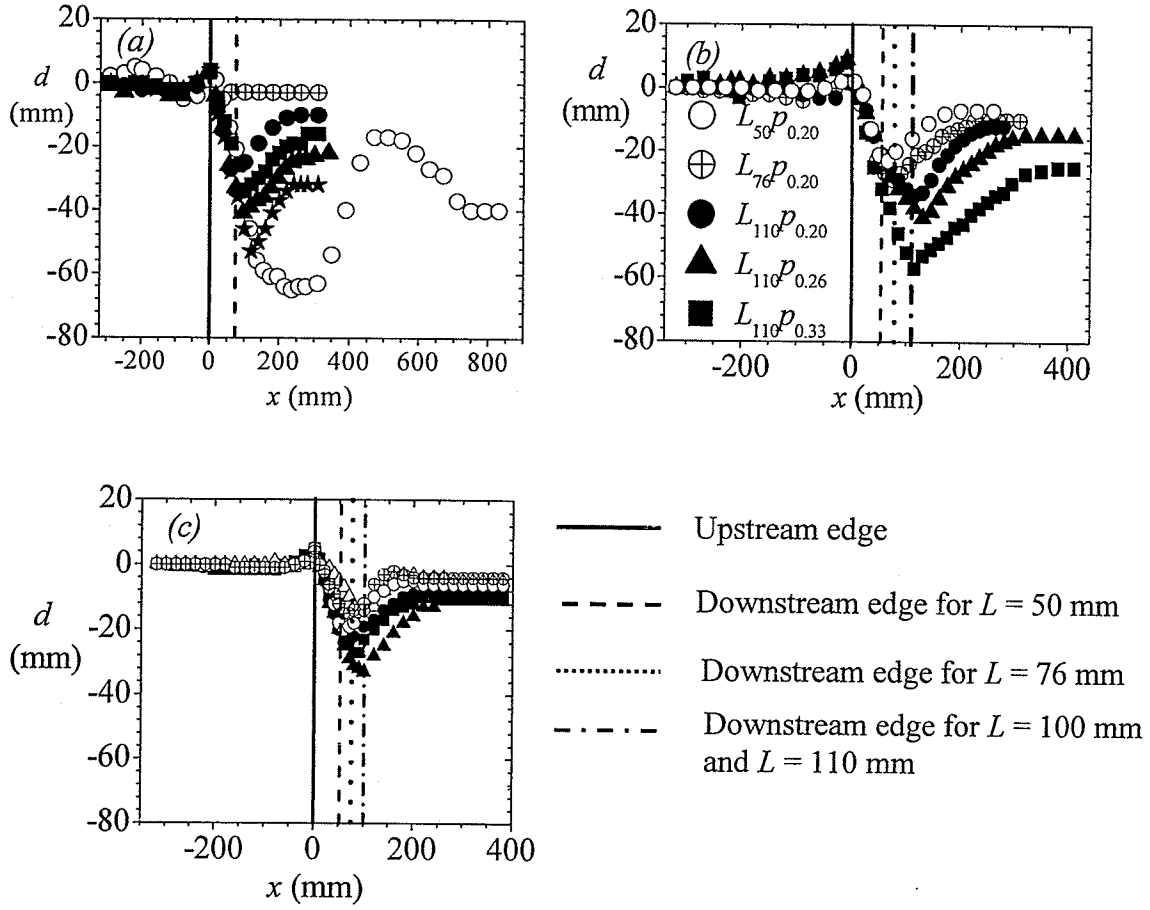

Figure 5.2: Variation of dip with; (*a*): velocity and bar inclination; ($\theta_0U_{0.26}$: ⊕; $\theta_0U_{0.52}$: ●; $\theta_0U_{0.76}$: ○; $\theta_6U_{0.52}$: ■; $\theta_9U_{0.52}$: ▲; $\theta_{12}U_{0.52}$: ★); (*b*): bar depth and blockage ratio: (SQ-L_{50}-$p_{0.20}$: ○; SQ-L_{76}-$p_{0.20}$: ⊕; SQ-L_{110}-$p_{0.20}$: ●; SQ-L_{110}-$p_{0.26}$: ▲; SQ-L_{110}-$p_{0.33}$: ■); (*c*): bar thickness, depth and bar shape: (SQ-s_6-L_{50}: ⊕; SQ-s_9-L_{50}: ○; SQ-s_{12}-L_{50}: ●; SQ-s_{12}-L_{76}: ■; SQ-s_{12}-L_{100}: ▲; ST-s_{12}-L_{100}: △)

5.2.2. Iso-contours

In this section iso-contours of mean velocity, Reynolds shear stress, turbulent kinetic energy and mean vorticity are presented. In each case, the streamlines are superimposed on the contours to facilitate their discussion in terms of the mean flow pattern. It should be noted that the topmost bars in Figures 5.3 to 5.12 are the bars closer to the channel wall (see Figure 4.3). For all test cases, the flow separated near the forward corners of the

bars. However, the shear layer and vortex formation depend strongly on bar inclination, bar depth, bar thickness, blockage ratio and bar shape.

5.2.2.1. Iso-contours of Mean Velocity

Figure 5.3 shows iso-contours of U/U_e, for the case where the bars were inclined ($\theta = 0°$, 6°, 9° and 12°) to the approach flow (*Series I*). There are distinct effects of bar inclination on the flow patterns. Close to the leading edge of the aligned bars (Figure 5.3a), for example, shallow recirculation bubbles are formed on either side of the bars and both the size and strength of the vortices are similar. As the bar inclination increased, the recirculation bubble on the leeward side of the bars increased while that formed at the windward side became less distinct and eventually disappeared. Bar inclination produced a skewed or asymmetric mean flow pattern, and significantly increased $(U/U_e)_{max}$ between the bars. The regions of $(U/U_e)_{max}$ within the bars are adjacent to the recirculation bubble (which are found in the leeward side of the inclined bars). A pair of well-defined symmetrical counter-rotating vortices are formed downstream of the aligned bars (Figure 5.3a). Downstream of the inclined bars, on the other hand, the recirculation bubbles are less distinct and asymmetric. As the flow evolved past the inclined bars, two distinct wake or low-velocity regions interconnected by a relatively higher velocity region are formed at the downstream of the bars. The two shear layers developed progressively and distinctly apart with increasing downstream distance.

Figures 5.4 and 5.5 show that the streamlines in-between the bars are nearly parallel to each other and the bars, except in the immediate vicinity of the bars where recirculation

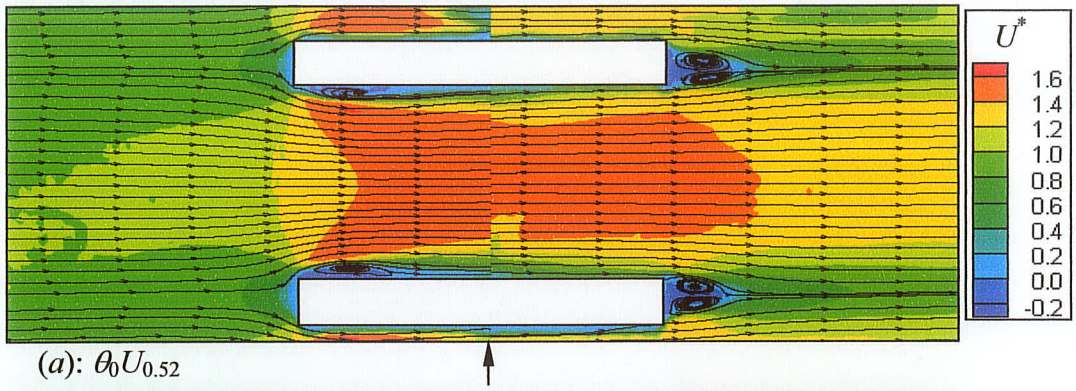

(*a*): $\theta_0 U_{0.52}$

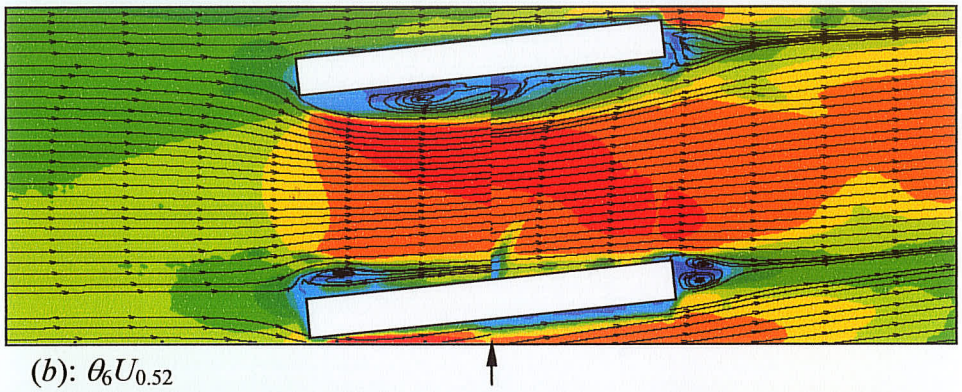

(*b*): $\theta_6 U_{0.52}$

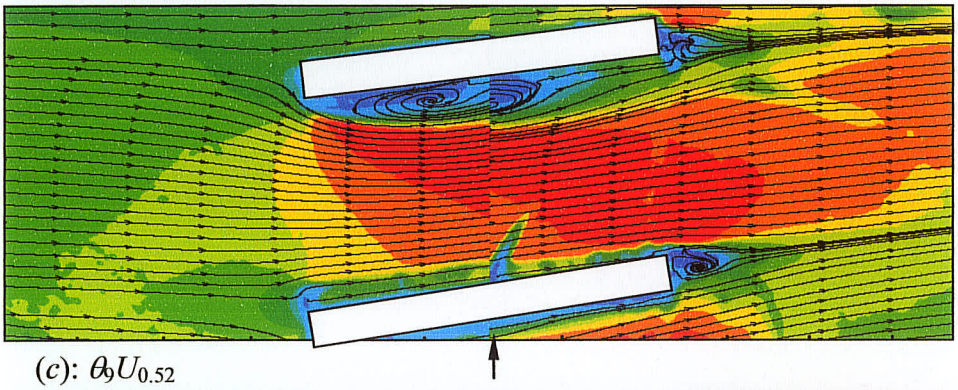

(*c*): $\theta_9 U_{0.52}$

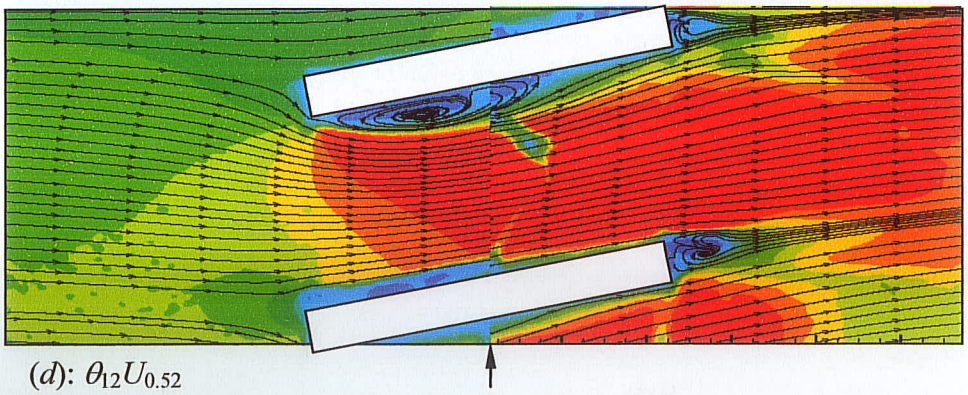

(*d*): $\theta_{12} U_{0.52}$

Figure 5.3: Iso-contours of mean velocity ($U^* = U/U_e$) to study the effects of bar inclination on mean flow pattern. Arrows indicate position where two planes merge.

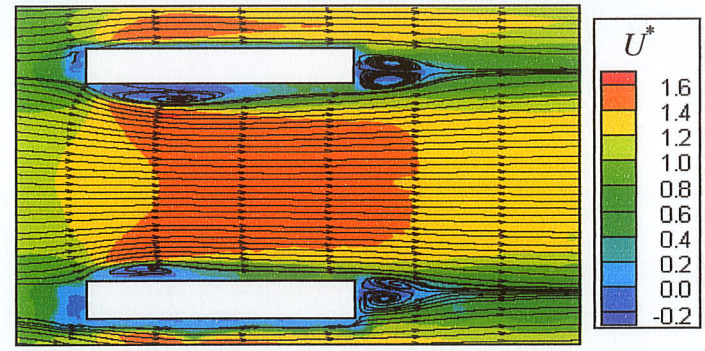

(*a*): SQ-L_{50}-$p_{0.20}$

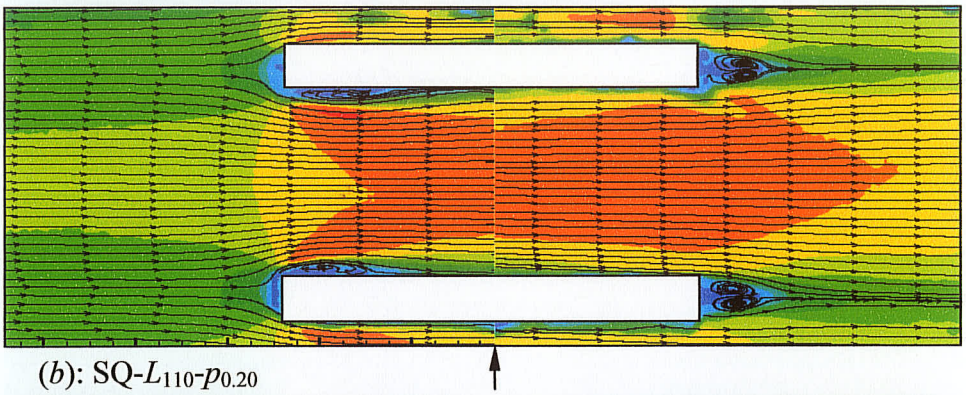

(*b*): SQ-L_{110}-$p_{0.20}$

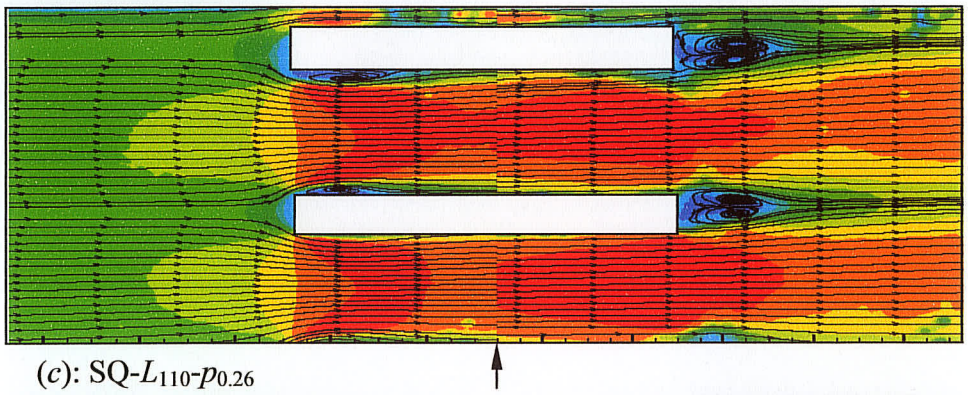

(*c*): SQ-L_{110}-$p_{0.26}$

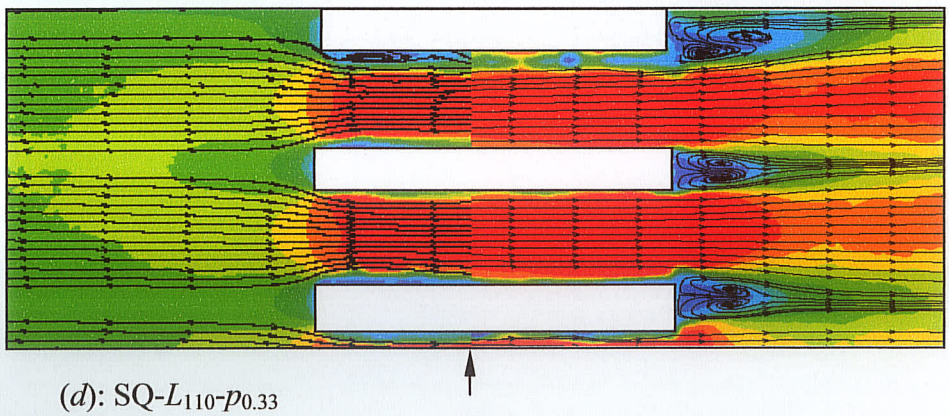

(*d*): SQ-L_{110}-$p_{0.33}$

Figure 5.4: Iso-contours of mean velocity ($U^* = U/U_e$) to study the effects of bar depth and blockage ratio on mean flow pattern. Arrows indicate position where two planes merge.

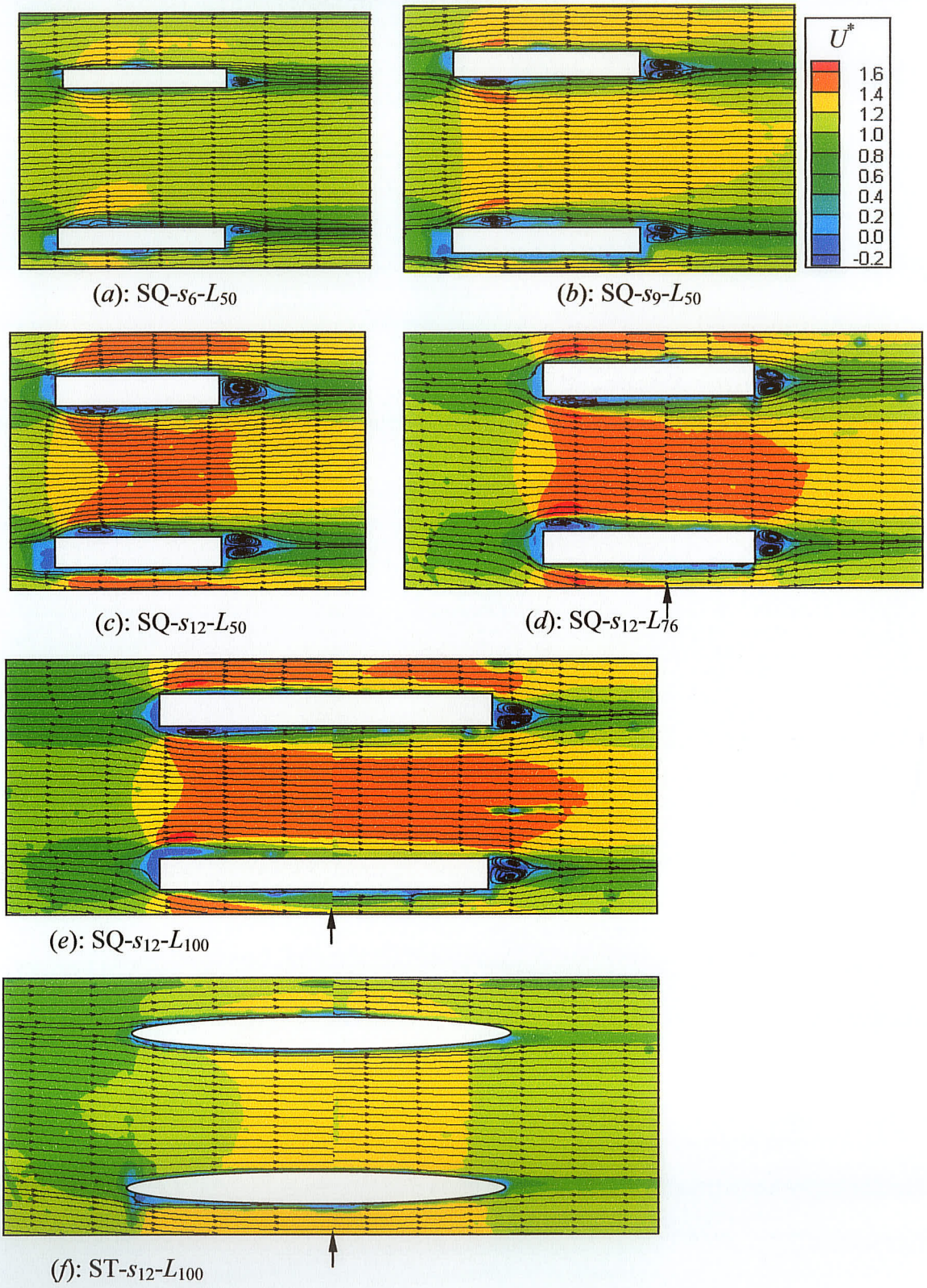

Figure 5.5: Iso-contours of mean velocity ($U^* = U/U_e$) to study the effects of bar thickness, bar depth and bar shape on mean flow pattern. Arrows indicate position where two planes merge.

zones are formed. Close to the leading edge, the size of the recirculation zones below the bars decrease with increasing blockage ratio (Figures 5.4b to 5.4d) and also with increasing *L/s* (Figures 5.4a and 5.4b). Because of the reduction in the flow area by the bars, the mean velocity within the bars is higher than that observed upstream of the bars. The diminishing of the recirculation zone as the blockage ratio increases is a consequence of enhanced flow acceleration within the bars. The increased section blockage and drop in water level (Figure 5.2b) contribute immensely to the higher velocity within the bars and the increased head losses for SQ-L_{110}-$p_{0.26}$ and SQ-L_{110}-$p_{0.33}$. It should be noted that, with increasing blockage ratio, the shear layers produced along the bars become thinner and more intense. Meusburger *et al.* [14], in their DNS simulation, reported that the increased flow velocity coupled with reduced vortex thickness as blockage ratio increases form an intense shear zone along the bars which in turn produce the major part of the head losses. The size of the pair of well-defined symmetrical counter-rotating vortices that is formed at the downstream of the bars of Figure 5.4 decreases with increasing *L/s*. The vortices, however, increase in size with increasing blockage ratio. The offset of the center of the clockwise-rotating recirculation bubble at the trailing edge of the bar of SQ-L_{110}-$p_{0.33}$, close to the channel wall relative to the centre of other recirculation bubbles, was due to the nearness of that bar to the channel wall.

It is also evident from Figure 5.5 that the size of the recirculation zones and the magnitude of the mean velocity within the bars diminish with decreasing bar thickness (Figures 5.5a, 5.5b and 5.5c). Note that as the bar thickness decreases, the blockage ratio also decreases. On the other hand, no distinct recirculation bubbles are observed along

and at the trailing edge of the streamlined bars (Figures 5.5f). Further, the mean velocity within the streamlined bars (Figure 5.5f) is lower than that observed for the corresponding rectangular bars (Figure 5.5e). The minimal drop in water level coupled with the increased net flow area within the streamlined bars (Figure 5.5f) as opposed to rectangular bars (SQ-s_{12}-L_{100}), accounts for the marked low velocity within the streamlined bars. It should be noted that the wakes of the streamlined bars are relatively thinner than that for the rectangular bars. Similarly, the shear layer along the streamlined bars is relatively thinner than that for the rectangular bars. The formation of thinner shear layer along the streamlined bars may be due to the absence of leading edge separation bubbles.

5.2.2.2. Iso-contours of Turbulent Quantities

The iso-contours of the dimensionless Reynolds shear stress ($-uw/U_e^2$) and turbulent kinetic energy (k/U_e^2) corresponding to Figures 5.3, 5.4 and 5.5 are, respectively, shown in Figures 5.6 and 5.7, 5.8, and 5.9. The signs of the Reynolds shear stress (Figures 5.6) on opposite sides of the wake axes are different in accordance to the orientation of the shear layer. The turbulent kinetic energy, as shown in Figure 5.7, was approximated from $k = 0.5(u^2 + w^2)$. In general, the plots reveal regions of extremely high turbulence levels around the outer edge of the recirculation bubbles formed close to the bar leading edge and also within the downstream wake region. It is apparent that bar inclination increased the turbulence level substantially (Figures 5.6 and 5.7). The turbulence levels are typically higher downstream of the bars than between the bars. The two distinct low-velocity regions observed downstream of the inclined bars are replaced by distinct high-turbulence regions in Figures 5.6 and 5.7.

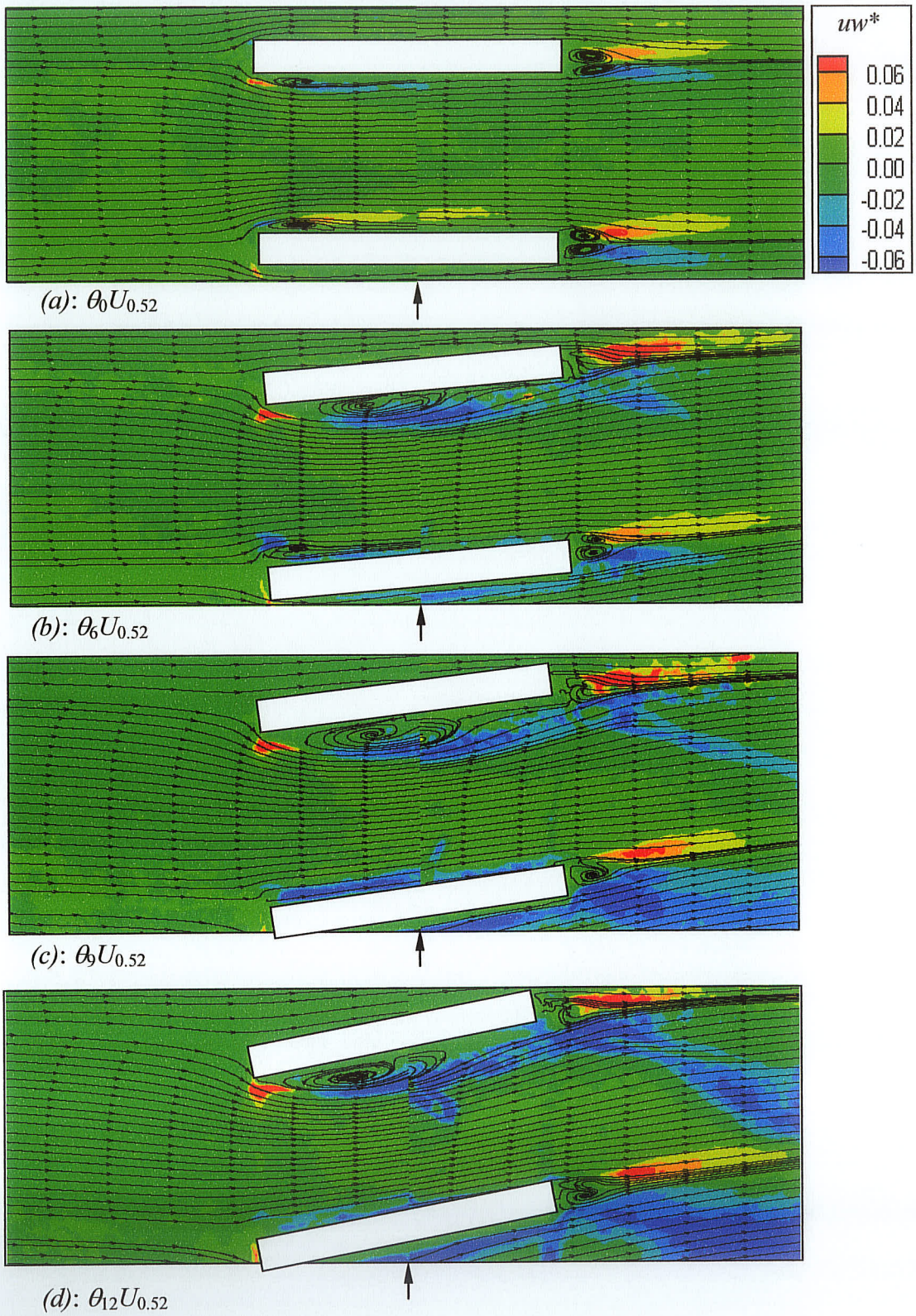

Figure 5.6: Iso-contours of Reynolds shear stress ($uw^* = -uw/U_e^2$) to study the effects of bar inclination on mean flow pattern. Arrows indicate position where two planes merge.

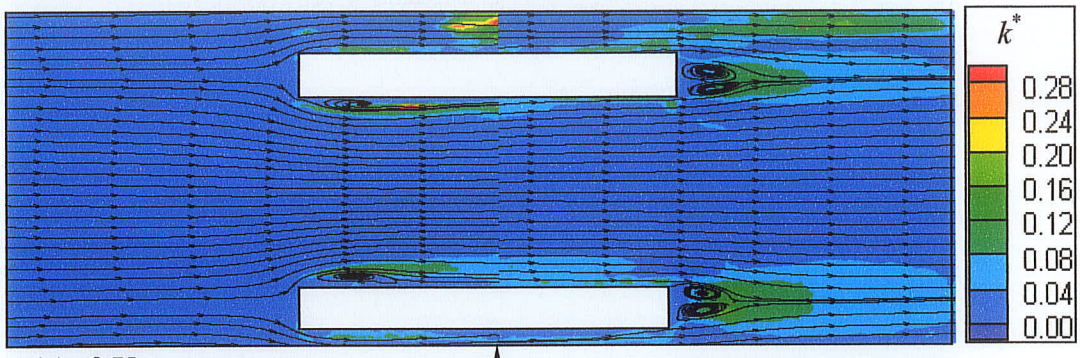

(a): $\theta_0 U_{0.52}$

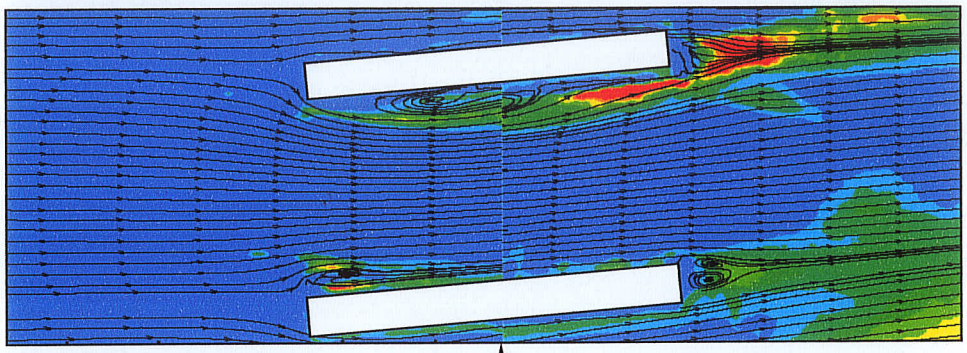

(b): $\theta_6 U_{0.52}$

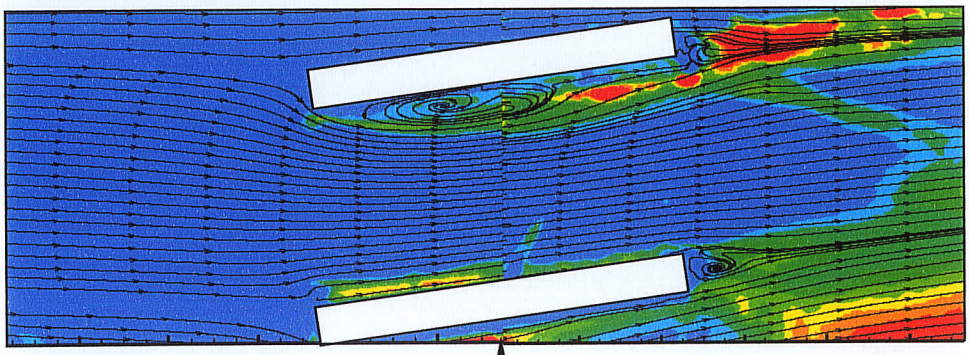

(c): $\theta_9 U_{0.52}$

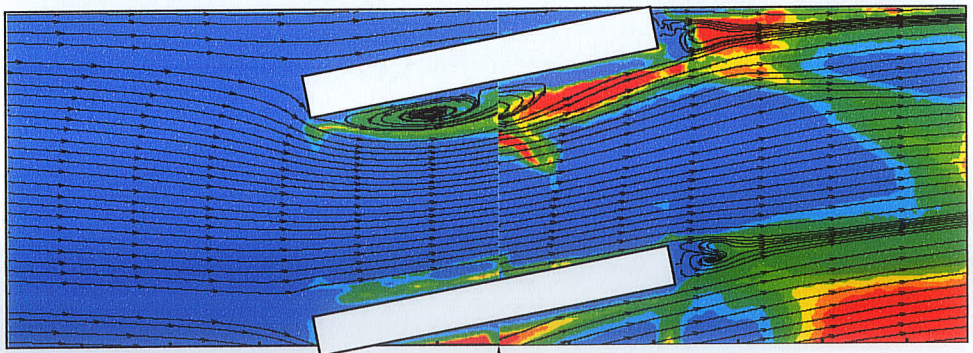

(d): $\theta_{12} U_{0.52}$

Figure 5.7: Iso-contours of turbulent kinetic energy ($k^* = k/U_e^2$) to study the effects of bar inclination on mean flow pattern. Arrows indicate position where two planes merge.

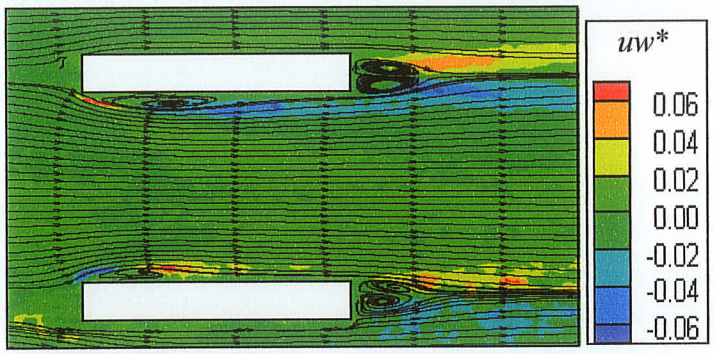

(a): SQ-L_{50}-$p_{0.20}$

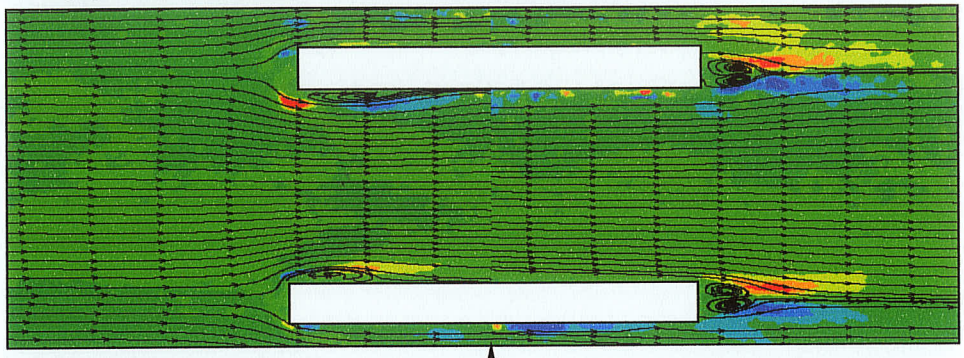

(b): SQ-L_{110}-$p_{0.20}$

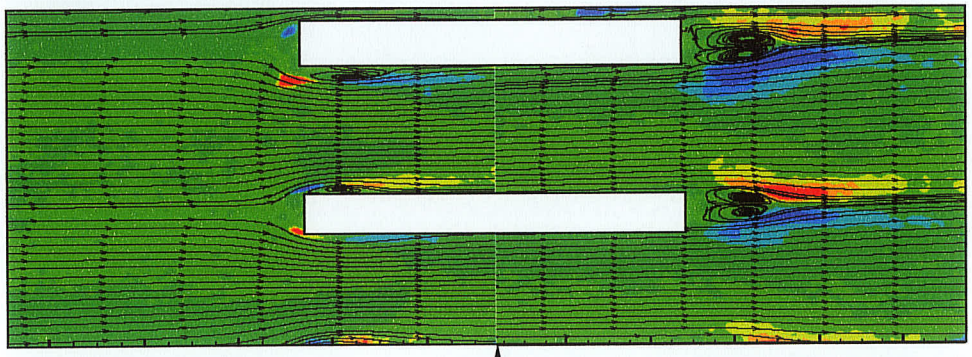

(c): SQ-L_{110}-$p_{0.26}$

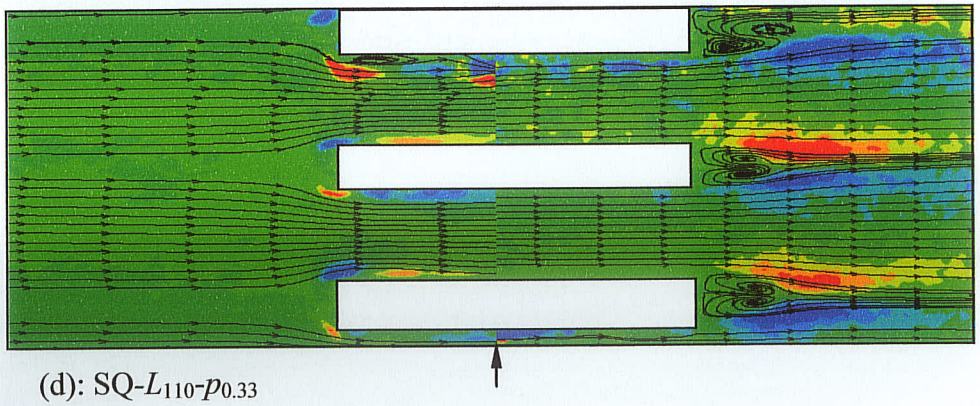

(d): SQ-L_{110}-$p_{0.33}$

Figure 5.8: Iso-contours of Reynolds shear stress ($uw^* = -uw/U_e^2$) to study the effects of bar depth and blockage ratio on mean flow pattern. Arrows indicate position where two planes merge.

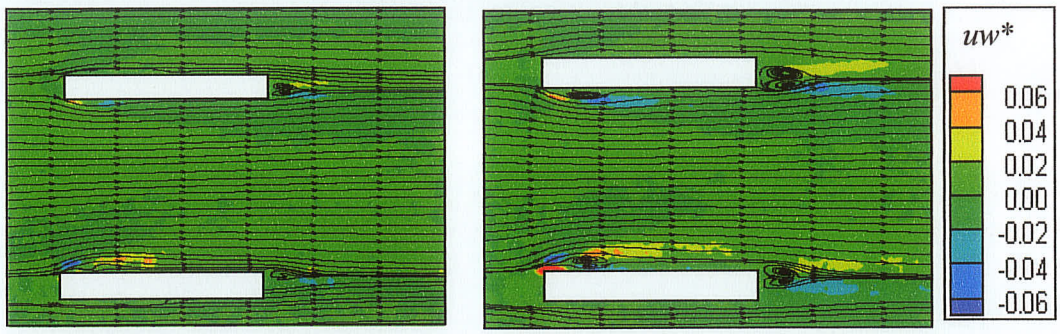

(*a*): SQ-s_6-L_{50} (*b*): SQ-s_9-L_{50}

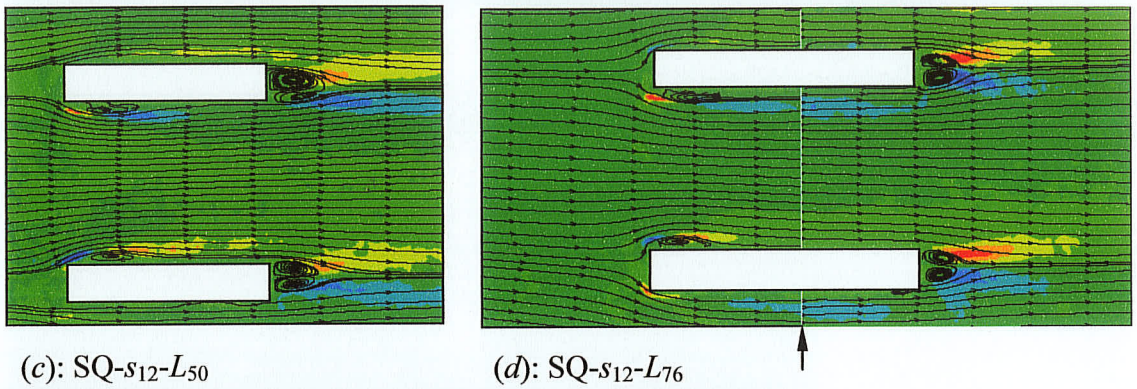

(*c*): SQ-s_{12}-L_{50} (*d*): SQ-s_{12}-L_{76}

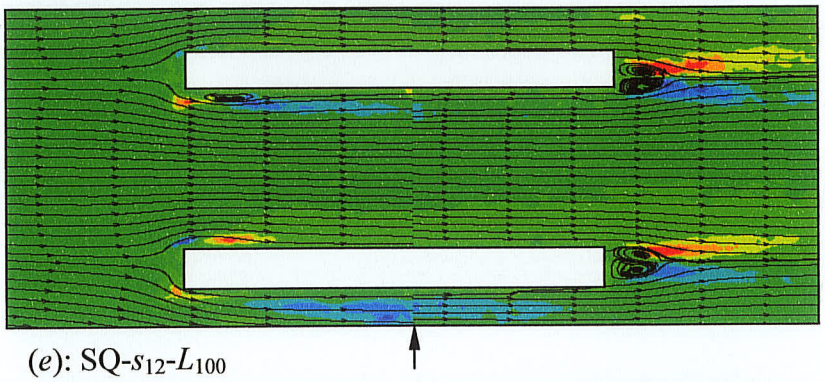

(*e*): SQ-s_{12}-L_{100}

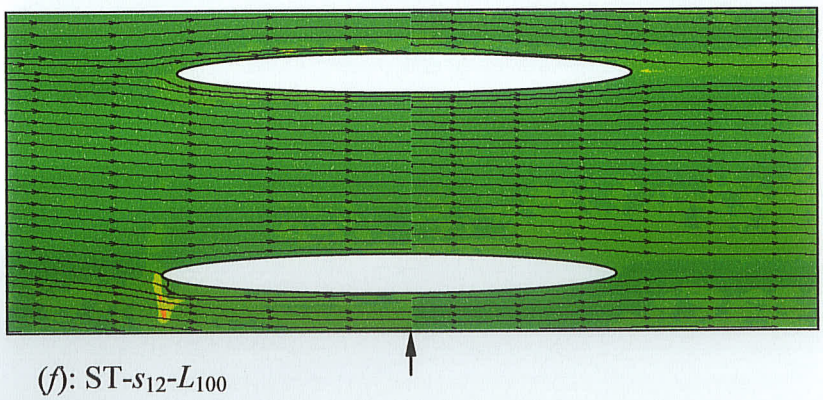

(*f*): ST-s_{12}-L_{100}

Figure 5.9: Iso-contours of Reynolds shear stress ($uw^* = -uw/U_e^2$) to study the effects of bar thickness, bar depth and bar shape on mean flow pattern.

As shown in Figures 5.8 and 5.9 the magnitude of the values of the Reynolds shear stress are the same for different bar depths of the same thickness (Figures 5.8a and 5.8b, and Figures 5.9c, 5.9d and 5.9e). The values increase substantially with increasing blockage ratio (Figure 5.8b to 5.8d). The distinct low-velocity regions observed downstream of the bars (Figures 5.4 and 5.5) are replaced by distinct high-turbulence regions in Figures 5.8 and 5.9. On the other hand, the magnitude of the values of the Reynolds shear stress decreases substantially with decreasing bar thickness (Figures 5.9a, 5.9b and 5.9c) and for the streamlined bars (Figure 5.9f). Similarly, the level of the turbulent kinetic energy (not shown) increased with blockage ratio, but no clear dependence on bar depth was observed. It is also lower for bars with smaller thicknesses and for streamlined bars.

5.2.2.3. Iso-contours of Mean Vorticity

Figures 5.10, 5.11 and 5.12 show the corresponding iso-contours of dimensionless mean vorticity ($\Omega/(U_e/s)$). The mean vorticity was approximated from, $\Omega = \partial W/\partial x - \partial U/\partial z$. The vorticity field can be used to provide insight into regions of strong shear layer or steep velocity gradient. It should be noted that the vorticity is predominantly negative above the bars and positive below the bars in accordance with the orientation of the shear layer. In Figure 5.10, the magnitude of the vorticity tends to increase with increasing inclination. Figures 5.11 and 5.12 shows that the mean vorticity for models consisting of rectangular bars of the same thickness is nearly independent of bar depth. The magnitude however, increases with increasing blockage ratio (Figure 5.11b to 5.11d). This increase in magnitude of vorticity associated with increasing blockage ratio contributes significantly to the formation of intense shearing zones along the bars. The formation of

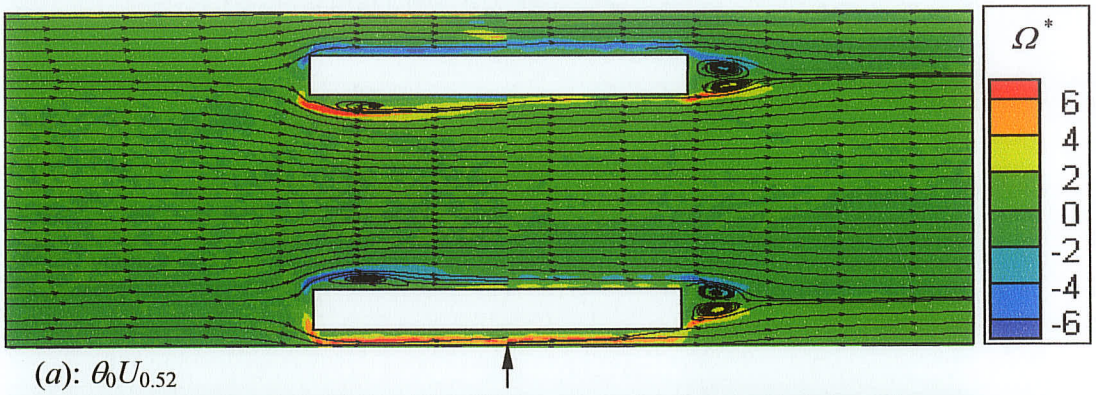

(*a*): $\theta_0 U_{0.52}$

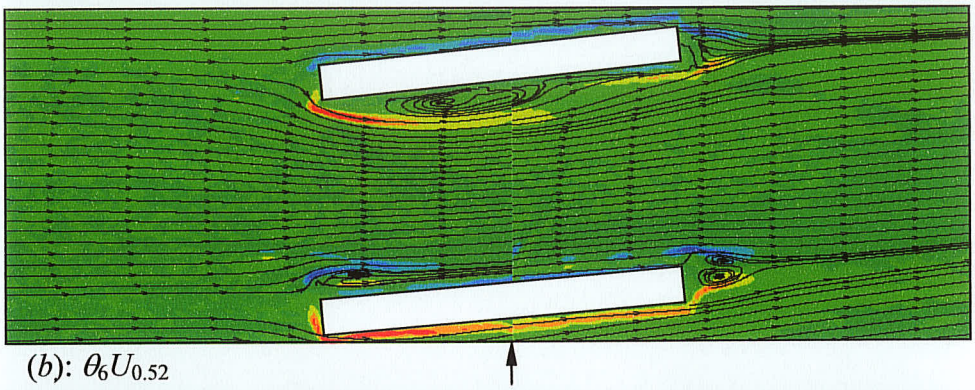

(*b*): $\theta_6 U_{0.52}$

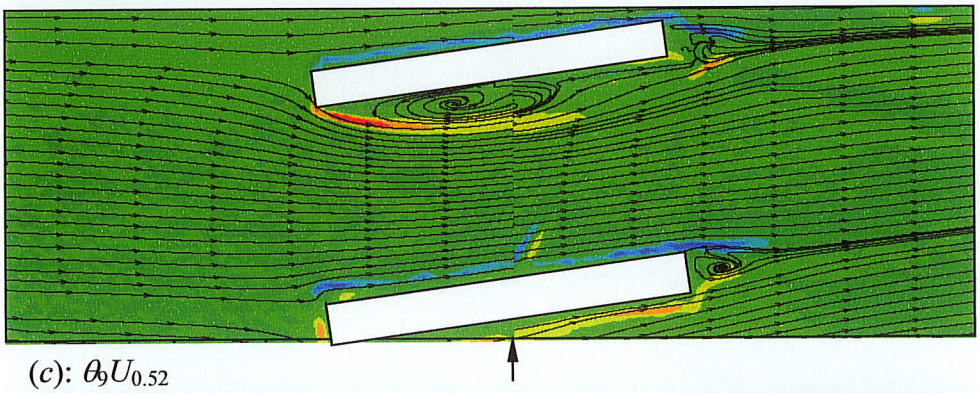

(*c*): $\theta_9 U_{0.52}$

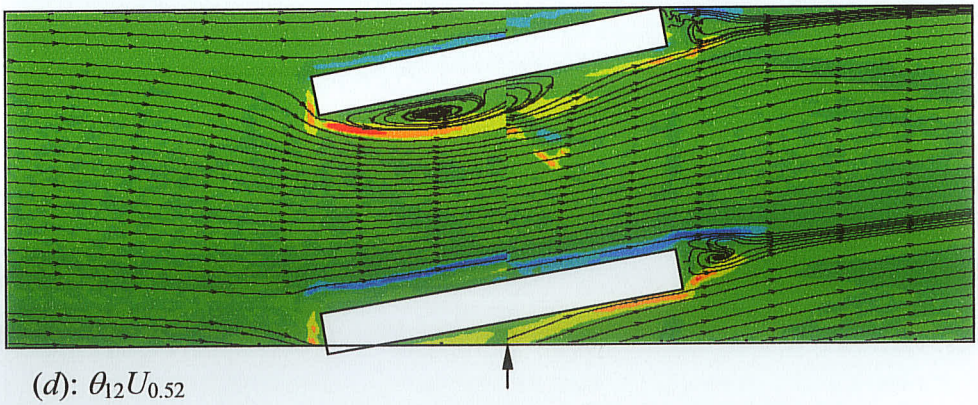

(*d*): $\theta_{12} U_{0.52}$

Figure 5.10: Iso-contours of Mean Vorticity ($\Omega^* = \Omega/(U_e/s)$) to study the effects of bar inclination on mean flow pattern. Arrows indicate position where two planes merge.

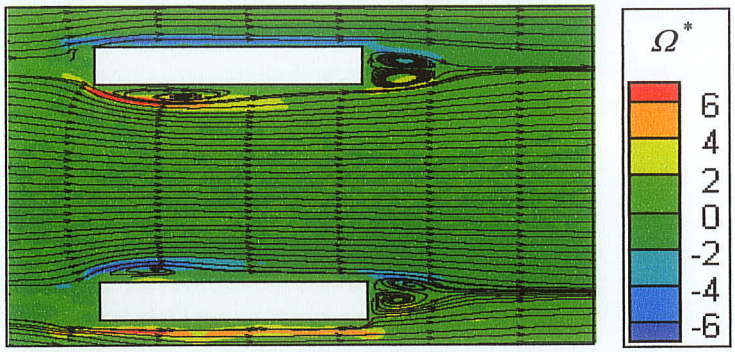

(a): SQ-L_{50}-$p_{0.20}$

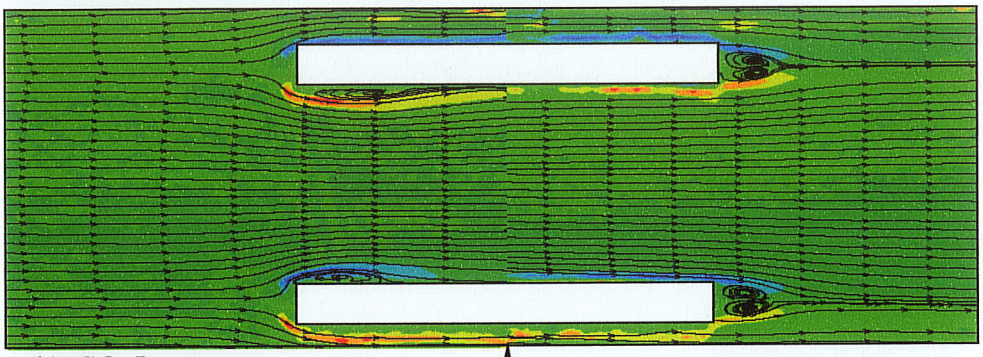

(b): SQ-L_{110}-$p_{0.20}$

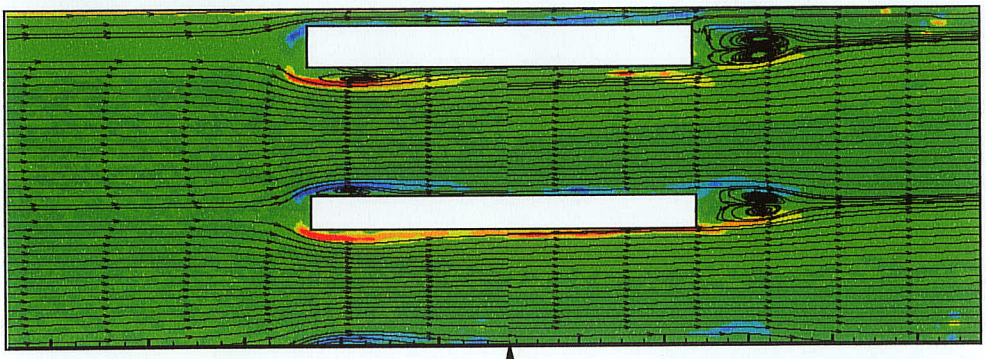

(c): SQ-L_{110}-$p_{0.26}$

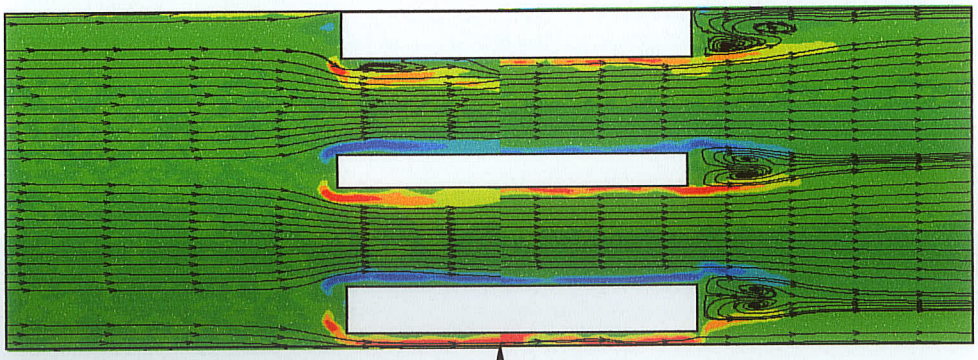

(d): SQ-L_{110}-$p_{0.33}$

Figure 5.11: Iso-contours of Mean Vorticity ($\Omega^* = \Omega/(U_e/s)$) to study the effects of bar depth and blockage ratio on mean flow pattern. Arrows indicate position where two planes merge.

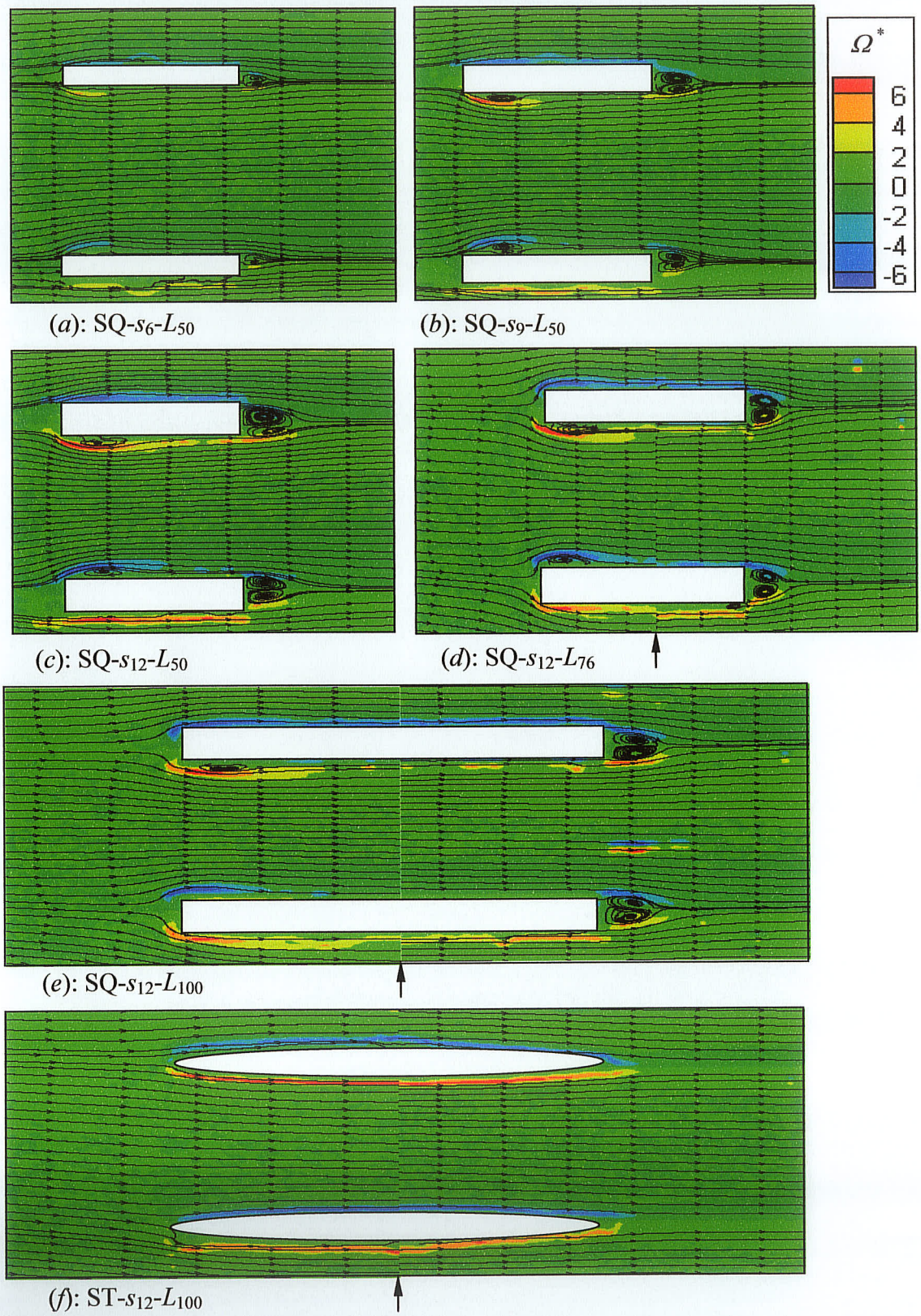

Figure 5.12: Iso-contours of Mean Vorticity($\Omega^* = \Omega/(U_e/s)$) to study the effects of bar thickness, bar depth and bar shape on mean flow pattern. Arrows indicate position where two planes merge.

vorticity along bars is also dependent on the bar thickness and bar form. The magnitude of the mean vorticity decreases with decreasing bar thickness (Figures 5.12a, 5.12b and 5.12c). An evenly distribution of vorticity is also evident around the streamlined bars (Figures 5.12f) with a higher intensity than for the corresponding rectangular bars (Figures 5.12e).

5.2.3. Profiles of Mean Velocities and Turbulence Intensities along the Wake Axes

In this and the following sections, profiles of the mean velocities and turbulent quantities are plotted to quantify some of the observations made earlier. The distributions of the mean velocities and turbulent quantities along the wake axis of the middle bar for *Series I* are shown in Figure 5.13. Upstream of the bars ($x/s < 0$), the mean velocities and turbulent intensities are nearly independent of Reynolds number and bar inclination (except for the very sharp increase observed in W in the immediate vicinity of the inclined bars). As expected, U attained negative values in the recirculation region behind the bars. The values of $(U/U_e)_{min}$ are in the range -0.14 to -0.28. The recirculation bubble length, defined as the distance between the trailing edge of the bar and the downstream location where $U/U_e = 0$ (Figure 5.13a), are x_r/s = 1.60, 1.14 and 1.22, respectively, for $\delta_0 U_{0.26}$, $\delta_0 U_{0.52}$ and $\delta_0 U_{0.76}$. The corresponding values for $\delta_6 U_{0.52}$, $\delta_9 U_{0.52}$, and $\delta_{12} U_{0.52}$ are, respectively, x_r/s = 1.10, 0.95 and 0.96. These results show that the recirculation bubble length does not change significantly with bar inclination. It should be noted that U_{max}/U_e exceeded unity for some of the test conditions because the depression of the water levels immediately downstream of the bars increased the mean velocity. In accordance with the data plotted in Figure 5.2a, U_{max}/U_e increased with Reynolds number for the aligned bars

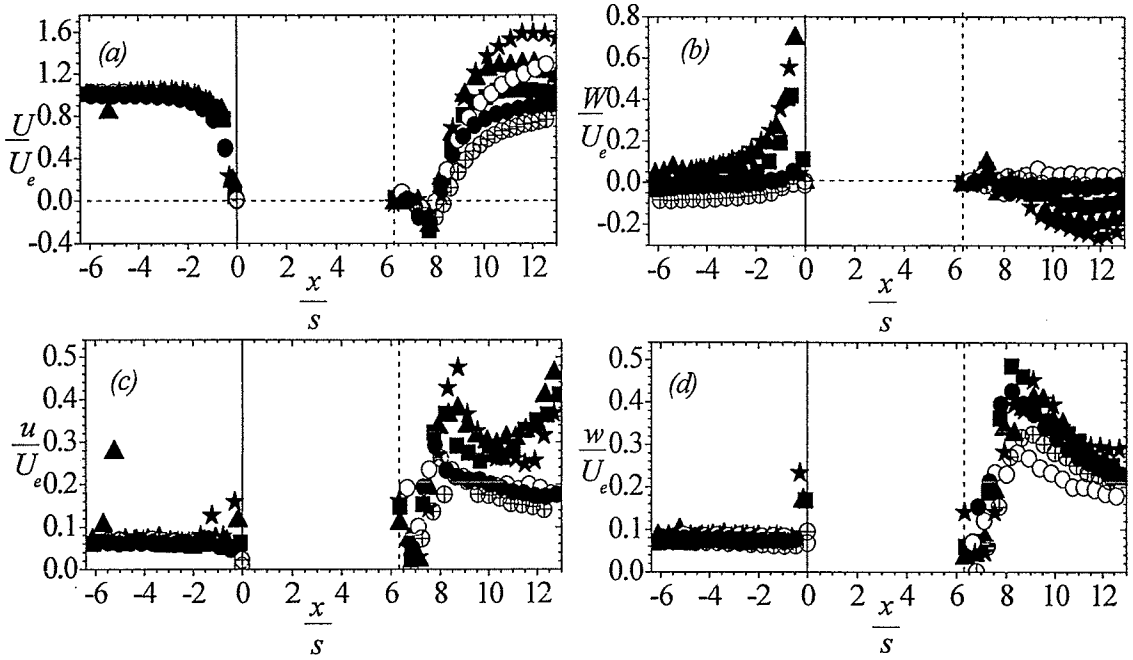

Figure 5.13: Mean velocities: (*a*) streamwise and (*b*) spanwise; and turbulence intensities: (*c*) streamwise and (*d*) spanwise along the wake axis: ($\theta_0U_{0.26}$: ⊕; $\theta_0U_{0.52}$: ●; $\theta_0U_{0.76}$: ○; $\theta_6U_{0.52}$: ■; $\theta_9U_{0.52}$: ▲; $\theta_{12}U_{0.52}$: ★)

($\theta = 0^o$), and for a constant U_e = 0.52 m/s, it increased substantially with θ. For $\theta_0U_{0.76}$, d_{max} occurred at x/s = 19 (which is beyond the range over which data are plotted). Therefore, U_{max}/U_e for $\theta_0U_{0.76}$ is higher than values plotted in Figure 5.13a. Figure 5.13b shows that $(W/U_e)_{min} \approx \pm 0.03$ for the aligned bars while corresponding values for $\theta_6U_{0.52}$, $\theta_9U_{0.52}$ and $\theta_{12}U_{0.52}$ are, respectively, -0.12, -0.20 and -0.26.

The turbulence intensities increased rapidly along the wake centerline to a maximum. The peak value ($u_{max}/U_e \approx 0.27$) is nearly independent of Reynolds number for the aligned bars but it increased to 0.50 for $\theta_{12}U_{0.52}$. Unlike the aligned bars, the values of u/U_e behind the inclined bars did not decrease monotonically. Instead, they decreased to a

minimum value at x/s = 10 ($\theta_6 U_{0.52}$, $\theta_9 U_{0.52}$) or x/s = 12 ($\theta_{12} U_{0.52}$) and increased abruptly thereafter. The values of w_{max}/U_e vary somewhat with Reynolds number but nearly independent of bar inclination ($w_{max}/U_e \approx 0.42$ - 0.45). The large values of u and w in the wake region are due to the vortex shedding from the bars. It is observed that w/U_e is higher than u/U_e for the aligned bars ($w_{max}/u_{max} \approx$ 1.5), but $w_{max}/u_{max} \approx$ 1 for the inclined bars. These results imply that bar inclination promotes a tendency towards local isotropy along the wake axis.

The distribution of mean streamwise velocity along the wake axis for different bar depth and blockage ratios (*Series II*) is shown in Figure 5.14. The values of $(U/U_e)_{min}$ are in the range of -0.08 to -0.26 for the different values of L/s, but remains constant at -0.14 for different blockage ratios. The recirculation bubble length increased from $x_r/s \approx 0.89$ to 1.35 for increasing bar depth (Figure 5.14). The value of x_r/s for SQ-L_{110}-$p_{0.26}$ was 1.58 and 1.44 for SQ-L_{110}-$p_{0.33}$. In accordance with the data plotted in Figure 5.2b, U_{max}/U_e increased with blockage ratio with no discernable dependence on bar depth.

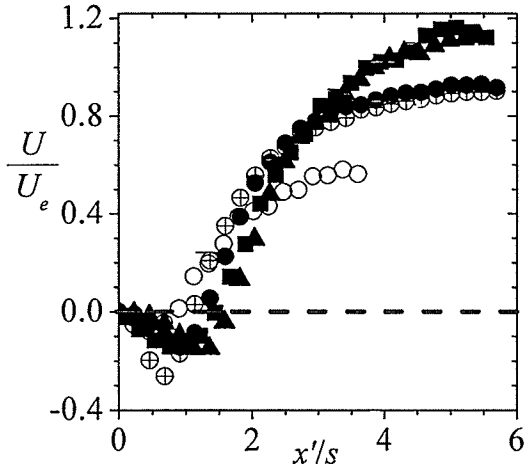

Figure 5.14: Mean streamwise velocity along the wake axis of the bars: SQ-L_{50}-$p_{0.20}$: ○; SQ-L_{76}-$p_{0.20}$: ⊕; SQ-L_{110}-$p_{0.20}$: ●; SQ-L_{110}-$p_{0.26}$: ▲; SQ-L_{110}-$p_{0.33}$: ■

Figure 5.15 shows the distributions of mean streamwise velocities and turbulence intensities along the wake axes for *Series III*. Negative values for U are observed in the recirculation region behind the rectangular bars (Figure 5.15a). The values of $(U/U_e)_{min}$ are -0.04, -0.08 and -0.18, respectively, for SQ-s_6-L_{50}, SQ-s_9-L_{50} and SQ-s_{12}-L_{50}. For the different bar depth, the values of $(U/U_e)_{min}$ are in the range of -0.18 to -0.23, but nearly 0 for the streamlined bars. The recirculation bubble length for different bar thicknesses are $x_r/s \approx 0.64$, 0.90 to 0.97, respectively, for SQ-s_6-L_{50}, SQ-s_9-L_{50} and SQ-s_{12}-L_{50}. The recirculation bubble length for the different bar depths varies from $x_r/s \approx 0.90$ to 1.06, but nearly 0 for the streamlined bars. Furthermore, values of U/U_e obtained downstream

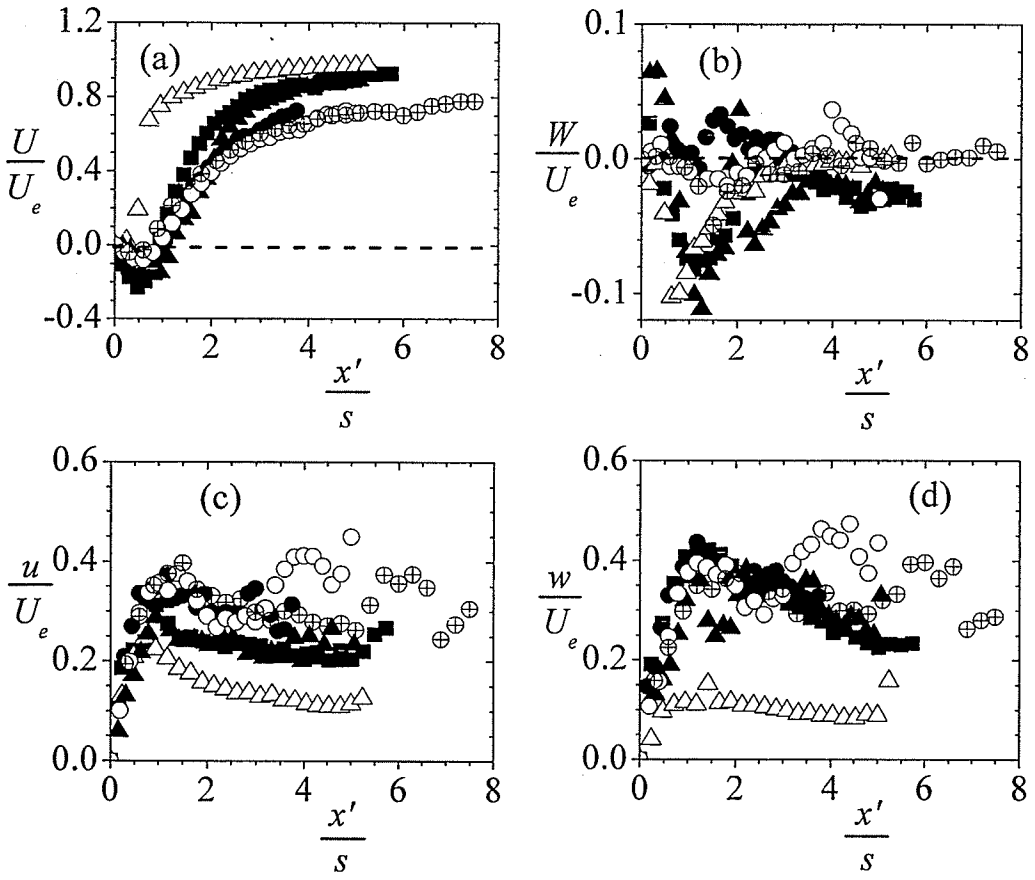

Figure 5.15: Mean velocities: (*a*) streamwise and (*b*) spanwise; and turbulence intensities: (*c*) streamwise and (*d*) spanwise along the wake axis: (SQ-s_6-L_{50}: ⊕; SQ-s_9-L_{50}: ○; SQ-s_{12}-L_{50}: ●; SQ-s_{12}-L_{76}: ■; SQ-s_{12}-L_{100}: ▲; ST-s_{12}-L_{100}: △)

of the streamlined bars rose abruptly to its maximum. The $(u/U_e)_{max}$ and $(w/U_e)_{max}$ are highest for the rectangular bars; however, they are least for streamlined. For example, $(w/U_e)_{max} \approx 0.45$ for SQ-s_{12}-L_{100}, whereas the corresponding value for the streamlined bar (ST-s_{12}-L_{100}) is approximately 0.15.

Distributions of the mean velocities extracted at $z''/b_a = 0.5$, and parallel to the x^*-axis are shown in Figure 5.16. As indicated in Figure 4.2, the location $z''/b_a = 0.5$ is midway between the two bars around which detailed measurements were conducted while the x^*-axis is parallel to the bars (rather than the side walls of the channel). As in Figure 5.13, the solid and dotted vertical lines are used, respectively, to demarcate the leading edge

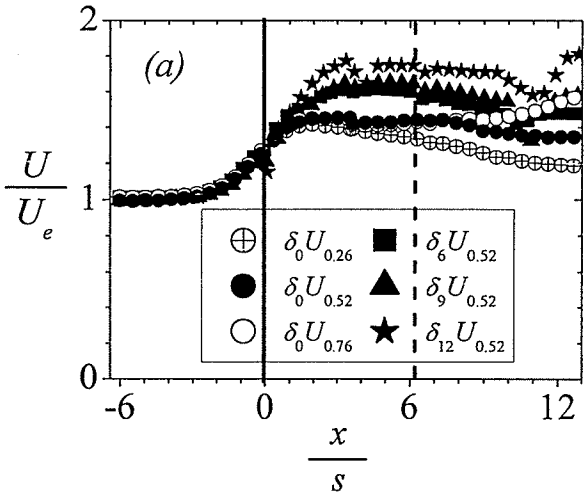

Figure 5.16: Mean streamwise velocity at the centre ($z''/b_a = 0.5$) of two bars.

and trailing edge of the bars. These plots are used to highlight the magnitude of the mean velocities between the various trashrack bars. At the leading edges of both the aligned and inclined bars, the mean velocity increased to 1.25 of the approach velocity. Inside the bars, the higher effective sectional blockage produced by the inclined bars accelerated the flow further to $U/U_e = 1.6$ to 1.8 compared with $U/U_e = 1.5$ for the aligned bars.

Fish are usually able to detect flow velocity, acceleration and turbulence, although their responses may differ based on swimming performance capacity, species and sizes (Katopodis [21]). Fish moving downstream may detect the presence of trashracks before physical contact is made and move away, if their swimming ability is higher than water velocities near the trashracks. Those fish large enough to physically be excluded by trashrack spacing may also be able to overcome such water velocities. Water velocities and accelerating flows which may overwhelm particularly smaller fish may be those between trashrack bars downstream of the leading edge. Figures 5.13a and 5.16 show how water velocities increase between bars. These velocities may exceed the swimming capability of certain sizes of fish. As a result these fish may be unable to escape upstream and instead pass through turbines with potential for injury or mortality.

5.2.4. Profiles of Mean Velocities across the Wake Axes

Figures 5.17 to 5.22 show profiles across the channel at selected streamwise locations upstream of the bars, within the bars and downstream of the bars. At the upstream location, profiles are plotted from the side wall to the mid-plane and z is normalized by B. Within the bars, the profiles are normalized by the clear space between adjacent bars (b) whereas the center-to-center spacing (b_a) is used to normalize z or z'' (in case of more than three bars) at the downstream locations. The mean velocities and turbulent quantities are made dimensionless by U_e.

In Figures 5.17 and 5.18, profiles were plotted at upstream of the bars (x/s = -5 and -1), within the bars (x_c/s, x/s = 4) and downstream of the bars (x'/s = 1, 2, 4 and 17 or 60). It

should be noted that x_c corresponds to the x-location where the critical points or centers of recirculation bubbles occurred close to the bar leading edge. These locations vary from test case to test case. The values of x'/s = 17 corresponds to the streamwise location where the freestream water level is nearly independent of streamwise distance for tests $\delta_o U_{0.26}$, $\delta_o U_{0.52}$, $\delta_6 U_{0.52}$, $\delta_9 U_{0.52}$ and $\delta_{12} U_{0.52}$ whereas x'/s = 60 corresponds to the location where the freestream water level is nearly independent of streamwise distance for test $\delta_0 U_{0.76}$. Upstream of the bars, the streamwise mean velocities (U/U_e) are nearly independent of bar inclination and Reynolds number (Figures 5.17a and 5.17b). At x/s = -5, the effects of channel wall (as revealed by the boundary layer) are confined to $z/B \leq$ 0.2. Meanwhile, the profiles at x/s = -1 are no longer uniform across the channel, an indication that the presence of the bars are felt at this upstream location. At this location, fish would begin to feel noticeable changes in the flow velocities (see also Figure 5.18b). The mean velocity profiles obtained between and downstream of the aligned bars collapsed reasonably well indicating no significant Reynolds number effect. These profiles are also nearly symmetric with respect to z'/b = 0.5 and z''/b = 0.5. Significant differences are observed between the profiles for the aligned bars and those for the inclined bars. For example, the profiles for the inclined bars are asymmetric, and their $(U/U_e)_{max}$ are substantially higher than those measured for the aligned bars. The interaction between the two distinct wake regions observed downstream of the inclined bars (Figure 5.3) produced flow discontinuity in the mean profiles around $z''/b_a \approx 0.8$ (at x'/s = 2), and $z''/b_a \approx 0.65$ (at x'/s = 4), Figures 5.17 and 5.18. It should be noted that the wider low velocity regions adjacent to z'/b = 1 is consistent with the wider recirculation bubbles on the leeward sides of the inclined bars. Figure 5.17 also show that as the bar

inclination increased, the magnitudes of W/U_e increased substantially. At x/s = 4, for example, $-(W/U_e)_{max}$ rose to 60% for $\delta_{12}U_{0.52}$ compared to 10% or less for the aligned bars. The differences between the mean velocity profiles for aligned and inclined profiles are still evident at x'/s = 17 and 60.

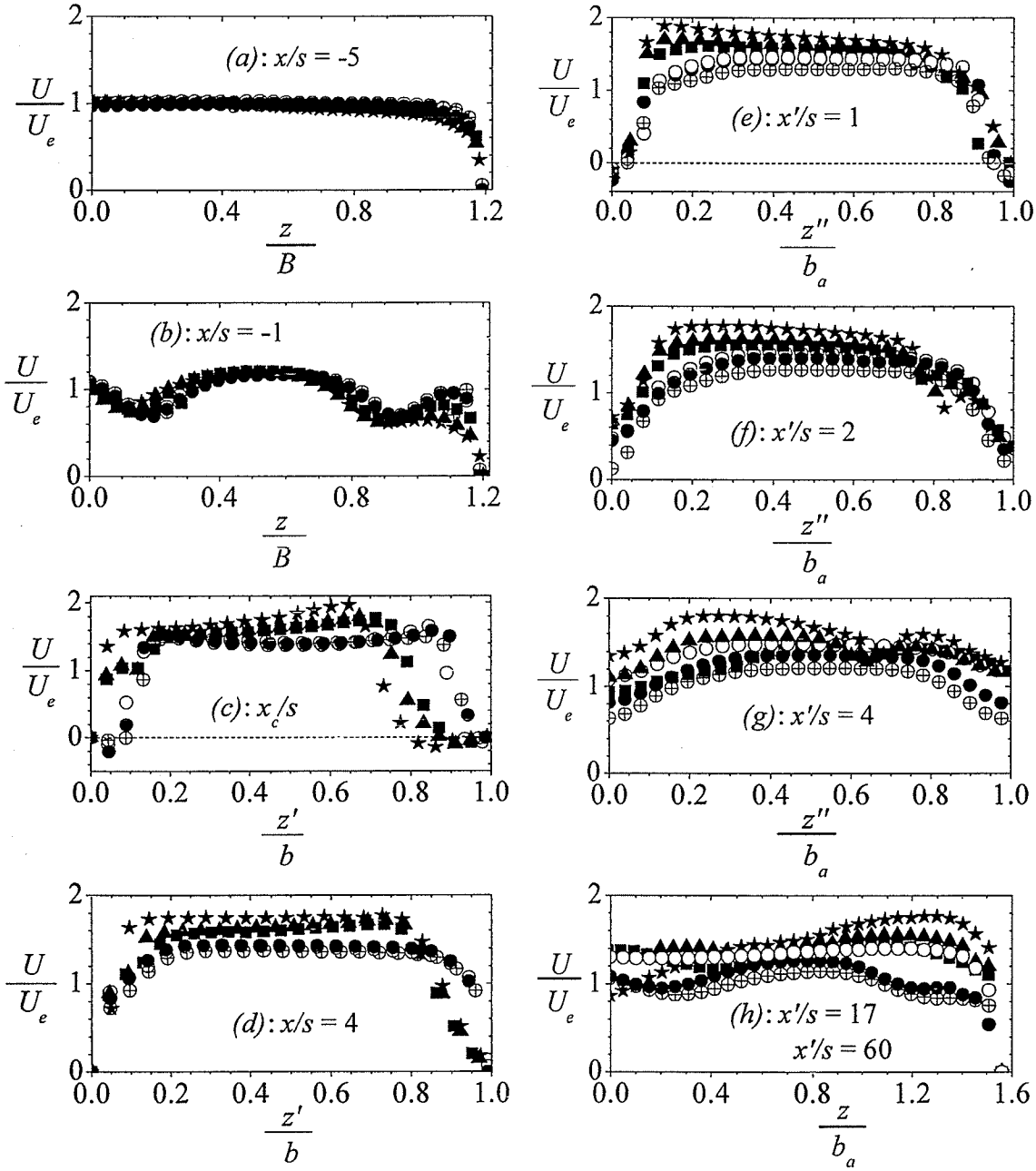

Figure 5.17: Mean streamwise velocity profiles across the channel at selected streamwise locations: ($\theta_0U_{0.26}$: ⊕; $\theta_0U_{0.52}$: ●; $\theta_0U_{0.76}$: ○; $\theta_6U_{0.52}$: ■; $\theta_9U_{0.52}$: ▲; $\theta_{12}U_{0.52}$: ★)

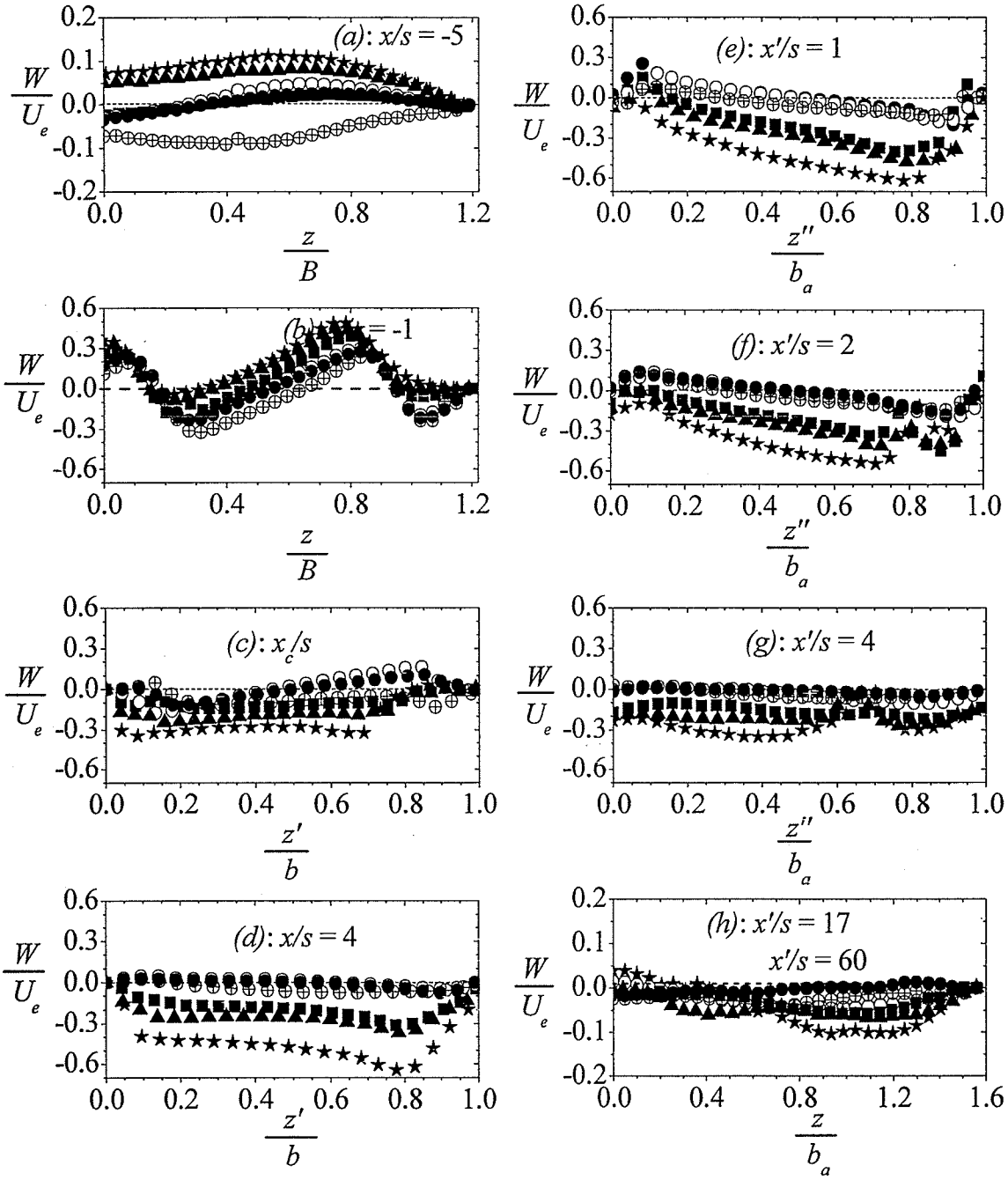

Figure 5.18: Mean spanwise velocity profiles across the channel at selected streamwise locations: ($\theta_0 U_{0.26}$: ⊕; $\theta_0 U_{0.52}$: ●; $\theta_0 U_{0.76}$: ○; $\theta_6 U_{0.52}$: ■; $\theta_9 U_{0.52}$: ▲; $\theta_{12} U_{0.52}$: ★)

The dependence of the mean velocities on the bar depth and blockage ratio is shown in Figures 5.19 and 5.20. The profiles were selected at streamwise locations: upstream (x/s = -1), within the bars ($x/s = x_c$ and $x/L = 0.5$) and downstream of the bars (x'/s = 1, 2 and 5). As noted earlier, x_c corresponds to the x-location where the centers of recirculation bubbles occurred close to the bar leading edge, whereas $x/L = 0.5$ is the mid-depth of bars for each test condition. The dents observed in Figures 5.19a and 5.20a are due to flow retardation by the presence of the bars. With increasing blockage ratio, the number of dents increases and level of water just upstream of the bars rises. Note that the pair of profiles within and downstream of models with blockage ratio 0.26 (SQ-L_{110}-$p_{0.26}$) and 0.33 (SQ-L_{110}-$p_{0.33}$) is identical to each other, an indication that the flow between any two bars is reproduced in the other pairs of bars. As observed from the flow patterns, most of the profiles of the mean velocities are nearly symmetric. The effects of bar depth on mean velocities are small compared with blockage ratio. Between the bars and downstream of the bars, the figures demonstrate clearly that, an increase in blockage ratio increases the magnitude of U. For example, as the blockage ratio increased from 0.20 (SQ-L_{110}-$p_{0.20}$) to 0.33 (SQ-L_{110}-$p_{0.33}$), the profiles at $x/L = 0.5$ show that $(U/U_e)_{max}$ rose from 145% to 180% (Figure 5.19c).

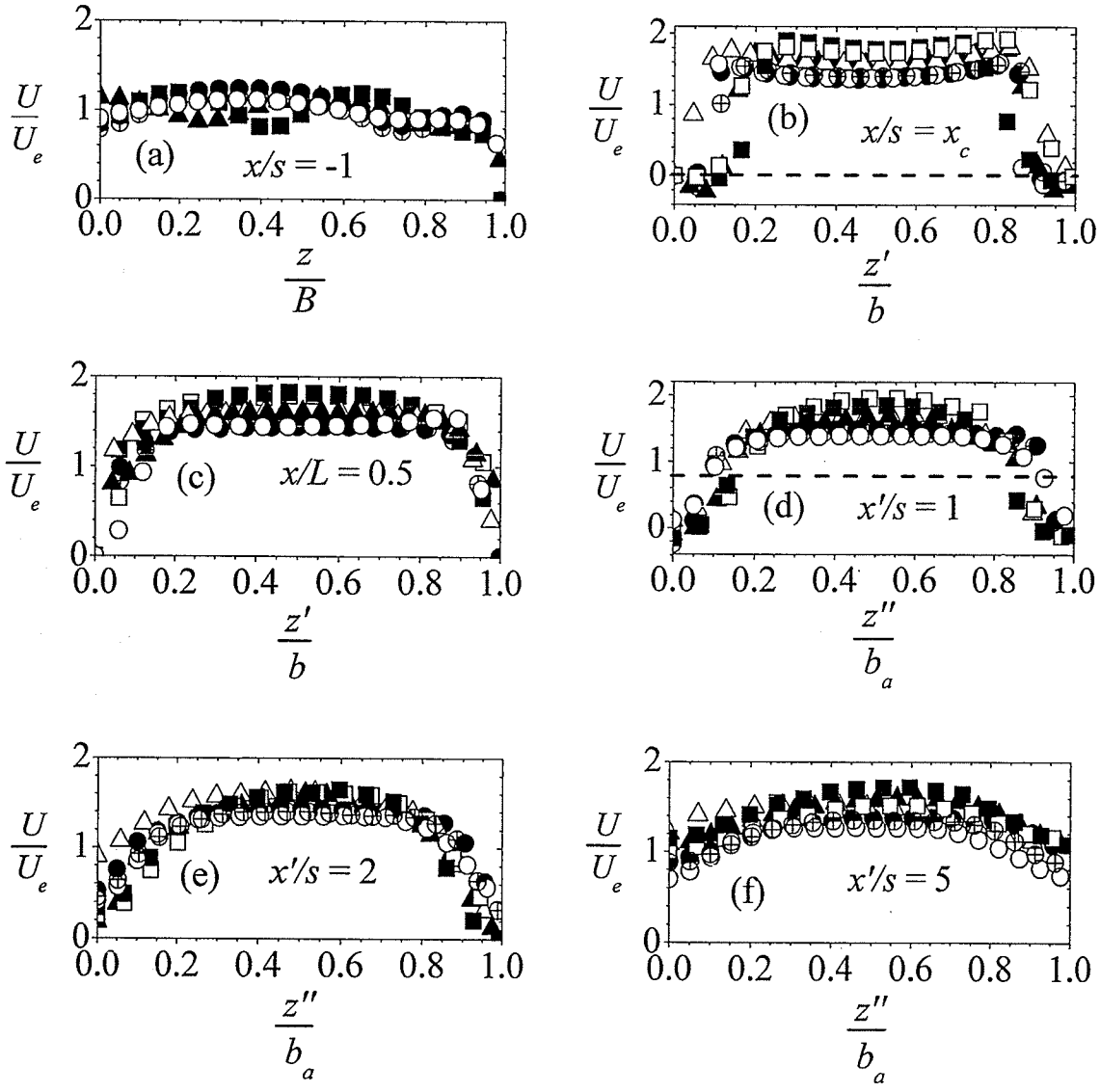

Figure 5.19: Mean streamwise velocity profiles across the channel at selected streamwise locations: SQ-L_{50}-$p_{0.20}$: ○; SQ-L_{76}-$p_{0.20}$: ⊕; SQ-L_{110}-$p_{0.20}$: ●; SQ-L_{110}-$p_{0.26}$: ▲ and △; SQ-L_{110}-$p_{0.33}$: ■ and □.

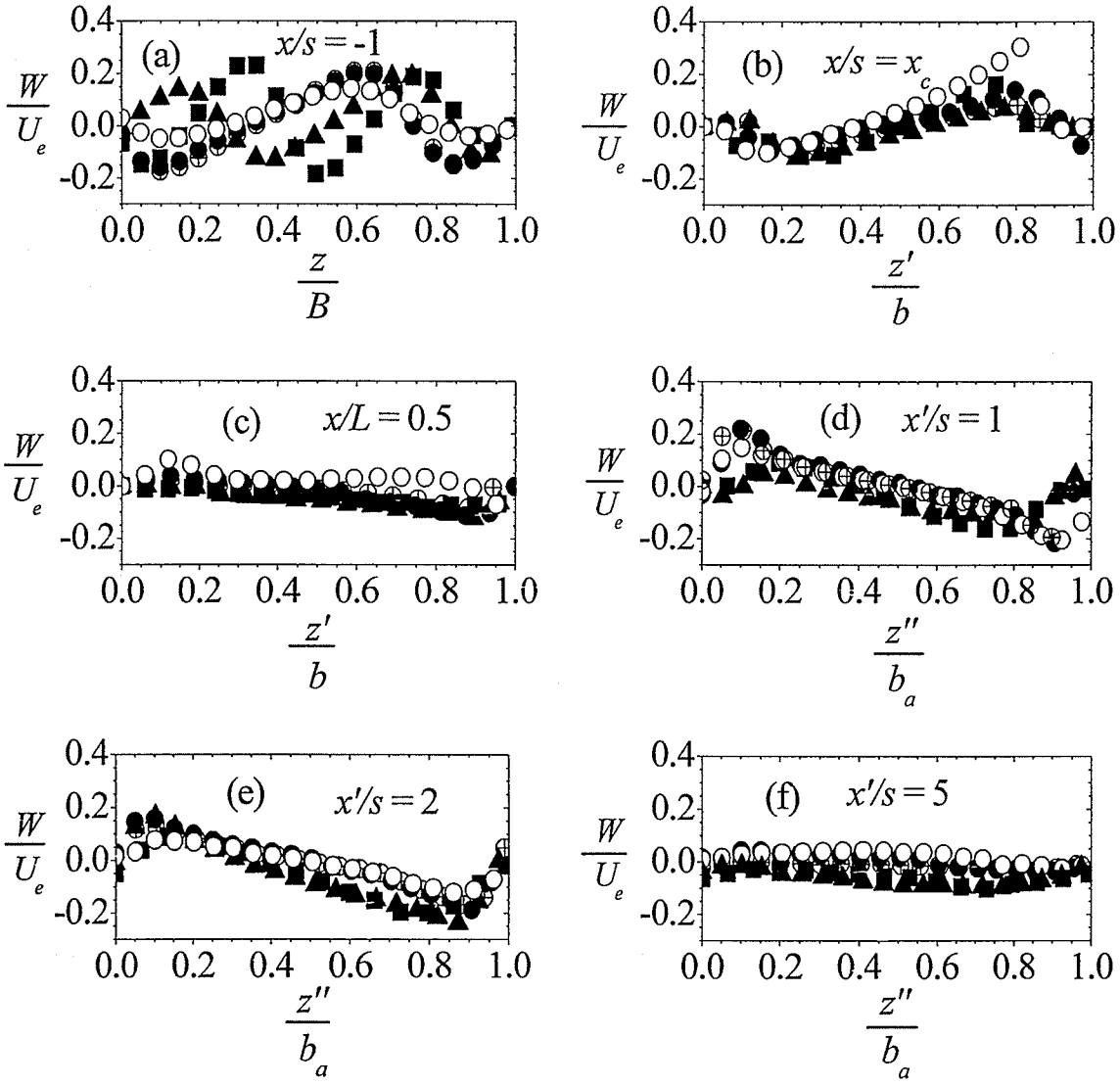

Figure 5.20: Mean spanwise velocity profiles across the channel at selected streamwise locations: SQ-L_{50}-$p_{0.20}$: ○; SQ-L_{76}-$p_{0.20}$: ⊕; SQ-L_{110}-$p_{0.20}$: ●; SQ-L_{110}-$p_{0.26}$: ▲; SQ-L_{110}-$p_{0.33}$: ■

The effects of bar depth, bar thickness and shape on the mean velocity profiles across the channel are shown in Figures 5.21 and 5.22. The profiles were selected at streamwise locations: upstream (x/s = -1), within the bars (x/L = 0.50 and 0.75) and downstream of the bars (x'/s = 1, 2.5 and 5). The effects of bar depth on these profiles are minimal

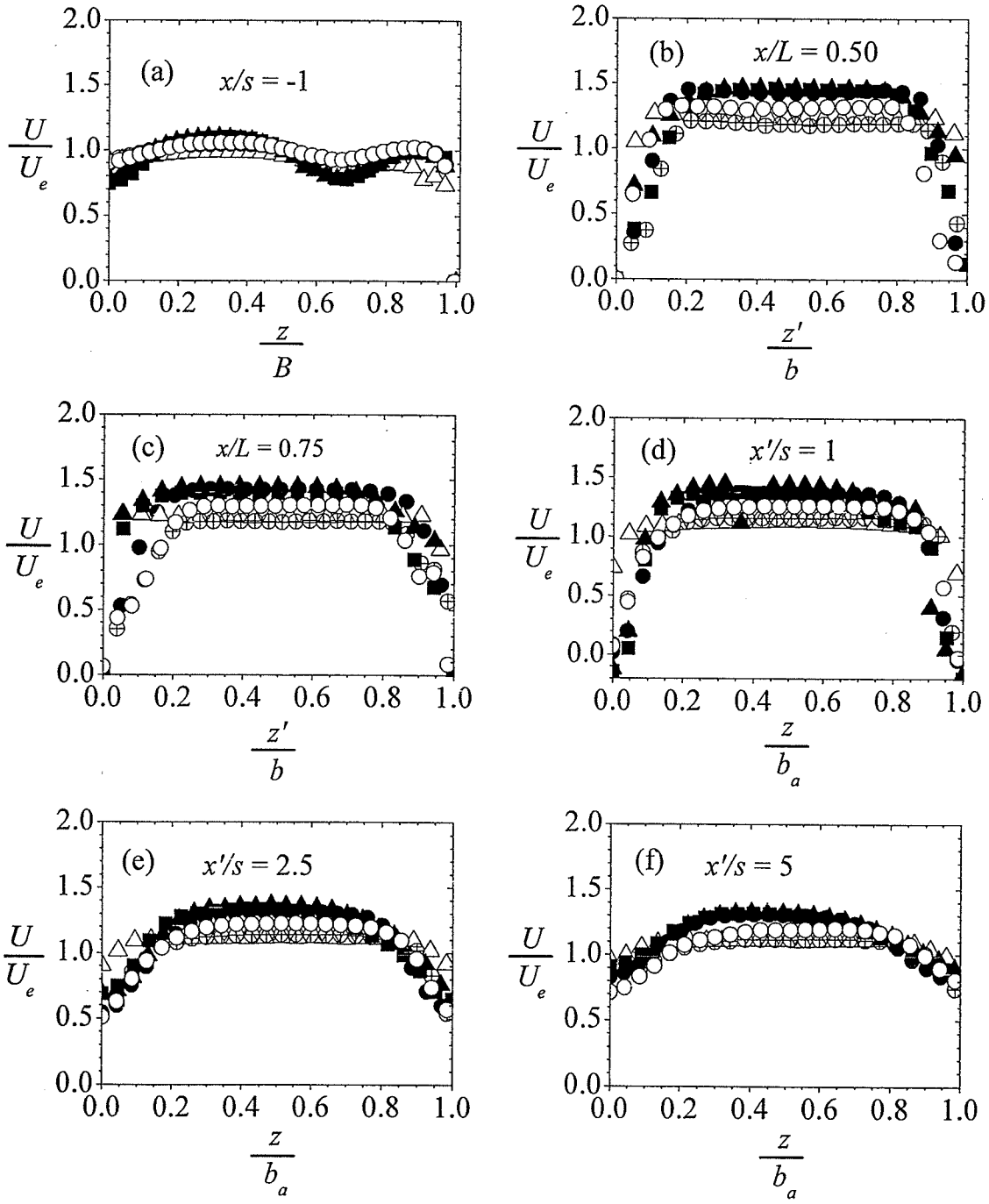

Figure 5.21: Mean streamwise velocity profiles across the channel at selected streamwise locations: (SQ-s_6-L_{50}: ⊕; SQ-s_9-L_{50}: ○; SQ-s_{12}-L_{50}: ●; SQ-s_{12}-L_{76}: ■; SQ-s_{12}-L_{100}: ▲; ST-s_{12}-L_{100}: △)

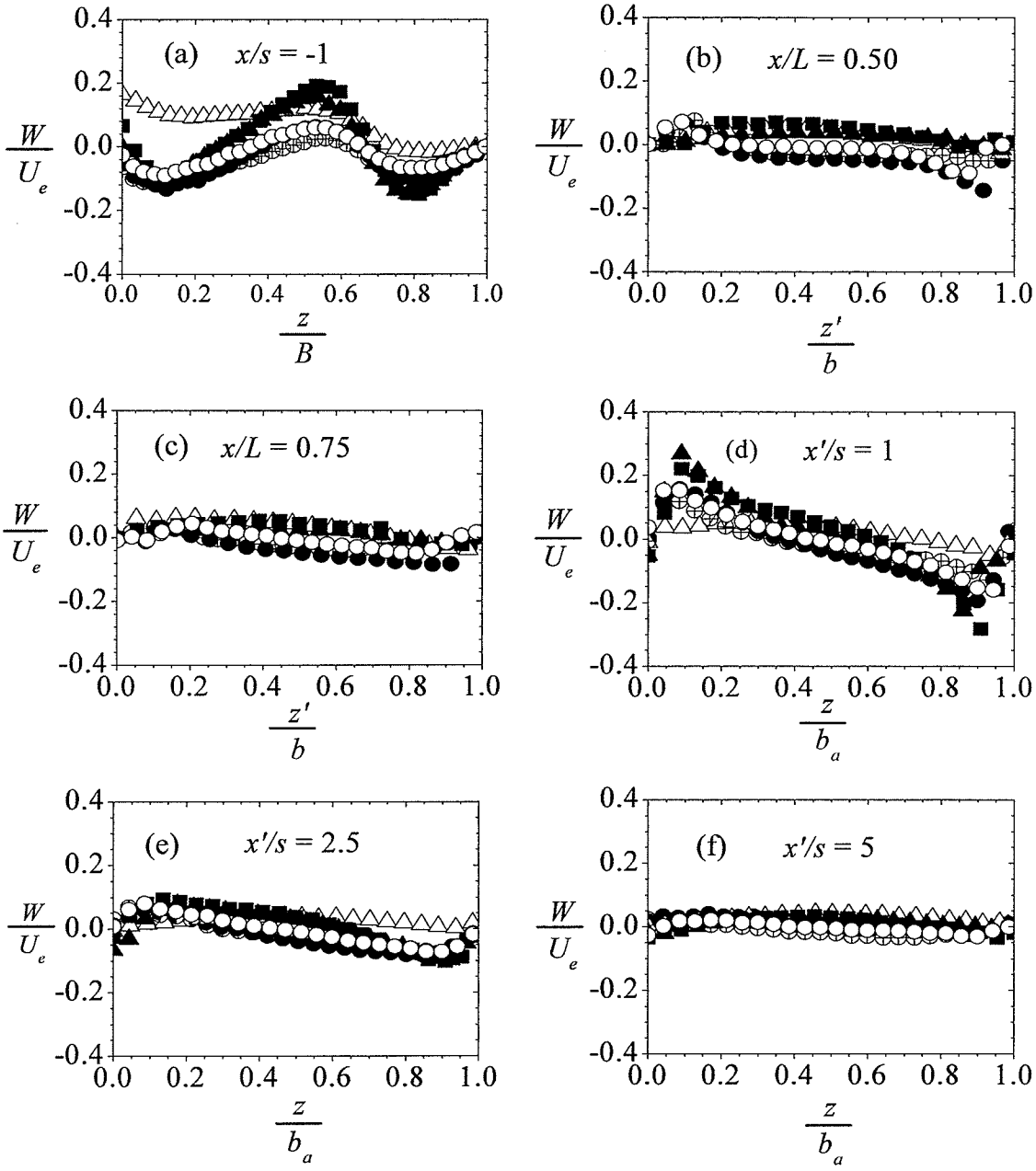

Figure 5.22: Mean spanwise velocity profiles across the channel at selected streamwise locations: (SQ-s_6-L_{50}: ⊕; SQ-s_9-L_{50}: ○; SQ-s_{12}-L_{50}: ●; SQ-s_{12}-L_{76}: ■; SQ-s_{12}-L_{100}: ▲; ST-s_{12}-L_{100}: △)

compared with bar thickness and shape. Whereas the profiles of U for the rectangular bars with different bar depth but the same thickness collapse reasonably well, the profiles

for the streamlined bars and rectangular bars with thicknesses other than s = 12 mm are relatively lower. For example, as the bar shape was changed from rectangular (SQ-s_{12}-L_{100}) to streamlined bars (ST-s_{12}-L_{100}), the profiles at x/L = 0.50 show that $(U/U_e)_{max}$ decreased from about 150% to 130% (Figure 5.21c). The decreased in values of $(U/U_e)_{max}$ as observed in Figure 5.21f is consistent with the rising water level (Figure 5.2c). At x'/s = 5, the profiles of W are nearly independent of bar depth, thickness and shape (Figure 5.22f).

5.2.5 Turbulence Intensities and Reynolds Shear Stress across the Wake Axes

The corresponding profiles of turbulent statistics for the mean velocities across the channel are discussed in this section. The turbulent quantities plotted are the turbulence intensities and Reynolds shear stress. Figures 5.23 to 5.25 also show that profiles of the turbulence intensities and Reynolds shear stress for the aligned bars are also independent of Reynolds number. This observation is valid upstream of the bars, between the bars and downstream of the bars. For the aligned bars, the regions of elevated turbulence level is confined to the immediate vicinity of the bars (z'/b_a = 0 and 1) or close to z''/b_a = 0 and 1. The turbulence intensities and Reynolds shear stress around and downstream of the inclined bars are relatively higher compared with the data obtained for the aligned bars. In contrast to the near-symmetry distribution observed for the aligned bars, the turbulence intensities and Reynolds shear stress are much higher on the leeward sides of the inclined bars than on the windward sides. This can be attributed to the unsteady recirculation bubbles that were formed on the leeward sides of these bars. Similar to the mean velocities, it is observed that the interaction between the two distinct wake regions

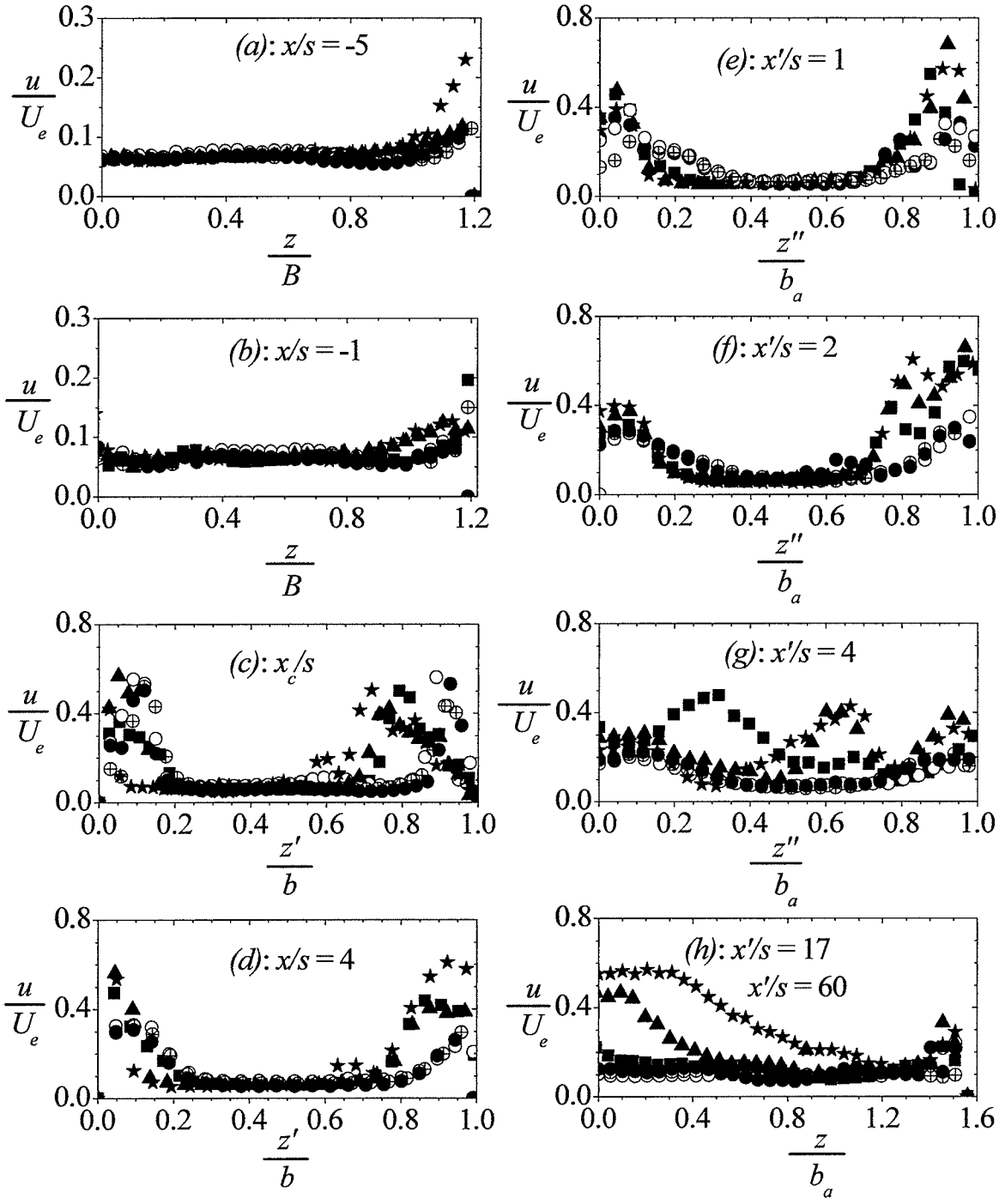

Figure 5.23: Streamwise turbulence intensity profiles across the channel at selected streamwise locations: ($\theta_0 U_{0.26}$: ⊕; $\theta_0 U_{0.52}$: ●; $\theta_0 U_{0.76}$: ○; $\theta_6 U_{0.52}$: ■; $\theta_9 U_{0.52}$: ▲; $\theta_{12} U_{0.52}$: ★)

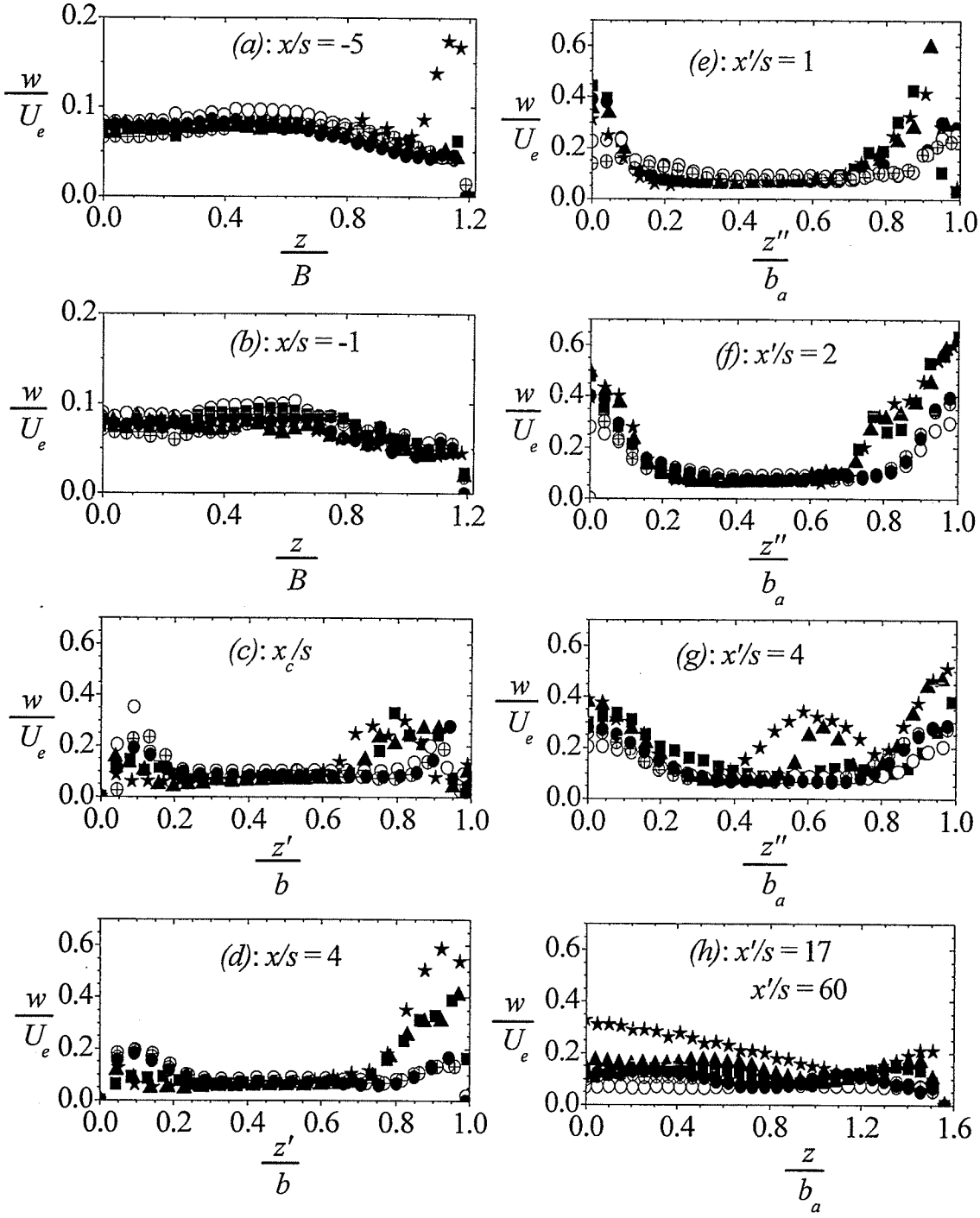

Figure 5.24: Spanwise turbulence intensity profiles across the channel at selected streamwise locations: ($\theta_0U_{0.26}$: ⊕; $\theta_0U_{0.52}$: ●; $\theta_0U_{0.76}$: ○; $\theta_6U_{0.52}$: ■; $\theta_9U_{0.52}$: ▲; $\theta_{12}U_{0.52}$: ★)

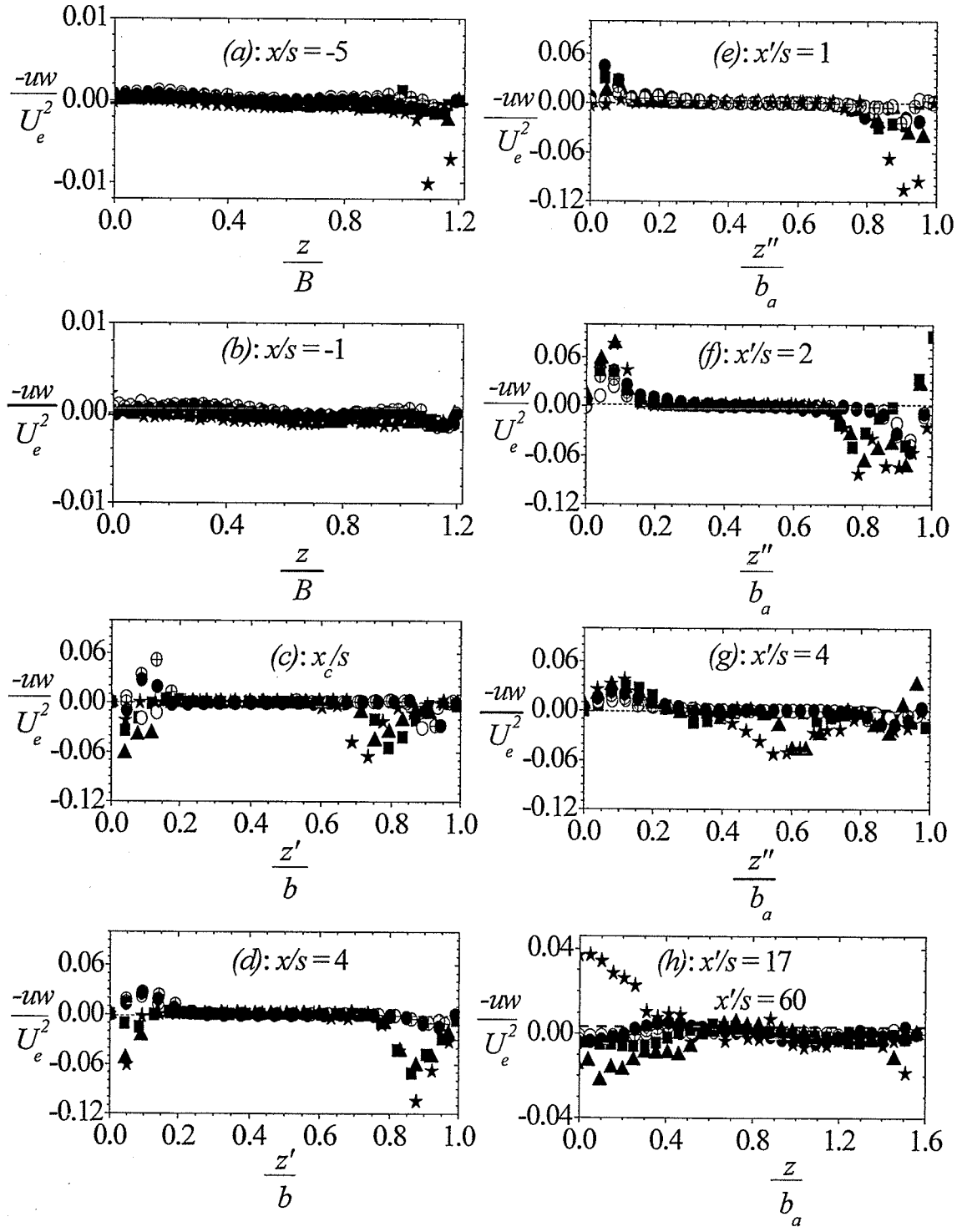

Figure 5.25: Reynolds shear stress profiles across the channel at selected streamwise locations: ($\theta_0U_{0.26}$: ⊕; $\theta_0U_{0.52}$: ●; $\theta_0U_{0.76}$: ○; $\theta_6U_{0.52}$: ■; $\theta_9U_{0.52}$: ▲; $\theta_{12}U_{0.52}$: ★)

observed downstream of the inclined bars produced discontinuity in the turbulent profiles around $z''/b_a \approx 0.8$ (at $x'/s = 2$), and $z''/b_a \approx 0.65$ (at $x'/s = 4$). For the most severe bar inclination ($\delta_{12}U_{0.52}$) considered in the present study, the turbulence intensities and Reynolds shear stress obtained across the channel at $x'/s = 60$ are still significantly higher than those obtained for the other test cases at $x'/s = 17$. This implies that, in view of the substantial flow distortion produced by the more severe bar inclinations, large downstream distance is required before the profiles of turbulence intensities and Reynolds shear stress across the channel become uniform.

The dependence of the turbulent quantities on the bar depth and blockage ratio is shown in Figures 5.26 to 5.28. Most of the profiles of the turbulent quantities are nearly symmetric. The effects of bar depth on turbulent statistics are small compared with blockage ratio. Between the bars and downstream of the bars, the figures demonstrate clearly that, an increase in blockage ratio increases the magnitude of u, w and $-uw$. For example, as the blockage ratio increased from 0.20 (SQ-L_{110}-$p_{0.20}$) to 0.33 (SQ-L_{110}-$p_{0.33}$), the profiles at $x/L = 0.5$ show that $(u/U_e)_{max}$ increased from 80% to 98% (Figure 5.26c), and $(w/U_e)_{max}$ increased from 24% to 64% (Figure 5.27c).

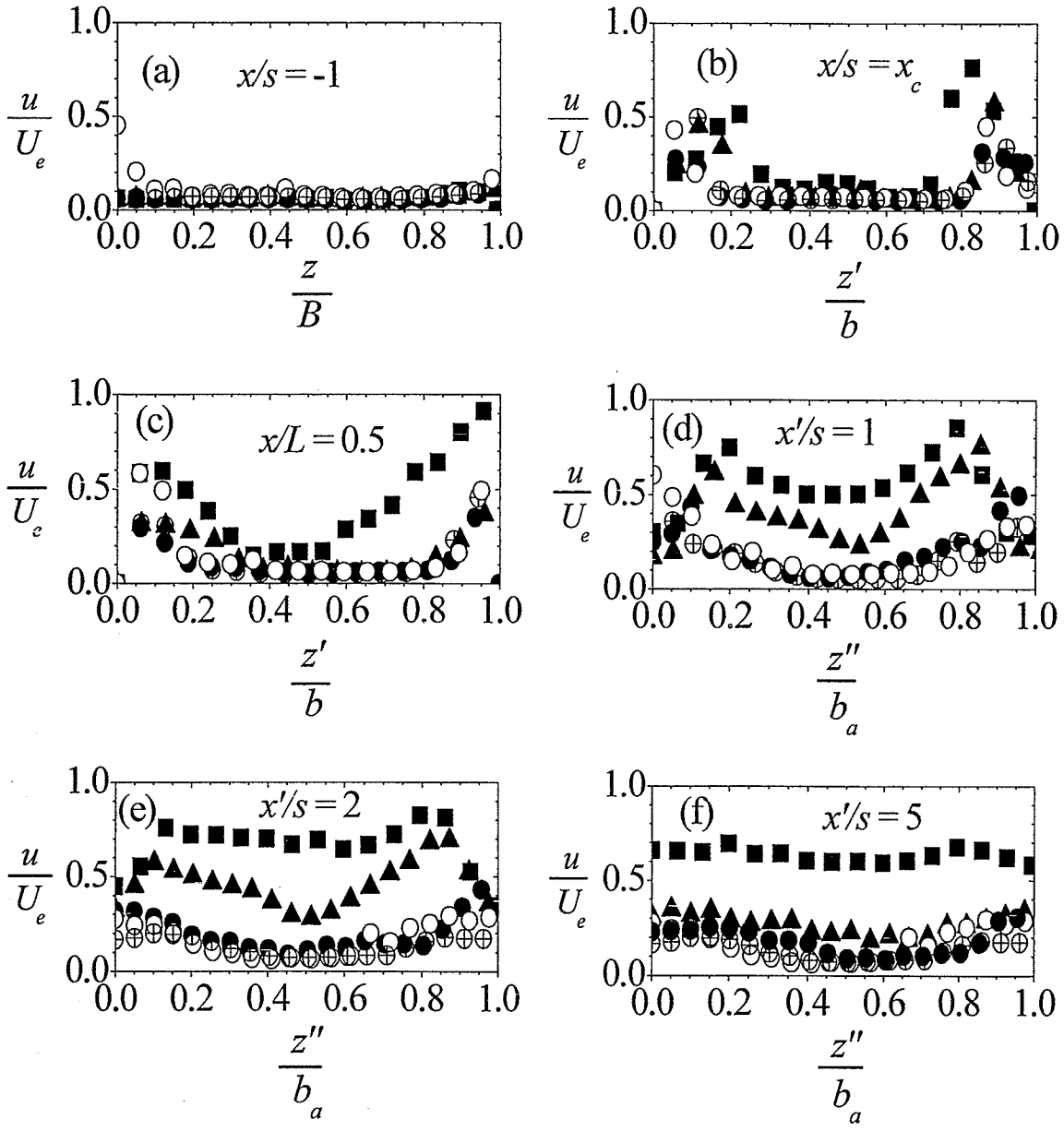

Figure 5.26: Streamwise turbulence intensity profiles across the channel at selected streamwise locations: SQ-L_{50}-$p_{0.20}$: ○; SQ-L_{76}-$p_{0.20}$: ⊕; SQ-L_{110}-$p_{0.20}$: ●; SQ-L_{110}-$p_{0.26}$: ▲; SQ-L_{110}-$p_{0.33}$: ■

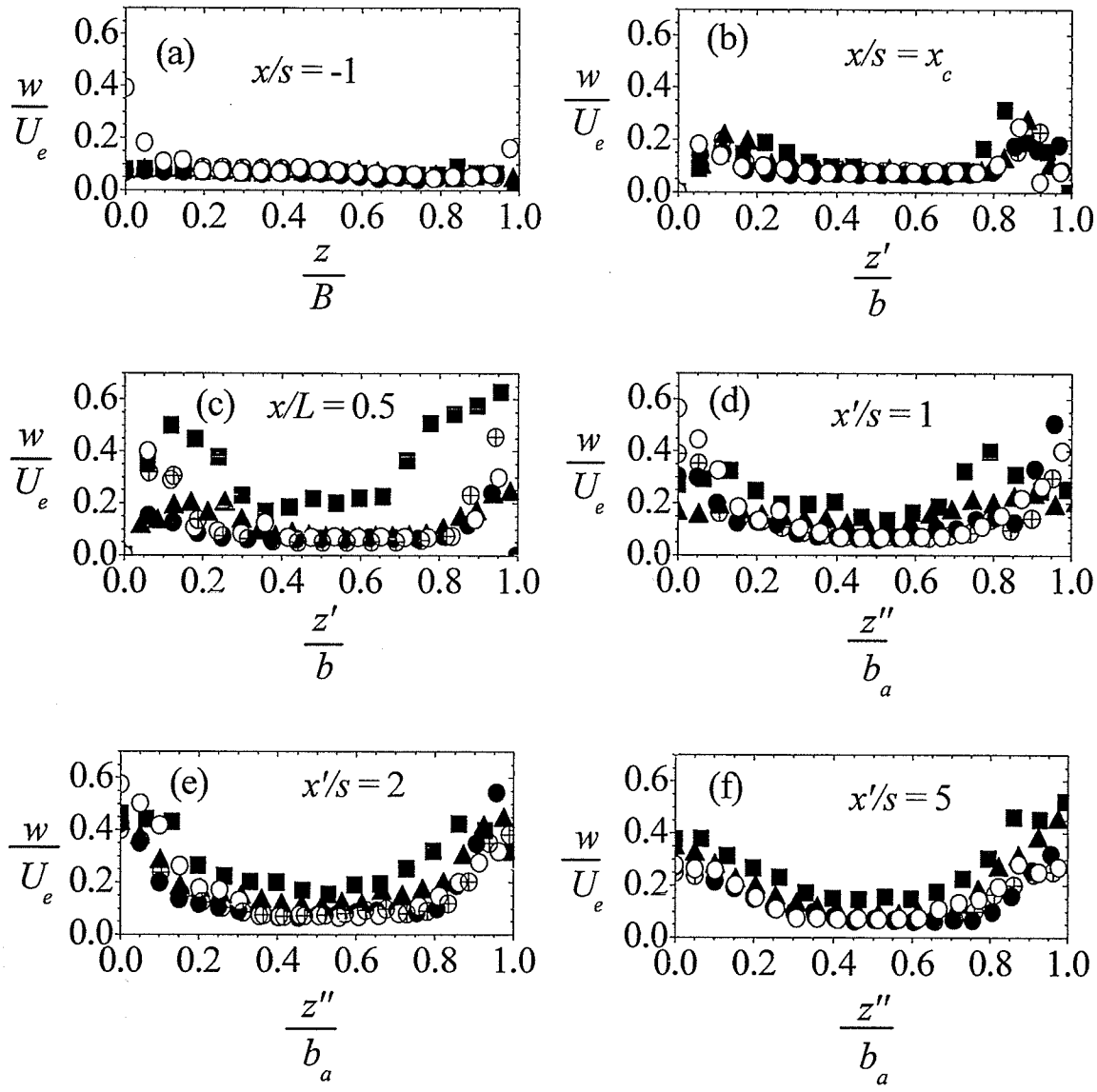

Figure 5.27: Spanwise turbulence intensity profiles across the channel at selected streamwise locations: SQ-L_{50}-$p_{0.20}$: ○; SQ-L_{76}-$p_{0.20}$: ⊕; SQ-L_{110}-$p_{0.20}$: ●; SQ-L_{110}-$p_{0.26}$: ▲; SQ-L_{110}-$p_{0.33}$: ■

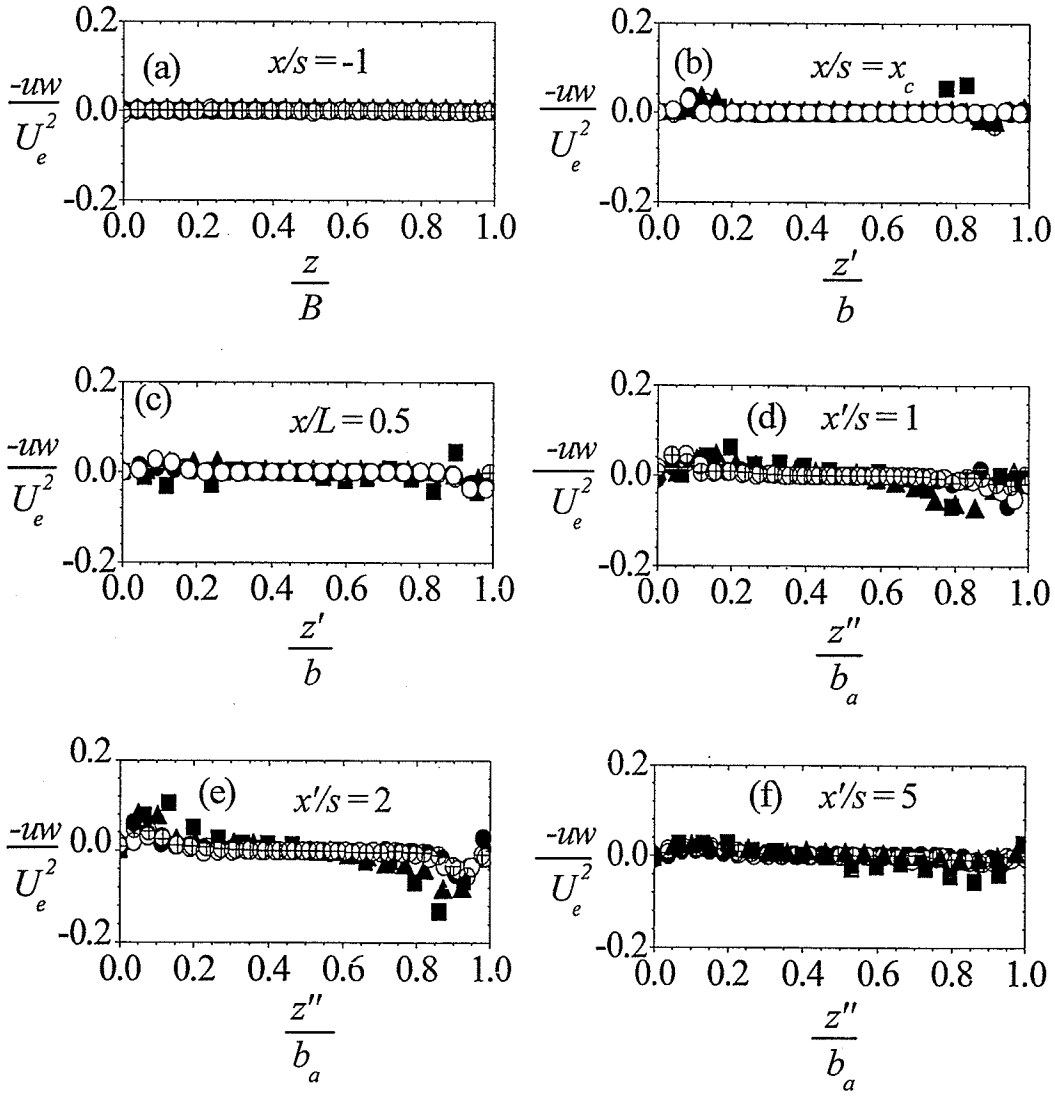

Figure 5.28: Reynolds shear stress profiles across the channel at selected streamwise locations: SQ-L_{50}-$p_{0.20}$: ○; SQ-L_{76}-$p_{0.20}$: ⊕; SQ-L_{110}-$p_{0.20}$: ●; SQ-L_{110}-$p_{0.26}$: ▲; SQ-L_{110}-$p_{0.33}$: ■

Similarly, Figures 5.29 to 5.31 show the effects of bar thickness and shape along with bar depth on the turbulent statistics. The effects of bar thickness and depth on these profiles are small compared to bar shape. The peak values of *u*, *w* and *-uw* profiles for the streamlined bars are consistently lower than that for rectangular bars.

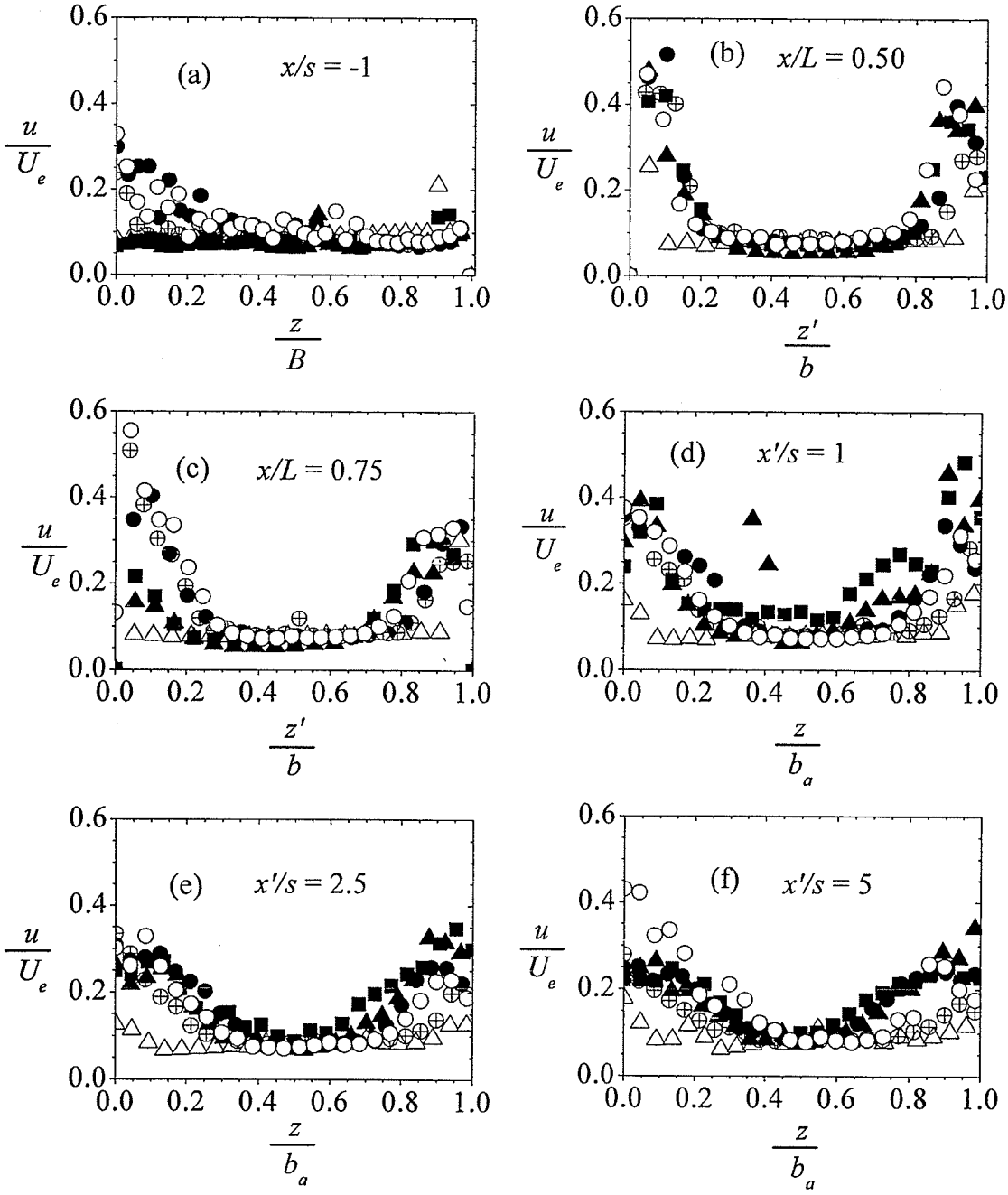

Figure 5.29: Streamwise turbulence intensity profiles across the channel at selected streamwise locations: (SQ-s_6-L_{50}: ⊕; SQ-s_9-L_{50}: ○; SQ-s_{12}-L_{50}: ●; SQ-s_{12}-L_{76}: ■; SQ-s_{12}-L_{100}: ▲; ST-s_{12}-L_{100}: △)

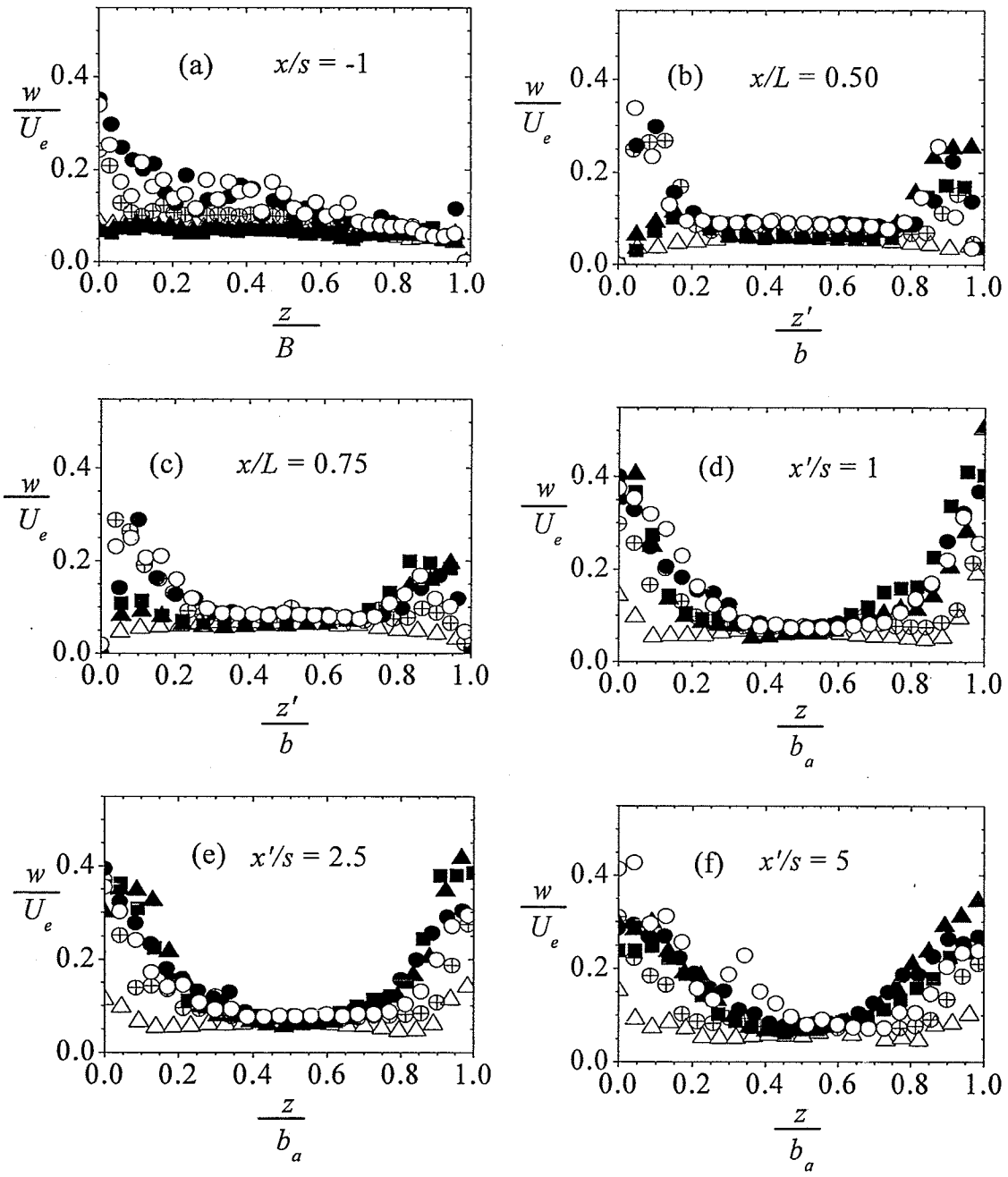

Figure 5.30: Spanwise turbulence intensity profiles across the channel at selected streamwise locations: (SQ-s_6-L_{50}: ⊕; SQ-s_9-L_{50}: ○; SQ-s_{12}-L_{50}: ●; SQ-s_{12}-L_{76}: ■; SQ-s_{12}-L_{100}: ▲; ST-s_{12}-L_{100}: △)

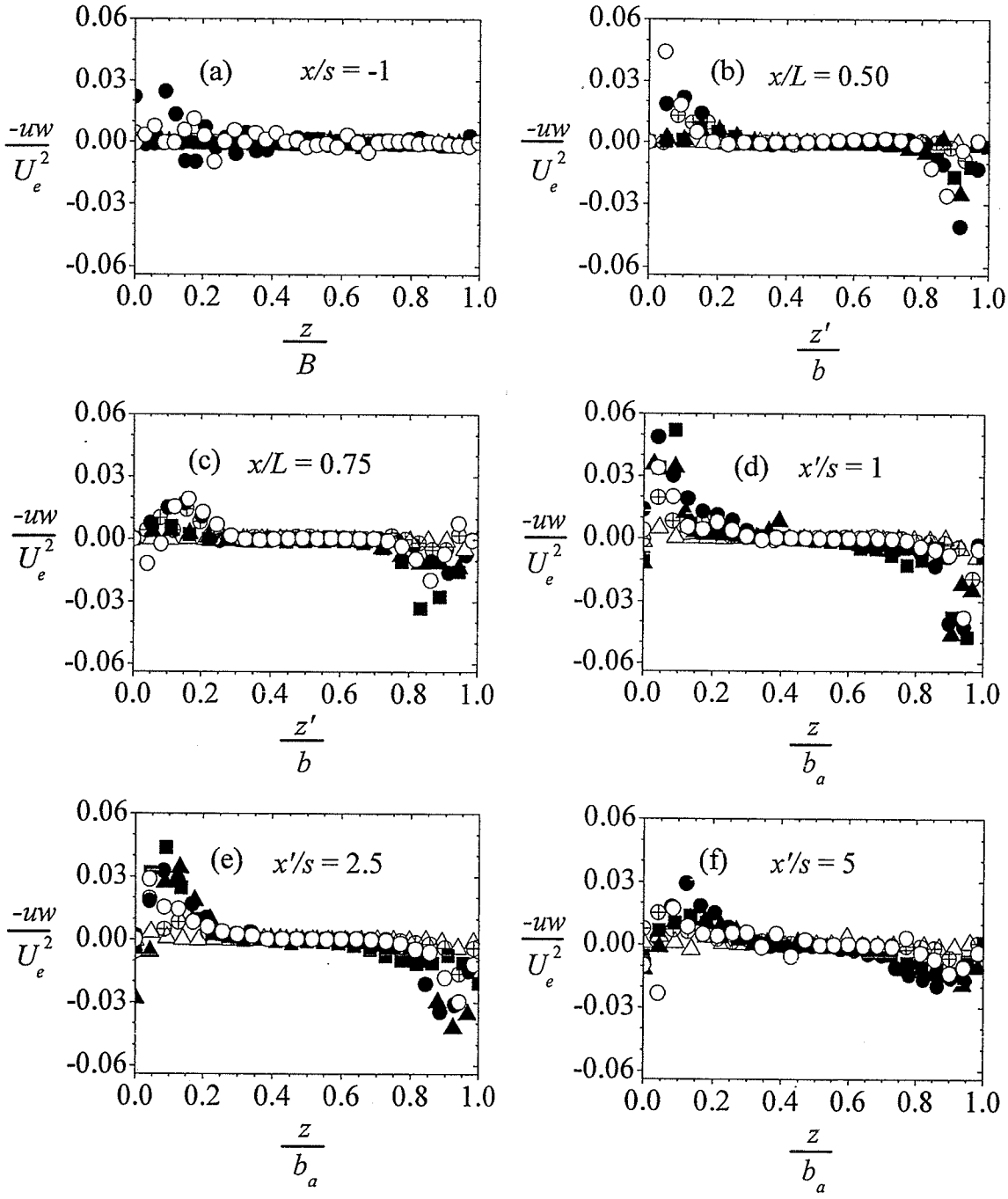

Figure 5.31: Reynolds shear stress profiles across the channel at selected streamwise locations: SQ-L_{50}-$p_{0.20}$: (SQ-s_6-L_{50}: ⊕; SQ-s_9-L_{50}: ○; SQ-s_{12}-L_{50}: ●; SQ-s_{12}-L_{76}: ■; SQ-s_{12}-L_{100}: ▲; ST-s_{12}-L_{100}: △)

5.2.6 Production of Turbulent Kinetic Energy

The full transport equation for the turbulent kinetic energy (TKE) can be found, for example, in Hinze [22]. For a quasi two-dimensional turbulent flow, the production terms in the TKE is $P_T = [-uw(\partial U/\partial z+\partial W/\partial x)]-[u^2\partial U/\partial x+w^2\partial W/\partial z]$. The derivatives in the above expression were obtained using second order central differencing scheme. The total production term as well as the individual components of the production term

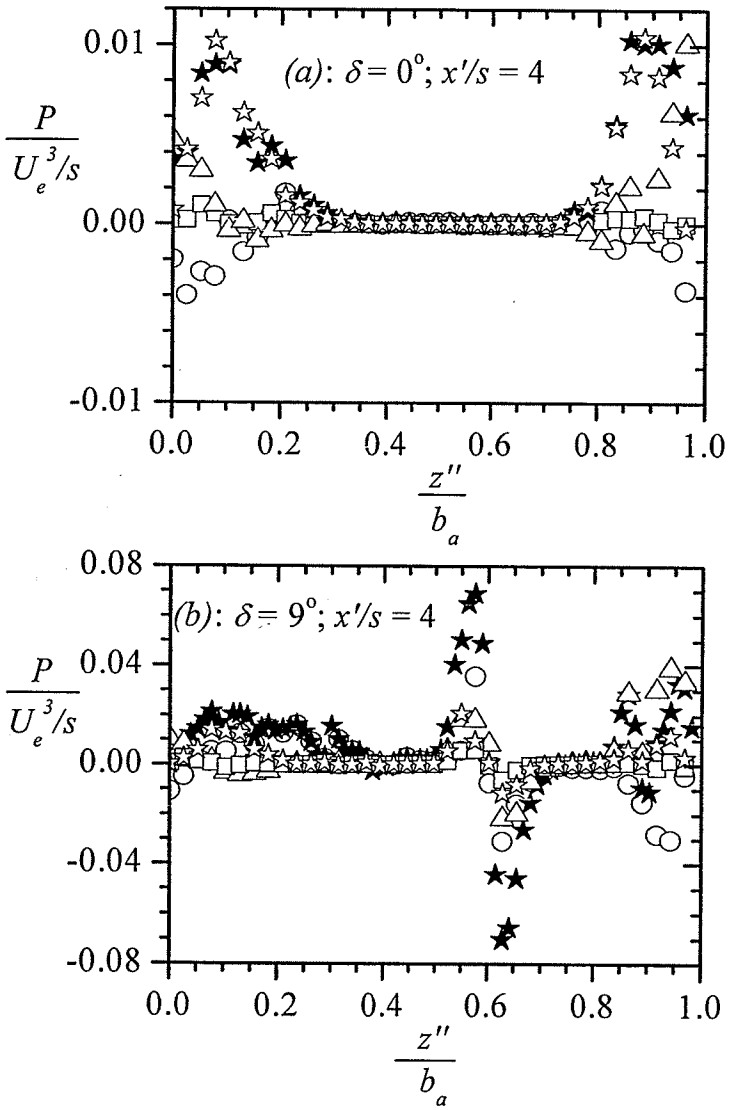

Figure 5.32: Production term in the transport equation for turbulent kinetic energy: $-u^2(\partial U/\partial x)$: ○; $-uw(\partial W/\partial x)$: □; $-uw(\partial U/\partial z)$: ☆; $-w^2(\partial W/\partial z)$: △; P_T:★.

evaluated at $x'/s = 4$ for tests $\delta_o U_{0.52}$ and $\delta_9 U_{0.52}$ are shown in Figures 5.32a and 5.32b, respectively. For each test, the contribution from $-uw\partial W/\partial x$ is small compared with the other components. Even though the two normal stress components ($u^2\partial U/\partial x$ and $w^2\partial W/\partial z$) are individually non-zero, their net contribution is nearly zero. The reason is that the magnitudes of the Reynolds normal stresses (u^2 and w^2) are similar while $\partial U/\partial x \approx -\partial W/\partial z$ from continuity requirement. Therefore, $u^2\partial U/\partial x$ and $w^2\partial W/\partial z$ are of opposite sign but their magnitudes are nearly the same. As a result, nearly all the contribution to the total production term in the TKE comes from $uw\partial U/\partial z$. Figure 5.32 shows that the level of turbulence production is substantially higher for the inclined bar than for the aligned bar. This observation may explain the substantially higher levels of turbulence intensities and Reynolds shear stress observed between and downstream of the inclined bars compared with measured values for the aligned bars.

5.3. Head Loss

5.3.1. Small-Scale

This section reports head losses estimated from the various correlations proposed for quantifying head loss produced by trashrack. Tables 5.1, 5.2 and 5.3 show head loss coefficients (Δh^*), respectively, for *Series I*, *Series II* and *Series III*. In Tables 5.1, 5.2 and 5.3, the head loss coefficients were obtained using the expression, head loss coefficient, $\Delta h^* = \Delta h/(U_1^2/2g)$. In general Table 5.1 shows that the head loss coefficients increase with Reynolds number and bar inclination to approach flow. The unexpected high value of Δh^* for $\theta_0 U_{0.26}$ obtained from the energy Eq. (2.1), may be due to

Table 5.1: Summary of head loss coefficients (Δh^*) for *Series I.*

Test	U_1 (m/s)	Δh^*					
		Eq. (2.1)	Eq. (2.2)	Eq. (2.3)	Eq. (2.4)	Eq. (2.5)	Eq. (2.12)
$\theta_0 U_{0.26}$	0.25	0.93	0.39	0.30	0.29	0.31	0.27
$\theta_0 U_{0.52}$	0.50	0.33	0.51	0.30	0.29	0.31	0.27
$\theta_0 U_{0.76}$	0.73	0.74	0.49	0.30	0.29	0.31	0.27
$\theta_6 U_{0.52}$	0.50	0.33					
$\theta_9 U_{0.52}$	0.50	0.40					
$\theta_{12} U_{0.52}$	0.50	0.76					

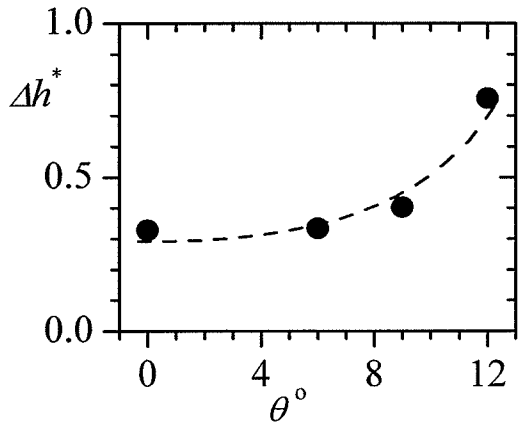

Figure 5.33: Variation of head loss coefficient with bar inclination for Eq. (2.1).

Note: The dash line is used to help visualize the trend of head loss coefficient.

measurement error. This is because (h_1-h_2) is only 3 mm, a value that is not very different from the measurement uncertainty of ± 1 mm in measuring h_1 and h_2. The values of Δh^* from the Eq. (2.1) for $\theta_6 U_{0.52}$ and $\theta_9 U_{0.52}$ are 1.5% and 22.7%, respectively, higher than that for $\theta_0 U_{0.52}$, whereas $\theta_{12} U_{0.52}$ produced head loss coefficient that is more than twice the value for $\theta_0 U_{0.52}$. These data are graphically shown in Figure 5.33, and it can be seen that the head loss coefficient varied non-linearly with bar inclination. The results imply that small values of bar inclination could be used to produce effective blockage that may prevent some fish from being entrained into turbine without increasing head losses

substantially. The data reported by Spangler [6] also reported increased head loss for inclined trashracks. Table 5.2 shows that the values of Δh^* increases with bar depth

Table 5.2: Summary of head loss coefficients (Δh^*) for *Series II*

Test	U_1 (m/s)	Δh^*					
		Eq. (2.1)	Eq. (2.2)	Eq. (2.3)	Eq. (2.4)	Eq. (2.5)	Eq. (2.12)
SQ-L_{50}-$p_{0.20}$	0.487	0.31	0.53	0.30	0.29	0.26	0.27
SQ-L_{76}-$p_{0.20}$	0.500	0.33	0.51	0.30	0.29	0.31	0.27
SQ-L_{110}-$p_{0.20}$	0.547	0.51	0.58	0.30	0.29	0.36	0.27
SQ-L_{110}-$p_{0.26}$	0.519	0.62	0.81	0.50	0.49	0.63	0.44
SQ-L_{110}-$p_{0.33}$	0.504	1.19	1.13	0.78	0.76	0.98	0.69

and blockage ratio. For example, Eq. (2.1) predicts a 39% decrease in Δh^* as the bar depth decreased from 110 mm (SQ-L_{110}-$p_{0.20}$) to 50 mm (SQ-L_{50}-$p_{0.20}$). Also, as the blockage ratio increases from p = 0.20 to 0.26, Eq. (2.1) yielded a 22% increase in Δh^*. A further increase in p to 0.33 increased Δh^* by 134%. In Table 5.3, the values of Δh^* decrease with decreasing bar thickness, bar depth and for streamlined bar shape. For example, Eq. (2.1) yielded a 50% decrease in Δh^* as the bar thickness decreased from 12 mm (SQ-s_{12}-L_{50}) to 6 mm (SQ-s_6-L_{50}). It should be noted that as the bar thickness decreases, the blockage ratio also decreases, thereby increasing the net flow area through the trashracks. Hence, less flow resistance is posed to trashrack comprised of lesser bar thicknesses, for a given centre-to-centre spacing. As a result, the head loss coefficients observed for bars with thicknesses other than 12 mm are smaller. Similarly, the values of

Table 5.3: Summary of head loss coefficients (Δh^*) for *Series III*

Test	U_1 (m/s)	Δh^*					
		Eq. (2.1)	Eq. (2.2)	Eq. (2.3)	Eq. (2.4)	Eq. (2.5)	Eq. (2.12)
SQ-s_6-L_{50}	0.487	0.22	0.24	0.12	0.12	0.10	0.12
SQ-s_9-L_{50}	0.487	0.34	0.38	0.22	0.21	0.18	0.20
SQ-s_{12}-L_{50}	0.487	0.43	0.48	0.35	0.34	0.27	0.31
SQ-$s_{12}L_{76}$	0.483	0.45	0.49	0.35	0.34	0.33	0.31
SQ-s_{12}-L_{100}	0.493	0.46	0.54	0.35	0.34	0.37	0.31
ST-s_{12}-L_{100}	0.471	0.21	0.44	0.11	0.10		

Δh^* obtained from Eq. (2.1) decreases by 53% as the bar shape was changed from rectangular (SQ-s_{12}-L_{100}) to streamlined (ST-s_{12}-L_{100}) section.

5.3.2. Large-Scale

Tables 5.4 and 5.5 present a summary of the head loss coefficients, Δh^* for the various large-scale trashrack models. The values of Δh^* from Eq. (2.1) are subsequently plotted in Figure 5.34. In general, the tables and the figures demonstrated that Δh^* increases with blockage ratio and bar inclination to approach flow, irrespective of the shape of the bars. Figure 5.34a shows that Δh^* increased linearly with blockage ratio, irrespective of bar thickness, bar depth and shape of the bar leading edge. It should be noted that the sectional blockage produced by the bars depends on the bar thickness, centre-to-centre spacing and number of bars. Therefore, blockage ratio would increase with increased bar thickness (for a given centre-to-centre spacing), number of bars and reduced bar centre-to-centre spacing. In Table 5.4, the values of Δh^* for aligned square leading edge bars having L = 100 mm and s = 12 mm (SQ-s_{12}-L_{100}), for example, shows that the values of Δh^* obtained from Eq. (2.1) decreased by 38% when the blockage ratio, p was decreased from 0.24 to 0.16 and by 71% and 92%, respectively, when p was further decreased to 0.12 and 0.08. The results for the round leading edge trashrack bars (RD-s_{12}-L_{100}) also show similar reduction in head loss coefficient when the blockage ratio is decreased. However, the values of Δh^* for RD-s_{12}-L_{100} are substantially lower than the corresponding values obtained for SQ-s_{12}-L_{100}. The percentage reduction in the values of Δh^* when round leading edge bars (RD-s_{12}-L_{100}) are used instead of square leading edge bars (SQ-s_{12}-L_{100}) was calculated by comparing the head loss coefficient for a given

blockage ratio, p but different leading edge as follows: $(\Delta h^*_{p,\ RD} - \Delta h^*_{p,\ SQ})/(\Delta h^*_{p,\ SQ})$, expressed as a percentage. With the exception of blockage ratio of p = 0.08, the percentage reduction varies from 33% to 50%. These results have important implications

Table 5.4: Summary of head loss coefficients, Δh^* for various test conditions.

Bar Type	p	U_1 (m/s)	Δh^*					
			Eq. (2.1)	Eq. (2.2)	Eq. (2.3)	Eq. (2.4)	Eq. (2.5)	Eq. (2.12)
Square leading edge (SQ) SQ-s_{12}-L_{100} (*Series 1*)	0.24	0.543	0.53	1.05	0.52	0.50	0.54	0.46
	0.18	0.555	0.48	0.72	0.35	0.34	0.34	0.31
	0.16	0.547	0.33	0.58	0.27	0.26	0.25	0.24
	0.12	0.546	0.15	0.39	0.17	0.16	0.15	0.16
	0.09	0.557	0.10	0.29	0.12	0.12	0.10	0.12
	0.08	0.557	0.05	0.24	0.09	0.09	0.07	0.10
Round leading edge (RD) RD-s_{12}-L_{100} (*Series 2*)	0.24	0.560	0.35	1.05	0.39	0.38		
	0.18	0.558	0.24	0.71	0.27	0.26		
	0.16	0.560	0.21	0.58	0.20	0.19		
	0.12	0.557	0.09	0.38	0.13	0.12		
	0.09	0.563	0.06	0.28	0.09	0.09		
	0.08	0.565	0.05	0.23	0.07	0.07		
Square leading edge (SQ) SQ-s_{12}-L_{50} (*Series 3*)	0.24	0.545	0.50	1.00	0.52	0.50	0.40	0.46
	0.18	0.548	0.43	0.68	0.35	0.34	0.25	0.31
	0.16	0.553	0.31	0.55	0.27	0.26	0.19	0.24
	0.12	0.551	0.19	0.38	0.17	0.16	0.11	0.16
	0.09	0.561	0.10	0.28	0.12	0.12	0.07	0.12
	0.08	0.561	0.08	0.23	0.09	0.09	0.05	0.10
Square leading edge (SQ) SQ-s_9-L_{50} (*Series 4*)	0.18	0.548	0.34	0.65	0.32	0.31	0.27	0.29
	0.14	0.558	0.27	0.46	0.22	0.21	0.17	0.20
	0.12	0.558	0.22	0.38	0.17	0.16	0.13	0.16
	0.09	0.563	0.12	0.27	0.11	0.11	0.07	0.11
	0.07	0.567	0.01	0.20	0.08	0.08	0.05	0.08
	0.06	0.567	0.02	0.17	0.06	0.06	0.04	0.07

for fish protection and generation cost. For example, compared with bars with square leading edge, round leading edge bars with tighter spacing could be used to prevent fish from being entrained into turbines without increasing head loss substantially. When the bar depth of the square leading edge bar was changed from L = 100 mm to L = 50 mm,

the variation in the values of Δh^* was very small. For example, for p = 0.24, Eq. (2.1) predicts 5% drop in Δh^* when the bar depth was reduced from L = 100 mm to L = 50 mm. This observation is consistent with the notion that, for L/s > 3, the separated shear layer and head losses should not vary significantly with L/s (Orsbon [10]). A significant reduction in Δh^* is observed by reducing the bar thickness. For example, when the bar depth was maintained at L = 50 mm, and the bar thickness was reduced from

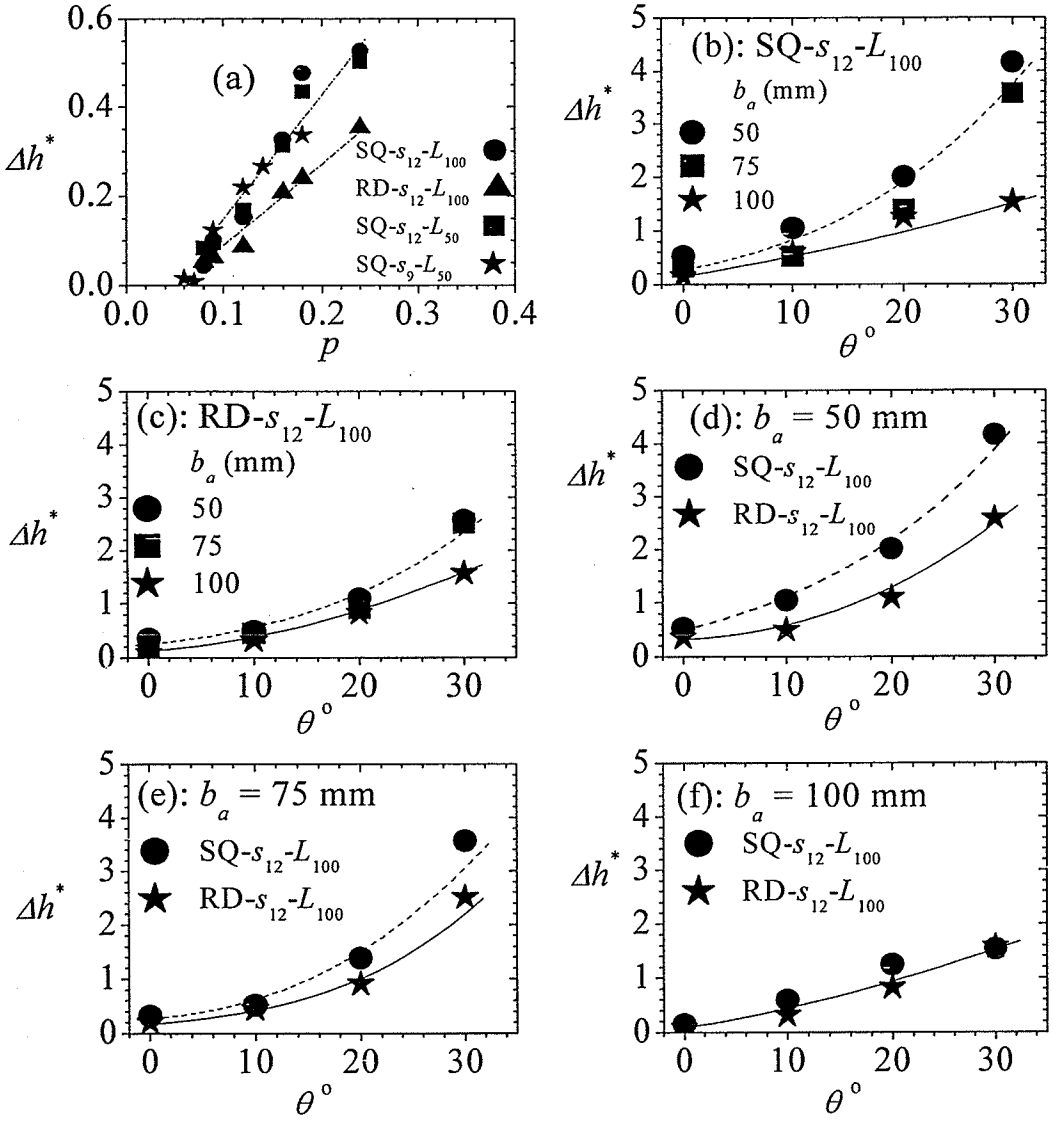

Figure 5.34: Variation of head loss coefficient with blockage ratio and bar inclination.

Note: The dash and solid lines are used to help visualize the trend of head loss coefficient.

s = 12 mm (SQ-s_{12}-L_{50}) to s = 9 mm (SQ-s_9-L_{50}), and for b_a = 50 mm, 63 mm and 75 mm, the percentage reduction in Δh^* are, respectively, 33, 39 and 30 for Eq. (2.1). This is because Δh^* also depends on physical thickness of the bar for a given centre-to-centre spacing. As shown in Figure 5.34a, the plots for SQ-s_{12}-L_{100}, SQ-s_{12}-L_{50} and SQ-s_9-L_{50} nearly collapse on each other. Further, Figure 5.34a shows that the differences in Δh^* for SQ-s_{12}-L_{100} and RD-s_{12}-L_{100} increase as the blockage ratio increases. In fact, Figure 5.34a, indicates that the slope (or rate of increase of Δh^* with p) is steeper for the square-edged bars (SQ-) than for the round leading edge bars (RD-). It is important to note that, by increasing the blockage ratio, the flow area within the bars reduces and the velocity between the bars increases. The increased blockage ratio and higher velocity within the bars contribute immensely to a drop in water level within and downstream of the models, thus increasing the head loss.

It is also apparent from Table 5.5 that bar inclination increases the values of Δh^*. Figures 5.34b and 5.34c show variation of Δh^* with θ for various bar spacing/blockage but similar leading edges while Figure 5.34d to 5.34f compare Δh^* at equal blockage ratio for SQ-s_{12}-L_{100} and RD-s_{12}-L_{100} models at various θ. Irrespective of blockage ratio, the head loss coefficient increased substantially as the bar inclination was increased. Unlike the linear variation of Δh^* with blockage ratio (Figure 5.34a), there is generally a non- linear relationship between Δh^* and bar inclination. For a particular bar shape (square or round leading edge), the increase in Δh^* with θ is more dramatic for a tighter bar spacing, i.e., larger blockage ratio. At the largest bar spacing (b_a = 100 mm), Δh^* increased almost linearly with θ (Figure 5.34f) but the increase is exponential for a tighter bar spacing (b_a

= 50 mm and 75 mm, Figures 5.34d and 5.34e). Furthermore, for a given blockage ratio, inclined bars with square leading edges produced significantly higher head loss than the corresponding bars with a round leading edge, but as the bar spacing increases, the differences between Δh^* values for the rounded and square-edged bars diminishes. In fact, there is no significant difference between Δh^* values for rounded and square edged bars if the bar spacing is increased to b_a = 100 mm (Figure 5.34f). It is important to note from Figure 5.34d that the Δh^* value for SQ-s_{12}-L_{100} at $\theta = 10^o$ is similar to Δh^* value for RD-s_{12}-L_{100} at $\theta = 20^o$.

Table 5.5: Summary of head loss coefficients, Δh^* for various test conditions.

Bar type	L (mm)	s (mm)	b_a (mm)	θ^o	n	p	U_1 (m/s)	Δh^* Eq. (2.1)
Square leading edge (SQ) SQ-s_{12}-L_{100} (*Series 5*)	100	12	50	0	18	0.24	0.543	0.53
	100	12	50	10	18	0.24	0.495	1.05
	100	12	50	20	18	0.24	0.491	2.01
	100	12	50	30	18	0.24	0.477	4.16
	100	12	75	0	12	0.16	0.547	0.33
	100	12	75	10	12	0.16	0.499	0.52
	100	12	75	20	12	0.16	0.501	1.38
	100	12	75	30	12	0.16	0.488	3.57
	100	12	100	0	9	0.12	0.546	0.15
	100	12	100	10	9	0.12	0.501	0.6
	100	12	100	20	9	0.12	0.500	1.25
	100	12	100	30	9	0.12	0.495	1.54
Round leading edge (RD) RD-s_{12}-L_{100} (*Series 6*)	100	12	50	0	18	0.24	0.560	0.35
	100	12	50	10	18	0.24	0.493	0.49
	100	12	50	20	18	0.24	0.488	1.10
	100	12	50	30	18	0.24	0.485	2.57
	100	12	75	0	12	0.16	0.560	0.21
	100	12	75	10	12	0.16	0.502	0.44
	100	12	75	20	12	0.16	0.499	0.91
	100	12	75	30	12	0.16	0.491	2.51
	100	12	100	0	9	0.12	0.557	0.09
	100	12	100	10	9	0.12	0.501	0.31
	100	12	100	20	9	0.12	0.498	0.83
	100	12	100	30	9	0.12	0.496	1.57

5.3.3. Comparison between Small-Scale and Large-Scale Models: As noted earlier, only 3 to 5 bars were employed in the small-scale models while 6 to 18 bars (depending on the bar thickness and blockage ratio) were used for the large scale models. Moreover, the Reynolds number ($Re_s = U_e s/\nu$) at typical Manitoba Hydro generation stations is much higher than those studied in the present study and the Froude numbers at the generation station are also much lower than those tested. Therefore, the small-scale and large-scale experiments are compared in Figure 5.35 to examine if there are any significant scaling effects. It should be noted that the Reynolds numbers, $Re_s = U_e s/\nu$, in the small-scale experiments are in the range $3000 \leq Re_s \leq 9060$ while those for the large-scale models are $5000 \leq Re_s \leq 6800$. Similarly, the Froude number based on the upstream

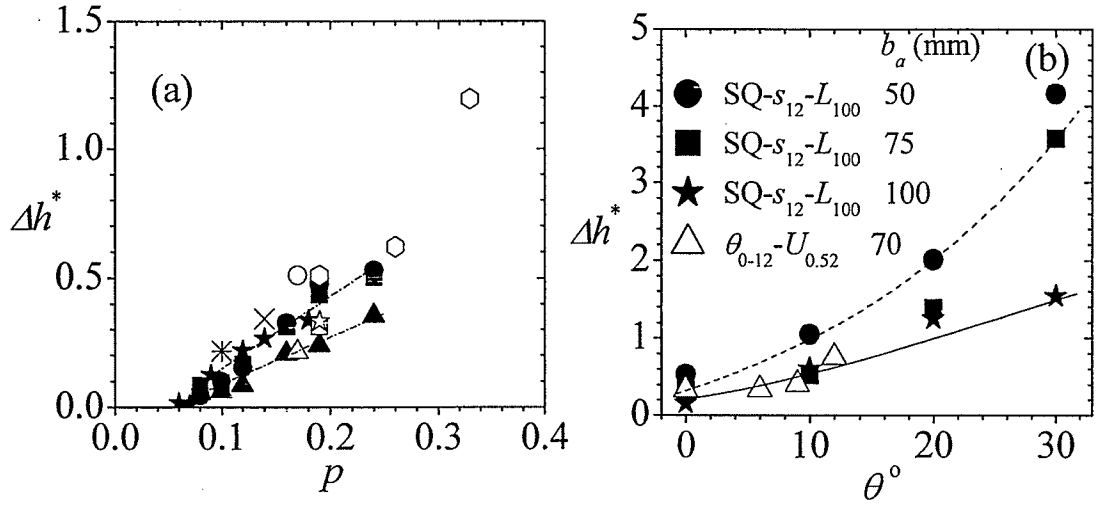

Figure 5.35: Variation of head loss coefficient with blockage ratio and bar inclination: (a): Large-scale (●: SQ-s_{12}-L_{100}, ▲: RD-s_{12}-L_{100}, ■: SQ-s_{12}-L_{50}, ★: SQ-s_9-L_{50}); Small-scale (⬡: SQ-s_{12}-L_{110}, ○: SQ-s_{12}-L_{100}, △: ST-s_{12}-L_{100}, ☆: $\theta_0 U_{0.52}$, □: SQ-s_{12}-L_{50}, +: SQ-s_{12}-L_{50}, ×: SQ-$s_9 L_{50}$, ✳: SQ-s_6-L_{50},); (b) Large-scale (SQ-s_{12}-L_{100}) and Small-scale ($\theta_{0\text{-}12}U_{0.52}$)

water depth and approach velocity for the small-scale and large-scale models are, respectively, $0.19 \leq F \leq 0.57$ and $0.22 \leq F \leq 0.26$. No systematic scaling effects are found for the aligned bars plotted in Figure 5.35a. It should be noted, however, that the scatter among Δh^* values for the small-scale models is larger than those in the large-scale model. As mentioned earlier, the measurement uncertainty in Δh^* values is larger for the small-scale models. As observed earlier, the streamlined bars and round leading edge bars produced lower head losses than the square edged bars. The differences between the round leading edge/streamlined bars and the square bars increase with increasing blockage ratio. The good agreement between Δh^* values for the streamlined bars and the round leading edge bars would imply that head losses produced by trashracks are more dependent on the specific geometry of the leading edge than the shape of the bar section. Figure 5.35b compares the values of Δh^* for SQ-s_{12}-L_{76} at b_a = 70 mm (small-scale) with the results obtained for SQ-s_{12}-L_{100} at b_a = 75 mm (large scale) in the flume. These plots also demonstrate that there are no substantial scaling effects in these experiments.

5.3.4. Comparison between Energy Equation and Empirical Correlations

In this section, the head loss coefficients obtained from Eq. (2.1) are compared with values obtained from selected empirical correlations. It should be noted that the test conditions for which Eq. (2.2), Eq. (2.3), Eq. (2.5) and Eq. (2.12) were reported in the literature did not include bars inclined at angles to the approach flow. Consequently, no value of Δh^* is reported in the present study for Eq. (2.2), Eq. (2.3), Eq. (2.5) and Eq. (2.12) for bars inclined to the approach flow. The test conditions for which Eq. (2.5) and Eq. (2.12) were reported did not consider streamlined and round leading edge bars, as a

result no value of Δh^* is reported for Eq. (2.5) and Eq. (2.12) were for these bar geometries (Table 5.3 and Table 5.4) in the present study. In general, Tables 5.1, 5.2, 5.3 and 5.4 shows that the values of Δh^* obtained from Eq. (2.1) are somewhat higher than the values calculated from Eqs. (2.3), (2.4), (2.5) and (2.12) but lower than the values obtained from Eq. (2.2). Wahl [3] reported that Eq. (2.2) tends to overestimate head losses by as much as 55%. The average percentage difference between values from Eq. (2.1) and Eq. (2.2) for the aligned bars is 53 for the small-scale experiments. Specifically, for $\theta_0 U_{0.52}$ (small-scale) the values of Δh^* from Eq. (2.3) and Eq. (2.5) are respectively, 11% and 6% lower than that obtained from Eq. (2.1), whereas the value from Eq. (2.2) is 18% higher.

For the large-scale experiments, Δh^* from Eq. (2.2) are 50% to well over 100% larger than those obtained from Eq. (2.1). These differences are much higher than suggested by Wahl [3]. For the tightest bar spacing, the Δh^* values from both Eq. (2.1) and Eq. (2.3) are in very good agreement. This is true for bars with round or square leading edge. In general, Eq. (2.3) and Eq. (2.5) tend to predict higher Δh^* values than Eq. (2.1) for relatively higher blockage ratio ($p \geq 0.16$ for s = 12 mm bars, and $p \geq 0.09$ for s = 9 mm bars). The corresponding head losses (Δh) in millimeters (mm) are presented in Tables A-1, A-2, A-3, A-4 and A-5 in the Appendix.

5.4. Ecological and Hydraulics Implications

The flow patterns shown in Figures 5.3 to 5.12 may have important implications for head losses and fish protection, including fish responses near the bars. The larger dead-water

zones with relatively calm flow on the leeward side of the inclined bars and flow acceleration and turbulence just upstream of the bars are key to fish responses to either avoid the trashrack or to be swept through the bars and reach the turbines. Once fish end-up near the turbines they are subject to mortality or injury from direct contact, sudden pressure changes or elevated levels of shear and turbulence.

The more asymmetric nature of the flow pattern and recirculation bubbles around the inclined bars will modify the pressure recovery. In effect, inclined bars would produce asymmetric hydrodynamic loads that may lead to more severe vibration problems in comparison to aligned bars. Knisely [12] examined flow past single rectangular bar at incidence and found that Strouhal number, which determines vortex shedding frequency for which vibration failures occur, increases with angle of incidence. From their DNS results, Herman *et al.* [13] suggested that vortices generated by individual bars gave rise to pressure fluctuations which in turn produced hydrodynamic forces on the bars.

Although, reduced bar spacing provides a greater protection for fish entrainment, it produces higher sectional blockage. This increased section blockage increases flow acceleration and may render fish of smaller sizes which swim near this region highly susceptible to entrainment by the flow through the trashrack and into the turbine and draft tube, where they are vulnerable. Nevertheless, reduced spacing increases head losses due to trashracks. It is very important to note that since trashrack comprising of streamlined bars or round leading edge bars produce low head losses, their spacing can be made tighter to diminish potential for fish entrainment into turbine. Similarly, bars with

rounded leading edges could be inclined at moderate angles to prevent fish from entering the turbines without a significant increase in head loss.

Chapter 6: CONCLUSION AND RECOMMENDATIONS

6.1. Conclusions

6.1.1 Mean Velocity and Turbulent Statistics

This study investigates the effects of approach velocity, bar inclination to approach flow, bar spacing and bar geometry on the mean velocities, turbulent statistics and head loss through trashrack models. The velocity measurements were made using PIV (for small-scale) and ADV (for large-scale). The present study demonstrates that the mean velocities and turbulent quantities normalized by the approach velocity are nearly independent of Reynolds number but tend to increase with increasing bar inclination and blockage ratio. Inclined bars also produced asymmetric flow patterns that may result in potential asymmetric hydrodynamic loads on the bars and vibration problems. While there is no clear dependence of the mean velocities and turbulent quantities on bar depth, the magnitude of the mean velocities and turbulent quantities decreased for trashrack models comprised of reduced bar thickness and streamlined bars.

6.1.2 Head Losses

With regards to trashrack head losses obtained for the various test conditions, the following conclusions are summarized:

1. The results demonstrate that as the approach velocity increased so did the head loss across the trashrack models.
2. The head loss coefficient increases linearly with increasing blockage ratio. For a given centre-to-centre spacing, the head loss also decreases with decreasing bar thickness.

3. The head loss increased non-linearly with bar inclination to approach flow. Moderate bar inclinations may offer a compromise between providing better conditions for fish without significantly increasing head losses and hydroelectricity generation costs.
4. Reduced head loss coefficients were observed for streamlined and round leading edge bars, suggesting that their spacing can be made much tighter to reduce fish entrainment into turbines.
5. It was observed that because the existing correlations proposed to calculate head losses were developed under different test conditions, the head loss coefficients predicted by those correlations were not in good agreement with the measured values.

6.2. Recommendations for Future Studies

The following recommendations are suggested for further studies based on the present experimental study of turbulent open channel flow near trashrack models.

- ✓ Trashracks use supporting beams which produce additional head losses. Tests with trashracks that consist of both horizontal and vertical beams would be useful to quantify the total head loss produced by trashracks.
- ✓ Trashracks with inclined bars are to produce louver effects thereby preventing certain species of fish from being entrained into turbine. Because of the asymmetric nature of flow associated with inclined bars, it is argued to be susceptible to more severe hydrodynamic load imbalance. The vibration characteristics of inclined bars should be thoroughly assessed so that for the

purpose of fish protection, moderate bar inclination can be employed to provide louver effects for fish without significantly increasing head loss.

- ✓ Streamlined bars are useful in mitigating head losses produced by trashracks. They are however not used for trashrack construction because of its susceptibility to vibration and difficulty in cleaning with cleaning machine. There is the need to study the vibrational characteristics of trashrack consisting of streamlined bars.

REFERENCES

[1] McPhail, G., 2006, Wuskwatim Shaped Bar Trashrack Design, Project No. 02-003-01.27, Manitoba Hydro, Winnipeg, Manitoba.

[2] Lemon, D. D., Topman, D. R., Bouhadji, L., Lampa, J. Understanding causes for systematic error in ASFM measurements of turbine discharge

[3] Wahl, T. L. 1992, Trash Control Structures and Equipment: A Literature Review and Survey of Bureau of Reclamation Experience. U.S. Bureau of Reclamation, Denver office, Colorado, Report No. R-92-05: 1-35

[4] Mosonyi, E., 1963, Water Power Development, vol. 1

[5] Escande, L., C.r. Acad. Sci., Paris 218, 179, 1944.

[6] Spangler, J. Investigation of the Loss through Trash Racks Inclined Obliquely to the Stream Flow, Hydraulic Practice, pp. 461-470.

[7] Mueusburger, H., Volkart, P. and Minor, H.-E., 2001, A New Improved Formula for Calculating Trashrack Losses. http://www.iahr.org/e-library/beijing_proceedings/Theme_D/A%20new%20IMPROVED%20FORMULA.html

[8] Kirschmer, O. 1926. Untersuchungen uber den Gefällverlust an Rechen, *Mitt. Hydr. Inst., Munich*, Ed. D Thoma, No. 1, p. 21

[9] Fellenius, W., and Lindquist, E. G. W., 1929, Experiments on the Head Loss Caused by Protecting Racks at Water-Power Plants, Hydraulic Practice, pp. 533-538.

[10]. Osborn, J. F., 1968, Rectangular-Bar Trashrack and Baffle Headlosses, Journal of Power Division, vol. 94, No. PO2, pp. 111-123

[11] Doland, J. J., 1954, Hydro Power Engineering

[12] Knisely, C. W., 1990, Strouhal numbers of rectangular cylinders at incidence: A review and new data. Journal of Fluids and Structures, 4 pp. 371-393

[13] Hermann, F. Billeter, P. and Hollenstein, R., 1998, Investigations on the flow through a trashrack under different inflow conditions, Hydroinformatics '98, Balkema, Rotterdam, pp. 121-128.

[14] Mueusburger, H., Herman, F., Hollenstein, R., Comparison of Numerical and Experimental Investigstions of Trashrack Losses, Laboratory of Hydraulics, Hydrology and Glaciology (VAW), ETH Zurich

[15] Yeh, H. H. and Shrestha, M., 1988, Free-surface flow through screen, Journal of Hydraulic Engineering, vol.115, No. 10, pp. 1371-1385

[16] Raffel, M., Willert, C., Kompehenhans, J. 1998, Particle Image Velocimetry, A Practical Guide, New York, Springer, 1998

[17] Westerweel, J., Draad, A. A., Th. Van der Hoeven, J. G., and Oord van, J., 1996, "Measurement of Fully Developed Turbulent Pipe Flow with Digital Particle Image Velocimetry," Exp. Fluids, **20**, pp. 165 – 177.

[18] Mei, R., Adrian, R. J. Hanratty, T. J., 1991, Particle Dispersion in Isotropic Turbulence under Stokes Drag and Basset Force with Gravitational Settling, J. Fluid Mech., **225**, pp. 481 – 495.

[19] Willert, C. E., and Gharib, M., 1991, Digital Particle Image Velocimetry, Experiments in Fluids, vol. 10, pp. 181-193

[20] Kean, R. D. and Adrain, R. J., 1990, Optimization of Particle Image Velocimetry, Part1: Doubled pulsed system, Measurement Science Tecknology, vol. 1, pp. 1202-1215

[21] Katopodis, C. (2005). Developing a toolkit for fish passage, ecological flow management and fish habitat works. IAHR J. *Hydraulic Research*, 43(5), 451-467.

[22] Hinze, J. O., (1959). *Turbulence*, McGraw-Hill, New York.

APPENDIX

Table A-1: Summary of head loss (Δh) for *Series I*

Test	θ	U_1 (m/s)	Δh (mm)					
			Eq. (2.1)	Eq. (2.2)	Eq. (2.3)	Eq. (2.4)	Eq. (2.5)	Eq. (2.12)
$\theta_0 U_{0.26}$	0°	0.25	2.95	1.25	0.94	0.91	0.99	0.85
$\theta_0 U_{0.52}$	0°	0.50	4.18	6.51	3.77	3.65	3.96	3.39
$\theta_0 U_{0.76}$	0°	0.73	20.21	13.43	8.04	7.78	8.43	7.22
$\theta_6 U_{0.52}$	6°	0.50	4.24					
$\theta_9 U_{0.52}$	9°	0.50	5.13					
$\theta_{12} U_{0.52}$	12°	0.50	9.63					

Table A-2: Summary of head loss (Δh) for *Series II*

Test	L (mm)	U_1 (m/s)	Δh (mm)					
			Eq. (2.1)	Eq. (2.2)	Eq. (2.3)	Eq. (2.4)	Eq. (2.5)	Eq. (2.12)
SQ-L_{50}-$p_{0.20}$	50	0.487	3.78	6.46	3.58	3.46	3.13	3.21
SQ-L_{76}-$p_{0.20}$	76	0.500	4.18	6.51	3.77	3.65	3.96	3.39
SQ-L_{110}-$p_{0.20}$	110	0.547	7.78	8.89	4.52	4.37	5.55	4.05
SQ-L_{110}-$p_{0.26}$	110	0.519	8.53	11.12	6.90	6.67	8.69	6.04
SQ-L_{110}-$p_{0.33}$	110	0.504	15.47	14.60	10.12	9.79	12.71	8.93

Table A-3: Summary of head loss (Δh) for *Series III*

Test	L (mm)	U_1 (m/s)	Δh (mm)					
			Eq. (2.1)	Eq. (2.2)	Eq. (2.3)	Eq. (2.4)	Eq. (2.5)	Eq. (2.12)
SQ-s_6-L_{50}	50	0.487	2.62	2.94	1.45	1.41	1.26	1.45
SQ-s_9-L_{50}	50	0.487	4.15	4.60	2.68	2.59	2.20	2.47
SQ-s_{12}-L_{50}	50	0.487	5.20	5.85	4.25	4.11	3.31	3.77
SQ-$s_{12}L_{76}$	76	0.483	5.30	5.78	4.18	4.04	3.90	3.71
SQ-s_{12}-L_{100}	100	0.493	5.69	6.65	4.36	4.21	4.57	3.86
ST-s_{12}-L_{100}	100	0.471	2.42	5.03	1.25	1.17		

Table A-4: Summary of head losses, Δh for various test conditions.

Bar Type	p	U_1 (m/s)	Δh (mm)					
			Eq. (2.1)	Eq. (2.2)	Eq. (2.3)	Eq. (2.4)	Eq. (2.5)	Eq. (2.12)
Square leading edge (SQ)	0.24	0.543	7.93	15.84	7.82	7.56	8.14	6.84
	0.18	0.555	7.49	11.33	5.52	5.34	5.37	4.90
	0.16	0.547	4.98	8.85	4.05	3.91	3.88	3.67
SQ-s_{12}-L_{100}	0.12	0.546	2.33	5.96	2.58	2.50	2.28	2.46
	0.09	0.557	1.59	4.58	1.90	1.84	1.52	1.90
(*Series 1*)	0.08	0.557	0.72	3.73	1.47	1.43	1.14	1.54
Round leading edge (RD)	0.24	0.560	5.67	16.70	6.29	6.08		
	0.18	0.558	3.81	11.22	4.22	4.08		
	0.16	0.560	3.31	9.19	3.21	3.10		
RD-s_{12}-L_{100}	0.12	0.557	1.38	6.05	2.03	1.96		
	0.09	0.563	1.00	4.56	1.47	1.42		
(*Series 2*)	0.08	0.565	0.86	3.81	1.15	1.11		
Square leading edge (SQ)	0.24	0.545	7.61	15.11	7.88	7.62	6.09	6.89
	0.18	0.548	6.66	10.39	5.38	5.20	3.88	4.77
SQ-s_{12}-L_{50}	0.16	0.553	4.87	8.50	4.13	4.00	2.94	3.75
	0.12	0.551	2.60	5.92	2.63	2.54	1.73	2.50
(*Series 3*)	0.09	0.561	1.53	4.48	1.93	1.87	1.15	1.93
	0.08	0.561	1.34	3.74	1.50	1.45	0.86	1.56
Square leading edge (SQ)	0.18	0.548	5.15	10.01	4.91	4.74	4.06	4.38
	0.14	0.558	4.21	7.32	3.52	3.41	2.68	3.25
	0.12	0.558	3.48	6.00	2.70	2.61	2.00	2.57
SQ-s_9-L_{50}	0.09	0.563	2.00	4.33	1.79	1.73	1.21	1.81
	0.07	0.567	0.15	3.28	1.30	1.25	0.79	1.39
(*Series 4*)	0.06	0.567	0.27	2.77	1.01	0.98	0.59	1.14

Table A-5: Summary of head losses, Δh for various test conditions.

Bar type	L (mm)	s (mm)	b_a (mm)	$\theta°$	n	p	U_l (m/s)	Δh (mm) Eq. (2.1)
Square leading edge (SQ)	100	12	50	0	18	0.24	0.543	7.93
	100	12	50	10	18	0.24	0.495	13.08
	100	12	50	20	18	0.24	0.491	24.73
	100	12	50	30	18	0.24	0.477	48.23
SQ-s_{12}-L_{100}	100	12	75	0	12	0.16	0.547	4.98
	100	12	75	10	12	0.16	0.499	6.64
(*Series 5*)	100	12	75	20	12	0.16	0.501	17.71
	100	12	75	30	12	0.16	0.488	43.37
	100	12	100	0	9	0.12	0.546	2.33
	100	12	100	10	9	0.12	0.501	7.64
	100	12	100	20	9	0.12	0.500	15.93
	100	12	100	30	9	0.12	0.495	19.21
Round leading edge (RD)	100	12	50	0	18	0.24	0.560	5.67
	100	12	50	10	18	0.24	0.493	6.12
	100	12	50	20	18	0.24	0.488	13.32
	100	12	50	30	18	0.24	0.485	30.82
RD-s_{12}-L_{100}	100	12	75	0	12	0.16	0.560	3.31
	100	12	75	10	12	0.16	0.502	5.67
(*Series 6*)	100	12	75	20	12	0.16	0.499	11.52
	100	12	75	30	12	0.16	0.491	30.79
	100	12	100	0	9	0.12	0.557	1.38
	100	12	100	10	9	0.12	0.501	4.01
	100	12	100	20	9	0.12	0.498	10.48
	100	12	100	30	9	0.12	0.496	19.67